DISSERTATION

MODELING LOCAL PATTERN FORMATION ON MEMBRANE SURFACES USING NONLOCAL INTERACTIONS

Submitted by

Melissa Adkins

Department of Mathematics

In partial fulfillment of the requirements

For the Degree of Doctor of Philosophy

Colorado State University

Fort Collins, Colorado

Spring 2015

Doctoral Committee:

Advisor: Yongcheng Zhou

Diego Krapf
James Liu
Jennifer Mueller

ABSTRACT

MODELING LOCAL PATTERN FORMATION ON MEMBRANE SURFACES USING NONLOCAL INTERACTIONS

The cell membrane is of utmost importance in the transportation of nutrients and signals to the cell which are needed for survival. The magnitude of this is the inspiration for our study of the lipid bilayer which forms the cell membrane. It has been recently accepted that the lipid bilayer consists of lipid microdomains (lipid rafts), as opposed to freely moving lipids. We present two lipid raft models using the Ginzburg-Landau energy with addition of the electrostatic energy and the geodesic curvature energy to describe the local pattern formation of these lipid rafts. The development and implementation of a C^0 interior penalty surface finite element method along with an implicit time iteration scheme will also be discussed as the optimal solution technique.

TABLE OF CONTENTS

LIST OF FIGURES

CHAPTER 1

Introduction

Cancer, Cardiac health disease, Alzheimer's, Parkinson's, HIV, and Immune Disorders are some of the most recognized and deadly diseases in the world today. Shockingly, all of these diseases are in some way linked to abnormalties in lipid rafts [53, 25, 26, 16, 46, 9]. Lipid rafts have become intensely studied for the roles they play in cell signaling and their link to these diseases. Lipid rafts are highly dynamic cholesterol-enriched microdomains of the cell membrane. As we dive deeper into the study of lipid rafts we first need to start with fundamental knowledge of the cell membrane.

Bilayer membranes are selectively permeable which allows them to regulate what enters and exits the cell. Along with many other functions such as cellular signaling processes and signal transduction make the cell membrane essential for the survival of the cell. Although cell membranes have been studied since 1855, introduced by C. Naegeli and C. Cramer, the present membrane model is still being developed. The first fluid mosaic model shown in Figure 1.1 of a biological membrane was developed by Singer and Nicolson [15]. More specific mosaic models can be established by considering different lipid types or lipid to protein ratios.

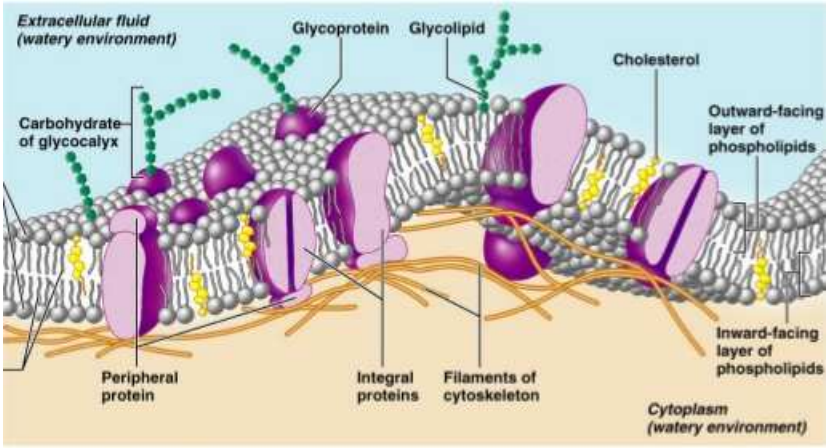

Figure 1.1: Fluid Mosaic Model [15].

Since 1972 there have been some changes to the fluid mosaic model, such as the memebrane having a patchwork mesh such that inside the patches lipid movement occurs, instead of lipids moving freely across the entire cell surface [48]. We call these patches "Lipid Rafts" a name coined by Simons and Ikonen at the 2006 Keystone Symposium of Lipid Rafts and Cell Function. Specifically they defined lipid rafts as small (10-200nm), heterogeneous, highly dynamic, sterol- and sphingolipid-enriched domains that compartmentalize cellular processes [52]. Figure 1.2 is the most recent membrane model including lipid rafts. Some experimental images of lipid rafts are shown in Figure 1.3.

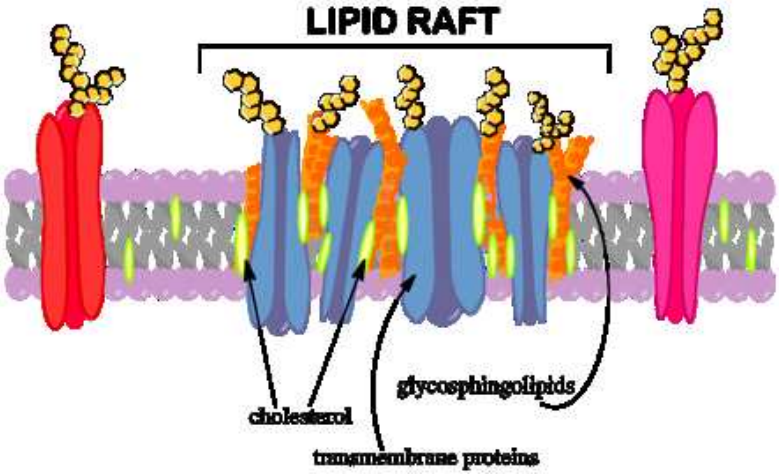

Figure 1.2: Illustration of a lipid raft model

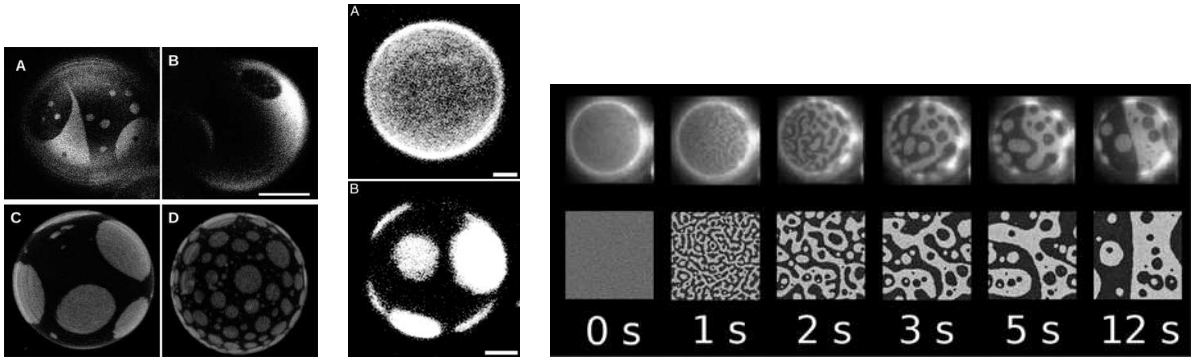

(a) (b) (c)

Figure 1.3: (a) These fluorescent images are representative of images of ordered and disordered phase coexistence in giant unilamellar vesicles and correspond to different lipid species and ratios [5]. (b) Phase separation shown experimentally using giant unilamellar vesicles [33]. (c) Comparison of experimental (top) and 2D simulated (bottom) phase separation kinetics [10].

To understand the form and stability of a cell membrane the knowledge of lipid behavior is essential, since the cell membrane is made of a lipid bilayer with embedded proteins and cholesterol. The lipid bilayer is formed by the spontaneous self arrangement of phosopholipids, such that their tails are isolated from the surrounding aqueous solution. This arrangement leaves their heads free to associate with other surfaces. In aqueous solutions lipids are able to laterally exchange locations with their neighbors c.f. Figure 1.4. This movement happens often, in fact millions of times a second [13]. Another type of movement, that happens much more slowly and not as often, is a lipid flip-flop c.f. Figure 1.4. This occurs when a lipid crosses the hydrophobic membrane core. This rare event has many degrees of freedom and multiple time scales which make it very difficult to understand and model. Despite being the least understood dynamical process in the membrane, there are currently some simple models using transition path sampling (TPS) of this biological phenomena [42].

Many models have been developed to model the lateral movement of lipid diffusion in membranes [58]. However, there are significantly fewer models developed to include lipid rafts. This may not be surprising as lipid rafts are a fairly new development in biological science. In fact there are many unanswered questions including [2, 39, 47, 1]:

(1) How do rafts organize themselves?

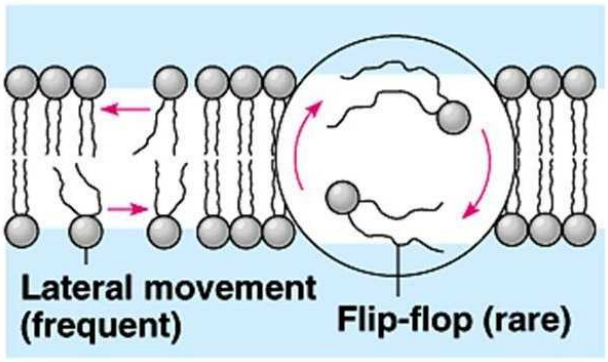

Figure 1.4: Lateral lipid movement (left) and flip-flop lipid movement (right) [41].

(2) How are the lipids attracted to the raft?

(3) How does the raft move?

(4) What is the size and lifetime of a lipid raft?

(5) How are the two monolayers of a bilayer coupled to form a trans-membrane raft?

(6) What do detergent extraction and insolubility tell us about the state of cell membranes?

(7) How directed are the effects of cholesterol depletion on cell function?

(8) What is the physiological function of lipid rafts?

(9) What effect do diet and drugs have on lipid rafts?

By answering these questions we are able to understand the applications of lipid rafts better. Applications include drug development, biosensors, solar energy transduction, fabrication of synthetic giant vesicles, and formation of virus envelopes [2, 47].There are so many unanswered quesions because of the lack of direct visualization of lipid rafts. Despite this lack we do have great knowledge about lipid rafts, for example the membrane has two different states, one being a fluid-like state. This occurs when lipids are moving freely around the membrane. The other being a gel-like state. This might be a state when lipids are clustered together to form a lipid raft. One could start with modeling these different states, particularly the phase transitions and the surface patterns made during these transitions as seen in Figure 1.3.

In this paper we will focus on answering Questions 1 and 4 from above by modeling the local pattern formations of lipid rafts. Chapter 2 and 3 will give background information about lipid rafts and the mathematics used to model them. These two chapters will provide helpful material, derivations, and explanations to better understand the models presented. Chapter 4 will discuss current models found in the literature. Chapter 5 will introduce our lipid raft model with electrostatics. In Chapter 6 we will propose a model for lipid rafts including line tension and geodesic curvature. Chapters 7 and 8 will present the numerical technique needed for the computational simulations of lipid rafts using the models we developed. In Chapter 9 we will discuss our numerical results and in Chapter 10 we will draw conclusions and discuss future works.

CHAPTER 2

Biology Modeling Background

Although lipid rafts are not completely understood at present there is growing knowledge on this topic. We will review some helpful information about modeling lipid rafts in this section. Membranes are formed by lipids, cholesterol, and proteins. It is known that the membrane undergoes a structural phase transition that changes the orientation of these membrane components. The changes are specifically reflected in the order of the lipid hydrocarbon chains [40]. The "ordered" phase, often denoted L_o, finds the lipid hydrocarbon chains to be ordered c.f Figure 2.1 (a). This ordering is largely caused by a high concentration of cholesterol imbedded in the membrane. This phase is what models the lipid raft. The "disorded" phase, often denoted L_d, is the state when lipid hydrocarbon chains are disordered c.f Figure 2.1 (b). In this phase the lipids diffuse freely over the membrane. The atoms in this phase are not as tightly packed as in L_o which makes it possible for molecules to pass through the membrane. As the lipid chains become less ordered the thickness of the bilayer

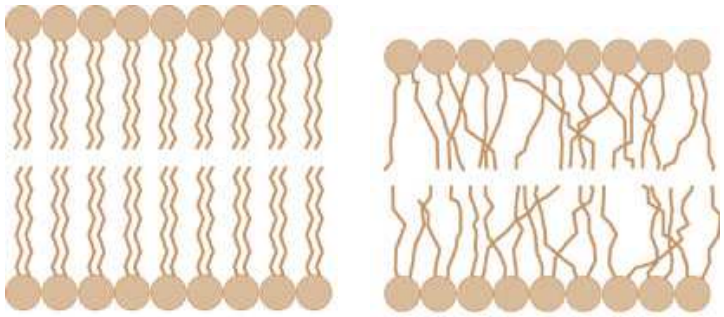

(a) (b)

Figure 2.1: Ordered (a) and Disordered (b) domains [43]

is decreased as shown in Figure 2.2 [43]. This height mismatch produces a "step-like" gap as seen in Figure 2.2 (a). There exist lipids with one full saturated hydrocarbon chain and one partially unsaturated chain, often referred to as "hybrid lipids" which fill in this gap as seen in Figure 2.2 (b). It has been suggested that "hybrid-lipids" are line active at the interface

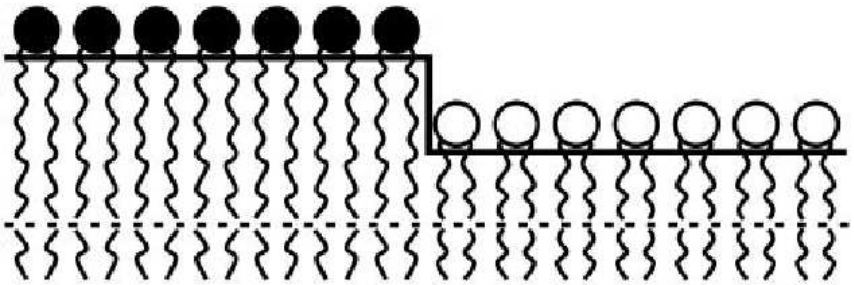

(a)

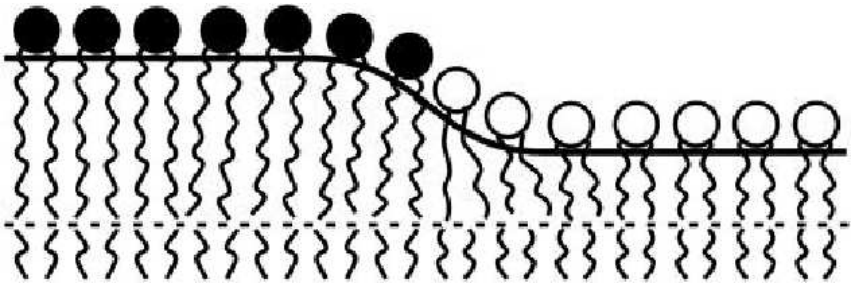

(b)

Figure 2.2: Showing the thickness mismatch [7]

of ordered and disordered lipid phases [7]. This may lead to line tension reduction for strong interaction strengths [8]. This height mismatch produces a free energy between ordered and disordered lipid phases. This height mismatch is associated with the hybrid lipids packing at the interface and is also associated with the specific curvature of the interface.

Along the interface between the L_o and L_d phases a line tension arises, and it has been suggested that the phase separation minimizes the total line tension [55]. This means the line tension favors having the L_o and L_d domains form two large domains instead of several microdomains, much like the domains produced by the Cahn-Hilliard equations in Figure 2.3. A competing interaction with the line tension is the electrostatic interactions of the membrane components. Since lipids, proteins, and ions all carry a charge the lipid blayer will have a net charge as well. For highly charged lipids or proteins the electrostatic interaction could be a competing interaction with line tension causing microdomain (or lipid raft) formation. To model these behaviors we consider the free energy of a physical system given

by

$$F = E - TS \ ,$$

where E is the energy of the system, T is the absolute temperature, S is the entropy. By minimizing the free energy we maximize the entropy of the system. This leads to maximizing disorder, at the same time each particle tries to minimize its energy of interaction with its neighbor, creating a type of organization. This results in a competition between the entropy of mixing and the desire to have particular neighbors. It has become very popular to model this behavior using phase field models [10, 40, 11, 51].

2.1. Derivation of the Cahn-Hilliard Equation

The Cahn-Hilliard equation has been used for many years to describe the process of phase separation of two species of particles spontaneously separating to form domains containing only an individual species of particles. This process is illustrated in Figure 2.3. We can

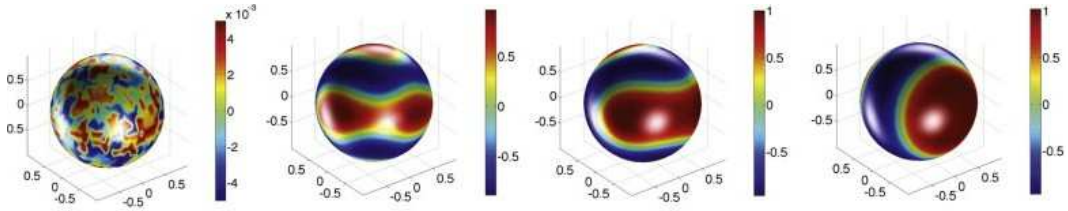

Figure 2.3: A computational simulation of phase separation is shown [20].

describe the phase separation by defining two components A and B with concentrations and making the following assumptions:

(1) Domain is filled with binary fluid: A and B particles with concentrations m_1 and m_2 respectively.

(2) Diffusion is the only form of transportation

(3) AA and BB interactions are favorable

(4) AB and BA interactions are unfavorable.

(5) The phase function can be defined in either of two ways

$$\phi = \frac{m_1 - m_2}{m_1 + m_2} , \qquad c = \frac{m_1}{m_1 + m_2} .$$

It follows that $-1 \leq \phi \leq 1$ and $0 \leq c \leq 1$.

In this study we will define the phase function as ϕ above. With these assumptions we further define the Ginzburg Landau free energy functional:

(1) $$F(\phi) \colon = \int_\Omega \left(f(\phi) + \frac{1}{2}|\nabla \phi|^2 \right) dx ,$$

where each term is defined as the following.

(1) $f(\phi)$ is a double well potential. An example of this would be to let $f(\phi)=\frac{\phi^4}{4} - \frac{\phi^2}{2}$ pictured below.

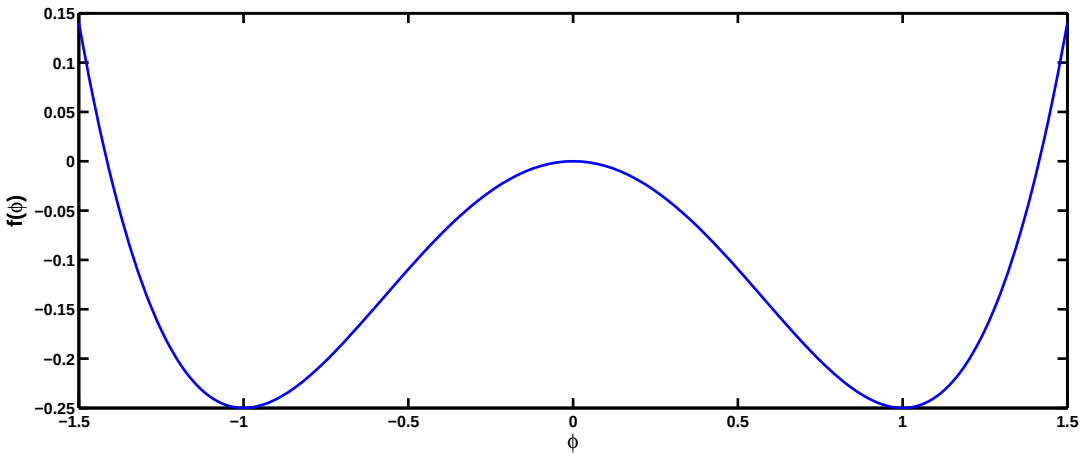

If we minimize $f(\phi)$ this term will draw the two particle species apart.

(2) $\int_\Omega \frac{1}{2}|\nabla \phi|^2$ represents the energy cost associated with local variations in ϕ, specifically those associated with domain walls. When these variations are small the gradient squared term is the lowest order approximation to the energy cost of creating the wall [51].

(3) The first variation, $\frac{\delta F(\phi)}{\delta \phi}$, would quantify how the energy changes when particle concentrations change. This variation is called the chemical potential of the system

$$\frac{\delta F(\phi)}{\delta \phi} = f'(\phi) - \Delta\phi = \mu \ . \tag{2}$$

The time dependent problem

$$\frac{\partial \phi}{\partial t} = -f'(\phi) + \Delta\phi \ , \tag{3}$$

is known as the Allen-Cahn equation. We use Fick's Law,

$$J = -M(\phi)\nabla\mu \ ,$$

to define the particle flux, J, where $M(\phi)$ is the phase field mobility. We have a mass conservation constraint so there is no creation or destruction of particles. We have the following time-dependent equation.

$$\frac{\partial \phi}{\partial t} + \nabla \cdot J = 0$$

$$\frac{\partial \phi}{\partial t} = \nabla \cdot (M(\phi)\nabla\mu)$$

Then the Cahn-Hilliard Equation in an open domain, $\Omega \in \mathbb{R}^n$, for $n = 2, 3$ is as follows:

$$\frac{\partial \phi}{\partial t} = \nabla \cdot (M(\phi)\nabla(f'(\phi) - \epsilon^2\Delta\phi)) \ \ in \ \ \Omega$$

$$\nabla\phi \cdot n = 0 \ \ on \ \ \partial\Omega$$

$$(M(\phi)\nabla\mu) \cdot n = 0 \ \ on \ \ \partial\Omega \ ,$$

where n is the outward normal to the domain. These equations will serve as a starting base for modeling lipid rafts.

2.2. Electrostatic Energy

Electrostatics has been proven to help stabilize biomolecular conformations [49], making it very useful to include electrostatic interactions in biomolecular models. These interactions

can exist over a long distance since they decay slowly at low ion concentrations. The electrostatic potential can be discribed by Gauss's Law c.f Theorem 2.2.1 from which we can derive Poisson's equation seen in Equation (4).

THEOREM 2.2.1. *[*Gauss's Law*] [49] If the volume within an arbitrary closed mathematical surface holds a net charge Q, then the electrical flux Φ_E through the surface is given by*

$$\Phi_E = \frac{Q}{\epsilon_0} ,$$

ehere ϵ_0 is an electric constant.

Φ_E may also be expressed as a surface integral as folows

$$\Phi_E = \int_S E \cdot dA ,$$

where E is the electric field and dA represents an element of area.

Alternatively, this law may be written in a differential form as

$$\nabla \cdot E = \frac{\rho}{\epsilon_0} ,$$

where ρ is the total electric charge density.

Using Gauss's Law the Poisson Equation can be derived.

$$\nabla^2 \psi = -\frac{\rho}{\epsilon_0} \tag{4}$$

This equation gives the electric potential, ψ, in terms of electric charge density ρ. We will incorporate the electrostatic interactions into the model we develop in Chapter 5.

2.3. Bending Energy

Another interaction we will model is the competition between the phase separation and the curvature energy. Some recent studies suggest that one can use the preferred interface

curvature for specific lipid compositions to determine the microdomain sizes [7]. The bending of a bilayer membrane modeled as a surface, S, also known as the Willmore Energy, has been introduced as

$$F = \int_S \left[\kappa_H \left(H - C_0\right)^2 + \kappa_K K\right] \, dA \ ,$$

where H is the mean curvature and K is the Gauss curvature of the domain. κ_H and κ_K are the mean bending rigidity and the Gauss bending rigidity respectively and C_0 is the spontaneous curvature. By the Gauss-Bonnet theorem the total Gauss curvature of the domain is a constant and can be computed using the Euler characteristics of the domain. This term is topologically invariant, so we may simplify the bending energy by just considering the mean curvature

$$F = \int_S \left[\kappa_H \left(H - C_0\right)^2\right] \, dA$$

In this study the phase separation occurs on a given surface, so the phase interface is a 3-D curve. The curvature of a curve, α, on a surface, S, is given by

$$\kappa = \alpha''(t) \cdot n(t) + \alpha''(t) \cdot (n(t) \times \alpha'(t)) = \alpha''(t) \cdot (n(t) + (n(t) \times \alpha'(t)))$$

Where $\alpha''(t) = \kappa_n N(t)$, $N(t) = \frac{T'}{|T|}$ is the principal normal vector, and T is the unit tangent vector to α. This is called the geodesic curvature. These types of curves can be seen in Figure 2.4.

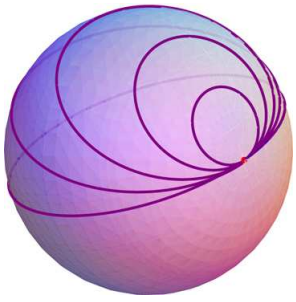

Figure 2.4: Curves of constant geodesic curvature

REMARK 2.3.1. It's important to note that the geodesic curvature of the great circle (the curve running along the sphere equator) is zero. This can be seen by considering the projection of the great circle onto the the plane tangent to the curve. This projection is essentially a straight line with zero curvature. The domain interfaces produced by the Cahn-Hilliard equation are great circles where the system has a minimum curvature.

We can write this geodesic curvature, κ, in terms of the phase field function, ϕ, defined in Equation (1) as

$$\kappa = \nabla_s \cdot n = \nabla_s \cdot \left(\frac{\nabla_s \phi}{|\nabla_s \phi|} \right) \ .$$

This will be an essential measurement when comparing the curvature of the mircodomains found numerically to the curvature of lipid rafts found experimentally. We develop a model including this interaction in Chapter 6.

CHAPTER 3

Background Mathematics

We will be modeling lipid rafts on surfaces, so it is important to note the difference between surface differential operators and domain differential operators. In this chapter we will introduce surface differentia operators and present some helpful theorems for surface calculations.

3.1. Surface Operators

Let S be a compact two dimensional, C^2-hypersurface imbedded in $\mathbb{R}^3$. If we are able to extend the surface S then let d be some oriented distance function defined on some open set $U \subseteq \mathbb{R}^3$, then S may be written as

$$S = \{x \in U | d(x) = 0\} \ , \tag{5}$$

where $\nabla d \neq 0$ and $\partial S = \emptyset$ [22]. Then the tangential gradient, ∇_s, on S can be written as

$$\nabla_s u = \nabla u - (\nabla u \cdot \vec{n})\vec{n} \tag{6}$$

for $u \in C^1(S)$, where ∇ is the three-dimensional gradient and $\vec{n}$ is the normal vector on S. For smooth S we can assume that there is a strip

$$U = \{x \in \mathbb{R}^3 | \, dist(x, S) < \delta\}$$

about S where

$$x = a(x) + d(x)\vec{n} \tag{7}$$

is unique for $a(x) \in S$ and $|d(x)| = dist(x, S)$ [22]. This suggests that we can uniquely extend a function u defined on S to U by

$$\hat{u}(x) = u(x - d(x)\vec{n}) \ , \ x \in U \tag{8}$$

If we are unable to extend the surface, S to U then let $c(t)$ be a curve defined on the same Riemannian manifold as that defined by S. Then $c(t) = S(u(t), v(t))$ where $u(t), v(t)$ are tangent vectors to the surface S then by taking the derivative of $c(t)$ we obtain

$$c'(t) = \frac{\partial S}{\partial u}\frac{du}{dt} + \frac{\partial S}{\partial v}\frac{dv}{dt} \ . \tag{9}$$

If $s(t)$ represents the arc length of the curve then

$$s(t) = \int_a^b |c'(t)| \, dt \ , \tag{10}$$

and

$$\frac{ds}{dt} = |c'(t)| \ . \tag{11}$$

This means

$$\begin{aligned}
\left(\frac{ds}{dt}\right)^2 &= |c'(t)|^2 \\
&= \left(\frac{\partial S}{\partial u}\frac{du}{dt} + \frac{\partial S}{\partial v}\frac{dv}{dt}\right)^2 \\
&= \left(\frac{\partial S}{\partial u}\frac{du}{dt}\right)^2 + 2\left(\frac{\partial S}{\partial u}\frac{du}{dt} \cdot \frac{\partial S}{\partial v}\frac{dv}{dt}\right) + \left(\frac{\partial S}{\partial v}\frac{dv}{dt}\right)^2 \ .
\end{aligned}$$

If we let

$$g_{1,1} = \left(\frac{\partial S}{\partial u}\right)^2 ,$$
$$g_{2,2} = \left(\frac{\partial S}{\partial v}\right)^2 ,$$
$$g_{1,2} = \left(\frac{\partial S}{\partial u} \cdot \frac{\partial S}{\partial v}\right) ,$$
$$g_{2,1} = \left(\frac{\partial S}{\partial v} \cdot \frac{\partial S}{\partial u}\right) .$$

Then the metric tensor g is given by

$$g = \begin{bmatrix} g_{1,1} & g_{1,2} \\ g_{2,1} & g_{2,2} \end{bmatrix} . \tag{12}$$

Note that this matrix is symmetric, since $g_{2,1} = g_{1,2}$. With this we can compute g for any parameterized surface [58]. Then we have the following alternative definitions of the surface gradient and surface divergence.

$$\nabla_s u = \frac{1}{\sqrt{g}} \frac{\partial}{\partial x^i} u^i \sqrt{g}$$
$$\Delta_s u = \nabla_s \cdot \nabla_s u = \frac{1}{\sqrt{|g|}} \frac{\partial}{\partial x^i} (\sqrt{|g|} g^{ij} u) .$$

3.2. Surface Theorems

Theorem 3.2.1 (*Divergence Theorem*). *[54] Let $M \subset \mathbb{R}^3$ be a compact three-dimensional manifold-with-boundary, ∂M, and $\vec{n}$ the unit outward normal on ∂M. Let F be a differentiable vector field on M. Then,*

$$\int_M \nabla \cdot F dV = \int_{\partial M} F \cdot \vec{n} \, dA$$

THEOREM 3.2.2 (*Integration By Parts*). *Let $M \subset \mathbb{R}^3$ be a compact three-dimensional manifold-with-boundary and $\vec{n}$ the unit outward normal on ∂M. If u and v are two continuosly differentiable functions on the closure of M, then*

$$\int_M \nabla_s uv \; dV = \int_{\partial M} uv \, \vec{n} \; dA - \int_M u \nabla_s v dV$$

where $\vec{n}$ is the outward unit surface normal to ∂M

3.3. Helpful Derivations

A few minor but helpful derivations are presented here for the convenience of the reader.

$$\begin{aligned} \Delta\phi^2 &= \frac{\partial^2(\phi^2)}{\partial x^2} + \frac{\partial^2(\phi^2)}{\partial y^2} + \frac{\partial^2(\phi^2)}{\partial z^2} \\ &= \frac{\partial}{\partial x}(2\phi\phi_x) + \frac{\partial}{\partial y}(2\phi\phi_y) + \frac{\partial}{\partial z}(2\phi\phi_z) \\ &= 2\phi_x\phi_x + 2\phi\phi_{xx} + 2\phi_y\phi_y + 2\phi\phi_{yy} + 2\phi_z\phi_z + 2\phi\phi_{zz} \\ &= 2|\nabla\phi|^2 + 2\phi\Delta\phi \end{aligned} \tag{13}$$

$$\begin{aligned} \Delta\phi^3 &= \frac{\partial^2(\phi^3)}{\partial x^2} + \frac{\partial^2(\phi^3)}{\partial y^2} + \frac{\partial^2(\phi^3)}{\partial z^2} \\ &= \frac{\partial}{\partial x}\left(3\phi^2\phi_x\right) + \frac{\partial}{\partial y}\left(3\phi^2\phi_y\right) + \frac{\partial}{\partial z}\left(3\phi^2\phi_z\right) \\ &= 6\phi\phi_x\phi_x + 3\phi^2\phi_{xx} + 6\phi\phi_y\phi_y + 3\phi^2\phi_{yy} + 6\phi\phi_z\phi_z + 3\phi^2\phi_{zz} \\ &= 6\phi|\nabla\phi|^2 + 3\phi^2\Delta\phi \end{aligned} \tag{14}$$

CHAPTER 4

Current Models of Lipid Raft

4.1. Electrostatics

In addition to evidences that lipid rafts might be formed by electrostatic interactions, [39], there is research suggesting other significant interactions such as thermal fluctuations, long-range repulsive interactions, and dipole interactions may also play a significant role in driving the formation of lipid rafts [10, 40, 11, 51]. Throughout this section we will review a model of each type.

4.1.1. Thermal Fluctuations. It is known that thermal fluctuations play a role in coarsening of binary fluids by driving coalescence [10]. This is also observed in phase separation in lipid membranes. This is considered in the model presented by Brown et al.[10]. They treat the membrane as a flat 2-D plane and follow the Ginzburg Landau free energy model presented in Chapter 2. They arrive at an overdamped model

$$\frac{\partial\phi(x,t)}{\partial t} + v\cdot\nabla\phi(x,t) = M\nabla^2\frac{\delta F}{\delta\phi(x,t)} + \theta(x,t)\ ,$$
$$v_i(x,t) = \int d^2x' T^m_{ij}(x-x')\left[\frac{\delta F}{\delta\phi}\nabla'_j\phi(x',t) + \zeta_j(x',t)\right]\ ,$$

where ϕ is the phase field function and F is the Ginzburg Landau free energy introduced in Equation (1). T^m_{ij} is the Green's function for in-plane velocity field, $\theta(x,t)$ and $\zeta_j(x',t)$ are Gaussian white random forces. Simplifying further we have

$$\partial_t\phi(r,t) = M\nabla^2\mu + \theta(r,t) - v\cdot\nabla\phi(r,t)\ ,$$
$$v_i(r,t) = \int d^2r' T^m_{ij}(r-r')\times\left[\mu\nabla'_j\phi(r',t) + \zeta_j(r',t)\right]\ ,$$

where μ is the chemical potential defined as in (3). Details of the numerical scheme can be found in [10]. It is easily seen that this model has a convection/advection term which is an advantageous feature. The results of including thermal fluctuations are reported in Figure 4.1. They conclude thermal fluctuations speed up the coarsening process and that the path taken to coarsening may be different. It is noted that ϕ is not at equillibrium in Figure 4.1. The authors also make some very enlightening conclusions reguarding scaling laws. However,

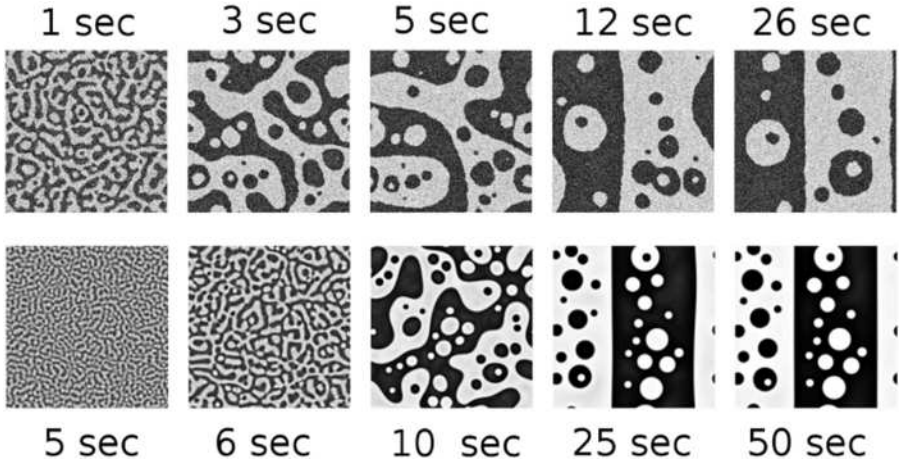

Figure 4.1: Both top and bottom images are snapshots of the coarsening process over time. The system size is 30μm x 30μm. The top image includes thermal effects and the bottom image does not include thermal effects [10]

in this model the membrane is treated as a flat geometry which may not be favorable as the membrane is a surface with curvature and this curvature has been shown to effect phase separation [3]. One could also ask since ϕ is not at equillibrium, how long do these patterns exist? Do the patterns stay around long enough for the biological processes to take place on lipid rafts? I am interested in the equillibrium state of this model and the results that are produced.

4.1.2. Long-Range Repulsive Interactions. C.B. Muratov develops a system with short-range attractive interactions and long-range repulsive Coulomb interactions [11]. This model is formed from the Ginzburg-Landau free energy model presented in Chapter 2. We take the domain to be a 2-D flat infinite domain and we have the following general mean-field

free energy functional

$$F = \int d^d x \left(f(\phi) + \frac{1}{2}|\nabla\phi|^2 + \frac{\alpha}{2} \int d^d x' g[\phi(x)] G(x - x') g[\phi(x')] \right) , \tag{15}$$

where $G(x - x')$ is a positive-definite kernel for long range interactions, $\alpha > 0$ is a coupling constant, $g(\phi)$ is a monotonic function that is equal to zero at some $\phi = \bar{\phi}$, and d is the dimension of space. Using singular pertubation, Fourier analysis, and linearization he is able to make estimates of the location of domain walls, characteristic sizes of domains, and develop some scaling laws. He uses a simple gradient descent method to study and analyze the homogenous system. Simulations of this model are presented in Figure 4.2. He notes that

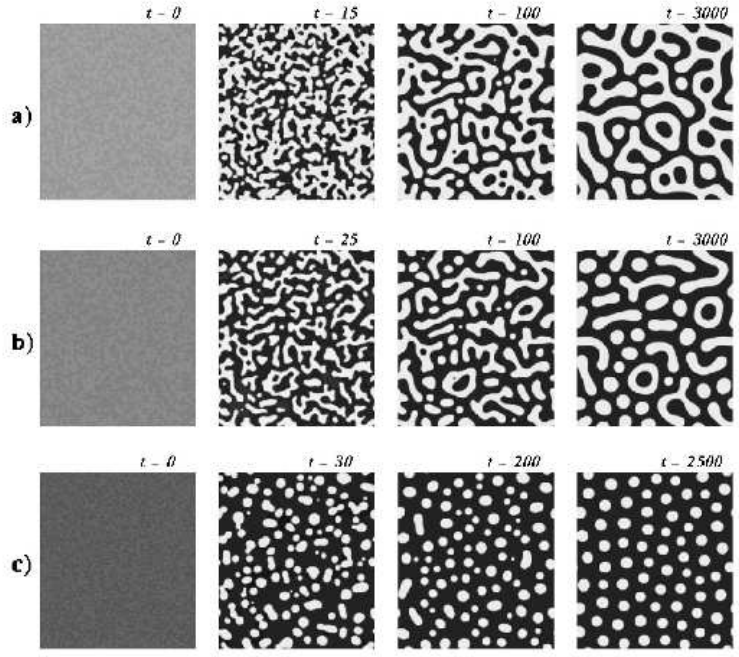

Figure 4.2: Coarsening of the domain pattern with (a) $\bar{\phi} = 0$, (b) $\bar{\phi} = -0.2$, (c) $\bar{\phi} = -0.5$. The system is size 400 x 460

the system and the resultant patterns are extremely sensitive to the intial conditions. This results in a large number of metastable patterns which locally minimize the energy along with the equillibrium patterns. They emphasize that the stability analysis really addresses the metastability of the resultant patterns. Again, in this model the membrane is treated as

a flat plane which may not be favorable as the membrane is a surface with curvature and this curvature can effect phase separation [3]. Also, the membrane is a finite charged domain, and much of the analysis is done on a neutrally charged infinite domain which may not be an accurate model. The gradient flow for F in Equation (15) is a nonconserved system thus cannot be applied to the modeling of lipid rafts. However, this model serves as a good building block to develop better physical models.

4.1.3. Dipole-Dipole Interactions. Michael Seul and David Andelman developed one of the earliest models of domain patterns and phase separation [51]. They consider phase separation caused by competing interactions, especially the repulsive dipole-dipole electrostatic interactions. The model is expressed as a Ginzburg Landau energy functional as presented in Chapter 2 on a 2-D domain.

$$F_\phi = \int d^d x \left(f(\phi) + \frac{1}{2}|\nabla \phi|^2 \right) \ .$$

They also note that in the minimization of the energy functional, the second term can be expressed in terms of the line tension, γ, and domain wall length, l, i.e.

$$F_\phi = \int d^d x(\phi) + \gamma l \ .$$

If two species carry dipole moments and all the molecular dipoles point along the direction normal to the plane they interact pairwise by a repulsive electrostatic interaction. Setting μ equal to one dipole moment and setting the other equal to zero this interaction may be modeled in the continuum limit by

$$\begin{aligned} F_d = &- \frac{\mu^2}{2} \int \int d^2x d^2x' \phi(x) g(x, x') \phi(x) \\ &- \frac{\mu^2}{2} \int d^2 q \phi_{-q} G(q) \phi_q \end{aligned}$$

Where μ is the dipole moment, q is a finite wave number, $G(q)$ and ϕ_q are the Fourier transforms of $g(|r - r'|)$ and $\phi(r)$ respectively, and $g(|r - r'|) = |x - x'|^{-3}$ expresses the

long-range nature of the dipole-dipole interactions. Combining the two terms we have the complete free energy

$$F = F_\phi + F_d$$

Once more, the domain is represented as a flat 2-D plane, which is not a physical feature of membranes. However, this model does serve as a good base for modeling membranes and the ideas are used in many of the current models.

4.2. Curvature

There has been indications that the free energy associated with the curvature of domain patterns competes with the line tension of the domain to produce multiple lipid domains. Recently, a few lipid raft models have considered the interaction between the line tension and the curvaure of the lipid domains [4, 8, 7, 31, 32, 3]. This interaction is discussed in detail in Chapter 2, but we will summarize a few models found in the literature here.

4.2.1. Lattice Model. We have chosen to summarize the model given in [7, 8]. This model is a spontaneous curvature model that uses packing arguments to predict the size of a lipid raft that is stabilized by a line of hybrid lipids saturating the interface as seen in Figure (4.3). The hybrid lipids must minimize the energy associated with the chain length mismatch while conserving their molecular volumes. The portion of the total free energy that dictates the response of the interface to bending is the mismatch free energy. This free energy is due to the volume constraints of the hybrid lipid and is given by

$$g = \left(\frac{V_s}{a w_s\ (1 - 1/2\, w_s\, H)} - L_S\right)^2 + \left(\frac{V_u}{a w_u\ (1 + 1/2\, w_u\, H)} - L_u\right)^2 + \left(-\frac{V_s}{a w_s\ (1 - 1/2\, w_s\, H)} + \frac{V_u}{a w_u\ (1 + 1/2\, w_u\, H)}\right)^2 \tag{16}$$

Where L_s and L_u is the length of the saturated chain of the hybrid lipid and the unsaturated chain of the hybrid chain respectively. H is the curvature, V_s and V_u are the volumes

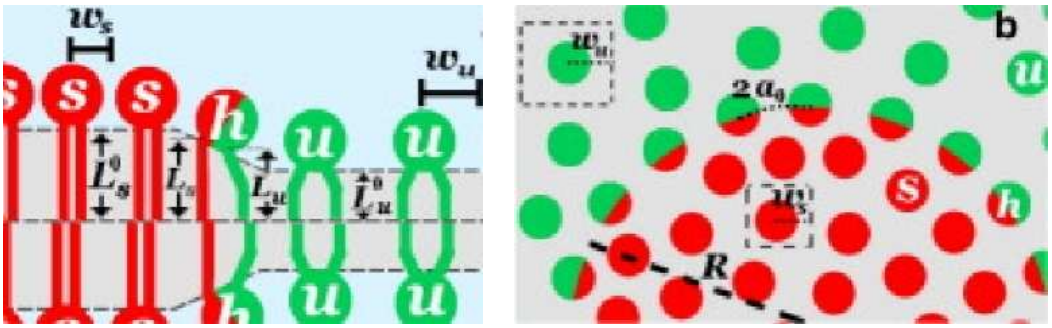

(a) (b)

Figure 4.3: (a) Shows the thickness mismatch with the hybrid lipid, h, at the interface. (b) shows the same bilayer as in (a) but looking down from above [7].

of the saturated and unsaturated chains respectively, w_s and w_u are the lengths that characterize the spacing of the saturated and unsaturated lipid heads respectively, and a is the headgroup spacing along the interface. Many of these parameters are lipid specific and can be measured experimentally. They add this term to a mean-field free energy of the system defined on a lattice pictured in Figure (4.4). They specifically look at modeling the interface

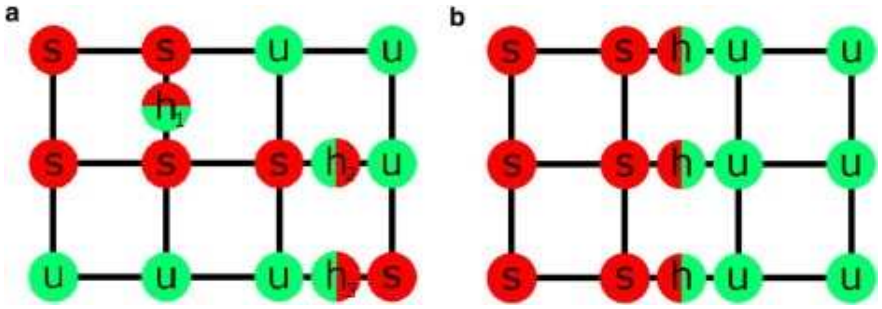

Figure 4.4: Schematic pictures for the lattice populated with saturated, unsaturated, and hybrid lipids [7].

of lipid domains. They conclude that the hybrid lipids drive the line tension to zero causing the formation of microdomains to stabilize. They are also able to measure the radius of microdomains by using information gathered on the curvature of the mircodomains. This model offers ideas to construct a better surface lipid raft model, by considering the curvature of mircodomains.

4.2.2. Discrete Model. Amazon, Goh, and Feigenson present a model based on line tension and curvature competition [4]. They develop the following Hamiltonian energy functional to model this interaction.

$$H = H_p + H_H + H_G \ ,$$

where H_p is the line tension term which is defined by multiplying the total perimeter of the phase boundary, L, by the constant energy per unit length, γ

$$H_p = \gamma L \ .$$

H_H is the mean curvature term given by

$$H_H = \int\int \kappa\left(\phi(x)\right)\left(H(x)\right)^2 \, dA \ ,$$

where $\kappa(\phi)$ is the local bending modulus. The last term H_G is the Gaussian curvature taken from the Helfrich functional

$$H_G = \int\int \bar{\kappa}\left(\phi(x)\right) G(x) \, dA \ .$$

Along with this energy functional they have two constraints to fix the volume and area of the vesicle. To determine the equillibrium shape of lipid rafts they use a discretizing scheme on a triangular lattice with an overall spherical topology, seen in Figure 4.5, and apply a Monte Carlo simulation.

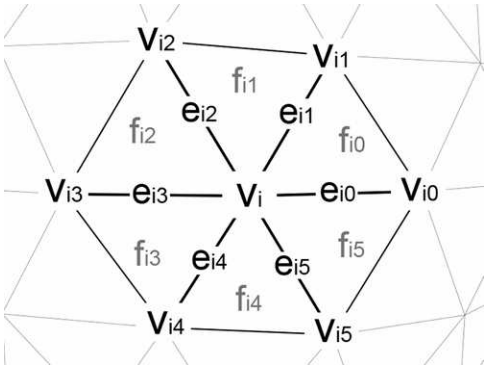

Figure 4.5: Triangulated lattice with vertices, edges, and faces [4].

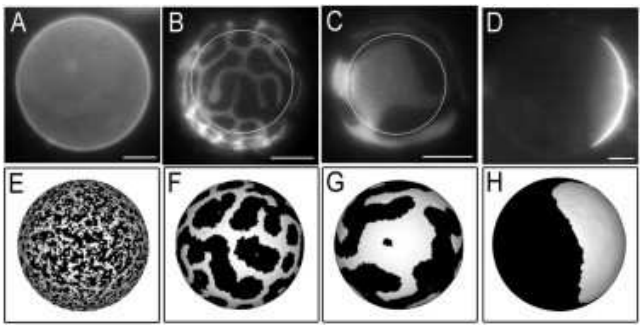

Figure 4.6: Patterns produced by purely changing the line tension. The top row are experimental phase patterns and the bottom row are simulated phase patterns [4].

In conclusion, they found the line tension to be the main factor in the location of domains. The patterns produced in the simulations presented in Figure 4.6 are the result of changing the line tension. This is a very good base for our model and will aid in comparison of results.

4.2.3. Course Grain Model. Meinhardt, Vink, and Schmid ,present a course grain model for multi-component lipid bilayers [44]. They have two main results. The first is showing the existence of a thermodynamically stable heterogeneous membrane phase with raft-like nanodomains using Monte-Carlo simulations os a coarse-grained model. The second is a model that explains this raft formation which is obtained by coupling the local composition and the monolayer curvature. The curvature is associated with an elastic bending

energy which in their simplified version is given by

$$F_{el} = k_c \delta c_0 \int dl\, \vec{n} \nabla u \ , \tag{17}$$

where $\vec{n}$ is the normal vector to the interface, δc_0 is a constant characterizing the curvature mismatch, and the line integral, $\int dl$, runs over all domains. They conclude that the curvature mismatch generates elastic interactions that supress global phase separation and stabilize the mircodomains. Their model was able to produce these stable microdomains.

CHAPTER 5

Electrostatics Model

Electrostatics have been seen to affect the phase separation in lipid rafts [40]. In this chapter we develop an electrostatics model of lipid rafts in which to show this effect. We consider the domain in Figure 5.1, where Ω is a 3-D domain, S is a surface in Ω, and ϕ is the chemical potential defined only on the surface.

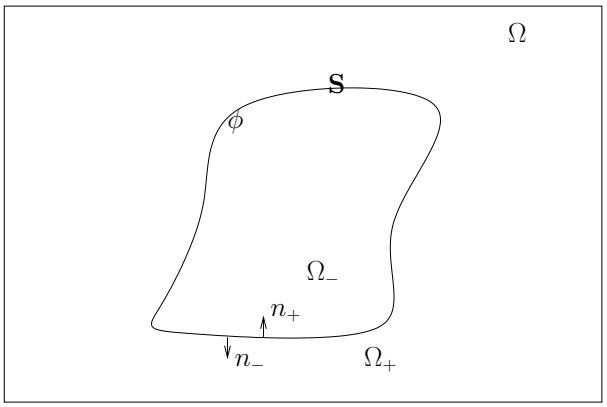

Figure 5.1: Ω is a 3D domain, S is a surface in Ω, and ϕ is the chemical potential defined on the surface

We can define the Ginzburg-Landau functional, as seen in Equation (1), over the surface, S, as

$$F(\phi) = \int_S \left(\frac{\sigma}{2} |\nabla_s \phi(x)|^2 + f(\phi) \right) ds \tag{18}$$

where $f(\phi)$ is a double well potential. We add to $F(\phi)$ in Equation (18) an electro-chemical energy term $\int_\Omega \frac{1}{2} |\nabla_s \psi|^2 dx$ defined over Ω to get

$$F(\phi) = \int_S \left(\frac{\sigma}{2} |\nabla_s \phi(x)|^2 + f(\phi) \right) ds + \int_\Omega \frac{1}{2} |\nabla_s \psi|^2 dx \ . \tag{19}$$

Note that the electro-chemical energy is defined in Ω but not on the surface, S, only. In order to transform this integral on Ω to a surface integral on S we will start with Poisson's

equation (20) to further develop the electro-chemical energy. Consider,

$$\begin{cases} -\nabla^2\psi = 0, \ \ on\ \Omega \\ \psi^+ = \psi^- \\ \left[\frac{\partial\psi}{\partial n}\right] = -(q_A\rho_A + q_B\rho_B) = -\rho(\phi), \ \ on\ S\ , \end{cases} \tag{20}$$

where ρ_A and ρ_B are the densities of particle A and particle B respectively and q_A and q_B are the charges on particle A and particle B respectively with the following definitions.

$$\begin{cases} \rho_A - \rho_B = \phi\ , \\ \rho_A + \rho_B = 1\ . \end{cases} \tag{21}$$

The solution to the Poisson's equation (20) is

$$\psi(x) = \int_S G(x - x_0)\rho(x_0)dx\ , \tag{22}$$

where $G(x - x_0)$ is the Green's function for the 3-D Laplace equation. In a domain, such as Ω, this solution depends on the boundary condition, $\rho(y)$, and we get the following nice result in Ω

$$\psi(x) = \int_\Omega G(x - y)\rho(y)dy\ ,$$

$$\Delta\psi(x) = \Delta\int_\Omega G(x - y)\rho(y)dy = \rho(y)\ .$$

However, on surfaces this solution no longer depends on the boundary conditions, $\rho(\phi)$. Thus, the property does not hold on S

$$u(x) = \int_S G(x - y)f(y)dy\ ,$$

$$\Delta_s u(x) = \Delta_s\int_S G(x - y)\rho(y)dy \neq \rho(y)\ .$$

This suggests that there is no explicit form for the electro-chemical term on S.

5.1. Domain Integral to Surface Integral

We now consider the electro-chemical term $\int_\Omega \frac{1}{2}|\nabla_s\psi|^2 dx$. To transform the integral on Ω to an integral on S we first put Poisson's equation in weak form.

$$\int_\Omega -\Delta\psi\psi = 0 \ .$$

Letting $\Omega = \Omega^+ + \Omega^-$ as represented in Figure 5.1 and integrating by parts we get

$$-\int_{\partial\Omega^+}(\nabla\psi\cdot n^+)\psi dx + \int_{\Omega^+}(\nabla\psi\cdot\nabla\psi) - \int_{\partial\Omega^-}(\nabla\psi\cdot n^-)\psi dx + \int_{\Omega^-}(\nabla\psi\cdot\nabla\psi) = 0 \ ,$$

That is

$$-\int_{\partial\Omega^+}\left(\nabla\psi\cdot n^+\right)\psi dx + \int_{\Omega^+}|\nabla\psi|^2 = \int_{\partial\Omega^-}\left(\nabla\psi\cdot n^-\right)\psi dx - \int_{\Omega^-}|\nabla\psi|^2 \ .$$

Notice that $n^+ = -n^-$ so we can write

$$\int_{\partial\Omega^+}\left(\nabla\psi\cdot n^-\right)\psi dx + \int_{\Omega^+}|\nabla\psi|^2 = \int_{\partial\Omega^-}\left(\nabla\psi\cdot n^-\right)\psi dx - \int_{\Omega^-}|\nabla\psi|^2 \ ,$$

and further

$$\int_\Omega |\nabla\psi|^2 = \int_{\partial\Omega}\left[\frac{\partial\psi}{\partial n}\right]\psi dx = \int_S \left(q_A\rho_A + q_B\rho_B\right)\psi ds \ .$$

Thus, the integral transformation is

$$\int_\Omega |\nabla\psi|^2\, dx = \int_S \left(q_A\rho_A + q_B\rho_B\right)\psi ds$$

Substituting this into the original formulation, Equation (19), we get

$$F(\phi) = \int_S \left(\frac{\sigma}{2}|\nabla_s\phi(x)|^2 + f(\phi)\right) ds + \frac{1}{2}\int_S \left(q_A\rho_A + q_B\rho_B\right)\psi ds \ .$$

Now let $\rho(\phi) = \left[\frac{\partial\psi}{\partial n}\right] = q_A\rho_A + q_B\rho_B$ we obtain,

$$\frac{1}{2}\int_S \left(\rho_A q_A + \rho_B q_B\right)\psi ds = \frac{1}{2}\int_S \rho(\phi)\psi ds \ ,$$

Substituting this into Equation (22), we get

$$\frac{1}{2}\int_S \rho(\phi)\psi ds = \frac{1}{2}\int_S \rho(\phi)\int_S G(x-x_0)\rho(x_0)ds \ .$$

Finally, with this relation the total energy defined in Equation (19) can be given as a quantity defined only on a surface as

$$F(\phi) = \int_S \left[\frac{\sigma}{2}|\nabla_s\phi(x)|^2 + f(\phi) + \frac{1}{2}\rho(\phi)\int_S G(x-x_0)\rho(x_0)ds\right] ds \ . \tag{23}$$

5.2. Variational Calculation

To minimize the total energy we need to derive the variation of the total energy. Using the definition of a functional derivative, for a general functional, $F(x)$:

$$\int \frac{\delta F}{\delta\phi}v(x) = \lim_{\epsilon\to 0}\frac{F(\phi+\epsilon v)-F(\phi)}{\epsilon} \ .$$

With our functional, F, in Equation (23) we have

$$F(\phi) = \int \frac{\sigma}{2}|\nabla_s\phi(x)|^2 + \int f(\phi) + \frac{1}{2}\int \rho(\phi)\int G(x-x_0)\rho(\phi)$$

$$F(\phi+\epsilon v) = \int \frac{\sigma}{2}|\nabla_s(\phi+\epsilon v)|^2 + \int f(\phi+\epsilon v) + \frac{1}{2}\int \rho(\phi+\epsilon v)\int G(x-x_0)\rho(\phi+\epsilon v)$$

where

$$\rho(\phi) = \frac{(q_a-q_b)}{2}\phi(x) + \frac{(q_a+q_b)}{2} \ , \qquad \rho(\phi+\epsilon v) = \frac{(q_a-q_b)}{2}(\phi(x)+\epsilon v) + \frac{(q_a+q_b)}{2} \ .$$

For simplicity we define

$$k = \frac{(q_a-q_b)}{2} \ , \qquad k' = \frac{(q_a+q_b)}{2} \ .$$

Then,

$$\rho(\phi) = k\phi(x) + k' \ , \qquad \rho(\phi+\epsilon v) = k(\phi(x)+\epsilon v) + k' = k\phi(x) + k\epsilon v + k' \ ,$$

and we have a simplified version of the variation:

$$F(\phi) = \int \frac{\sigma}{2}|\nabla_s \phi(x)|^2 + \int f(\phi) + \frac{1}{2}\int k\phi(x) + k' \int G(x - x_0)(k\phi(x) + k')$$

$$F(\phi+\epsilon v) = \int \frac{\sigma}{2}|\nabla_s (\phi+\epsilon v)|^2 + \int f(\phi+\epsilon v) + \frac{1}{2}\int k\phi(x) + k\epsilon v + k' \int G(x-x_0)(k\phi(x)+k\epsilon v+k')$$

Then the derivation of the variation is

(24)

$$\begin{aligned}
\int \frac{\delta F}{\delta \phi} v(x)\, dx &= \lim_{\epsilon \to 0} \frac{1}{\epsilon} \left(E(\phi + \epsilon v) - E(\phi)\right) \\
&= \lim_{\epsilon \to 0} \frac{1}{\epsilon} \left(\int \frac{\sigma}{2}|\nabla_s \phi(x)|^2 + \int f(\phi) \right) \\
&+ \lim_{\epsilon \to 0} \frac{1}{\epsilon} \frac{1}{2} \int k\phi(x) + k\epsilon v + k' \int G(x - x_0)(k\phi(x) + k\epsilon v + k') \\
&- \lim_{\epsilon \to 0} \frac{1}{\epsilon} \left(\int \frac{\sigma}{2}|\nabla_s (\phi + \epsilon v)|^2 + \int f(\phi + \epsilon v) \right) \\
&+ \lim_{\epsilon \to 0} \frac{1}{\epsilon} \left(\frac{1}{2} \int k\phi(x) + k' \int G(x - x_0)(k\phi(x) + k') \right) \\
&= \int \sigma \Delta \phi v + \int f'(\phi) v + \lim_{\epsilon \to 0} \frac{1}{\epsilon} \left(\frac{1}{2} \int k\phi(x) \int G(x - x_0) k\epsilon v \right) \\
&+ \frac{1}{\epsilon} \left(\frac{1}{2} \int k\epsilon v \int G(x - x_0)(k\phi(x) + k\epsilon v + k') \right) + \frac{1}{\epsilon} \left(\frac{1}{2} \int k' \int G(x - x_0) k\epsilon v \right) \\
&= \int \sigma \Delta \phi v + \int f'(\phi) v + \lim_{\epsilon \to 0} \frac{1}{2} \int k\phi(x) \int G(x - x_0) kv + \\
&+ \lim_{\epsilon \to 0} \left(\frac{1}{2} \int kv \int G(x - x_0)(k\phi(x) + k\epsilon v + k') + \frac{1}{2} \int k' \int G(x - x_0) kv \right) \\
&= \int \sigma \Delta \phi v + \int f'(\phi) v + \frac{1}{2} \int k\phi(x) \int G(x - x_0) kv \\
&+ \frac{1}{2} \int kv \int G(x - x_0)(k\phi(x) + k') + \frac{1}{2} \int k' \int G(x - x_0) kv \\
&= \int \sigma \Delta \phi v + \int f'(\phi) v + \frac{1}{2} \int (k\phi(x) + k') \int G(x - x_0) kv \\
&+ \frac{1}{2} \int kv \int G(x - x_0)(k\phi(x) + k')
\end{aligned}$$

$$
\begin{aligned}
&= \int \sigma \Delta \phi v + \int f'(\phi) v + \frac{1}{2} \int \rho(\phi) \int G(x - x_0) \frac{d\rho}{d\phi} v \\
&= + \frac{1}{2} \int \frac{d\rho}{d\phi} v \int G(x - x_0) \rho(\phi) \\
&= \int \sigma \Delta \phi v + \int f'(\phi) v + \int \frac{d\rho}{d\phi} \int G(x - x_0) \rho(\phi) v
\end{aligned}
$$

which implies:

$$
\int \frac{\delta F}{\delta \phi} = \int_S \sigma \Delta \phi \, dx + \int_S f'(\phi) \, dx + \int_S \frac{d\rho}{d\phi} \int_S G(x - y) \rho(y) dy
$$

5.3. Complete Model of Electrostatic Mediated Lipid Raft Formation

The total energy functional is

$$
F(\phi) = \int_S \left[\frac{\sigma}{2} |\nabla_s \phi(x)|^2 + f(\phi) + \frac{1}{2} \rho(\phi) \int_S G(x - x_0) \rho(x_0) ds \right] ds \tag{25}
$$

with the total variation

$$
\frac{\delta F}{\delta \phi} = f'(\phi) - \sigma \Delta \phi + \int_S G(x, y) \rho(y) dy \frac{d\rho}{d\phi} \, .
$$

Applying Fick's Law, the change in ϕ over time is given by

$$
\frac{\partial \phi}{\partial t} = \Delta_s \left(f'(\phi) - \sigma \Delta \phi + \int_S G(x, y) \rho(y) dy \frac{d\rho}{d\phi} \right) \, ,
$$

where

$$
\rho(y) = \left(\frac{q_A - q_B}{2} \right) \phi(y) + \frac{1}{2} q_A + \frac{1}{2} q_B
$$

and

$$
\frac{d\rho}{d\phi} = \frac{q_A - q_B}{2} \, .
$$

To summarize the final problem is to find ϕ such that:

$$
\begin{cases}
\frac{\partial \phi}{\partial t} = \Delta_s f'(\phi) - \Delta_s^2 \phi + \Delta_s \psi \frac{d\rho}{d\phi} \\
\psi = \int_S G(x.y) \rho(y) dy
\end{cases} \tag{26}
$$

where $G(x, y)$ is the Green's function for the 3-D Laplace equation. We will develop numerical techniques to solve Equation (68) in Chapter 8.

CHAPTER 6

Geodesic Curvature Model of Lipid Rafts

Recently, it has been shown that the free energy associated with the curvature of microdomain patterns is a driving energy in the formation of microdomains. This is discussed in detail in Chapter 2. This motivates us to develop and implement a model containing the free energy associated with the curvature of microdomains. We start with the free energy associated with the curvature of lipid-lipid interfaces developed in [7, 8]:

$$F(\phi) = \int_S g(H)\, ds$$

where $g(H)$ is defined as

$$g = \left(\frac{V_s}{a w_s\ (1 - 1/2\, w_s\, H)} - L_S \right)^2 + \left(\frac{V_u}{a w_u\ (1 + 1/2\, w_u\, H)} - L_u \right)^2 + \left(-\frac{V_s}{a w_s\ (1 - 1/2\, w_s\, H)} + \frac{V_u}{a w_u\ (1 + 1/2\, w_u\, H)} \right)^2 \tag{27}$$

Where L_s and L_u is the length of the saturated chain of the hybrid lipid and the unsaturated chain of the hybrid chain respectively. H is the geodesic curvature, V_s and V_u are the volumes of the saturated and unsaturated chains respectively, w_s and w_u are the lengths that characterize the spacing of the saturated and unsaturated lipid heads respectively, and a is the headgroup spacing along the interface. This free energy is highly nonlinear and has a unique global minimum so we can approximate the curvature energy density, $g(H)$, near the minimum, $H = H_0$, using a Taylor approximation. This Taylor approximation is plotted against the original function in Figure 6.1 and the approximation is listed below

$$g(H) \approx g(H_0) + g'(H_0)\,(H - H_0) + \frac{1}{2} g''(H_0)\,(H - H_0)^2$$

Define

$$a = g(H_0) - (H_0)g'(H_0) + \frac{H_0^2}{2} g''(H_0) \quad b = -g'(H_0) + (H_0)g''(H_0) \quad c = \frac{1}{2} g''(H_0)$$

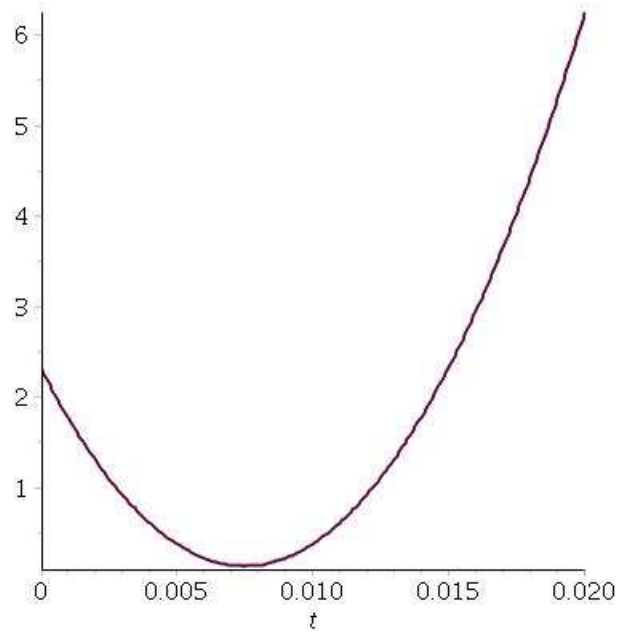

Figure 6.1: $g(H)$ near its minimum and the Taylor approximation of $g(H)$ plotted together for parameters $V_u = 72$, $V_s = 896$, $L_u = 27.36$, $L_s = 28$, $w_u = 6$, $w_s = 5.65$.

Then we can write $g(H)$ as

$$g(H) \approx a - b\,H + c\,H^2$$

By completing the square we can write $g(H)$ as

$$g(H) = (H - \tilde{H}_0)^2 + a - \tilde{H}_0^2 \tag{28}$$

Where $\tilde{H}_0 = \frac{b}{2}$ is the spontaneous geodesic curvature. Then, the energy functional defined on a contour, C, is given by

$$\int_C (H - \tilde{H}_0)^2 + a - \tilde{H}_0^2\, dx\ . \tag{29}$$

Note that the minimization of Equation (30) is equivalent to minimizing

$$\int_C (H - H_0)^2\, dx\ , \tag{30}$$

where H_0 is the spontaneous geodesic curvature, since the minimization is driven by this term. Thus, the total energy functional is

$$F(\phi) = \int_C (H - H_0)^2 ds \ . \tag{31}$$

The task now becomes to write the contour integral in terms of a surface integral and to define H in terms of the phase field function, ϕ, defined on S.

6.1. Countour Integral to Surface Integral

To begin the derivation of the energy functional in terms of ϕ on the surface, S, we note that Equation (31) is the Lagrangian formulation of the energy. A possible alternate formulation is the Eulerian formulation given by

$$\int_S \frac{k\epsilon}{2} \left(\Delta_s \phi + \frac{1}{\epsilon^2} \left(\phi + H_c \epsilon \right) \left(1 - \phi^2 \right) \right)^2 dx \tag{32}$$

where $H_c = \sqrt{2} H_o$. Since the Eulerian formulation is a surface integral it would suffice to show these two forms are equivalent up to a constant. This equivalence is analog to the equivalence between the Canham-Helfrich-Evans bending energy and the membrane elastic energy [19]. We first define the phase field function $\phi = \tanh\left(\frac{d(x)}{\epsilon\sqrt{2}}\right)$ where $d(x)$ is the signed distance for any point on the surface S to the contour C and ϵ is the width of the transition layer between lipid phases. Then,

$$\nabla \phi = \frac{1}{\epsilon} q' \nabla_s d \ , \qquad \Delta_s \phi = \frac{1}{\epsilon} q'' \nabla_s d \cdot \nabla_s d + \frac{1}{\epsilon} q' \Delta_s d$$

$$q(x) = \tanh\left(\frac{x}{\sqrt{2}}\right), \ q'(x) = \left(1 - \tanh^2\left(\frac{x}{\sqrt{2}}\right)\right)/\sqrt{2}, \ q''(x) = -2\tanh\left(\frac{x}{\sqrt{2}}\right)\operatorname{sech}^2\left(\frac{x}{\sqrt{2}}\right)$$

The geodesic curvature of a contour is given by

$$H = \nabla_s \cdot n$$

where n is the bi-normal vector to the contour, C. Since $n = \nabla_s d$ we have

$$H = \nabla_s \cdot \nabla_s d = \Delta_s d \ .$$

Using the relations given in Equation (33) we find that

$$\Delta_s d = \frac{\epsilon}{q'} \Delta_s \phi - \frac{1}{q'} q'' \nabla_s d \cdot \nabla_s d$$

and

$$\nabla_s d = \frac{\epsilon}{q'} \nabla_s \phi \ .$$

Together we have

$$\Delta_s d = \frac{\epsilon}{q'} \Delta_s \phi - \frac{1}{q'} q'' \frac{\epsilon}{q'} \nabla_s \phi \cdot \frac{\epsilon}{q'} \nabla_s \phi \ .$$

Writing q' and q'' in terms of q we can rewrite this as

$$\Delta_s d = \frac{\sqrt{2}\epsilon}{1 - q^2} \left(\Delta_s \phi + \frac{2q}{1 - q^2} \nabla_s \phi \cdot \nabla_s \phi \right) \ .$$

Then the curvature of a countour is given by

$$H = \frac{\sqrt{2}\epsilon}{1 - q^2} \left(\Delta_s \phi + \frac{2q}{1 - q^2} \nabla_s \phi \cdot \nabla_s \phi \right) \ .$$

Replacing q with ϕ we have the final form as:

$$\begin{aligned} H &= \frac{\sqrt{2}\epsilon}{1 - \phi^2} \left(\Delta_s \phi + \frac{2\phi}{1 - \phi^2} |\nabla_s \phi|^2 \right) \ , \\ &= \frac{\sqrt{2}\epsilon}{1 - \phi^2} \left(\Delta_s \phi + \frac{1}{\epsilon^2} \left(1 - \phi^2 \right) \phi \right) \ . \end{aligned} \tag{33}$$

Following the procedure for transforming a contour integral to a surface integral, [19], we consider the following integral:

(34)

$$\begin{aligned}
\int_{-\infty}^{\infty}\left(1-q^2\left(\frac{x}{\sqrt{2}\epsilon}\right)\right)^2 dx &= 2\int_0^{\infty}\operatorname{sech}^4\left(\frac{x}{\sqrt{2}\epsilon}\right)dx \\
&= \frac{\sqrt{2}\epsilon}{3}\left(3\sinh\left(\frac{x}{\sqrt{2}\epsilon}\right)+\sinh\left(\frac{3x}{\sqrt{2}\epsilon}\right)\sinh^3\left(\frac{x}{\sqrt{2}\epsilon}\right)\right)\Bigg|_{x=0}^{\infty} \\
&= \frac{\sqrt{2}\epsilon}{3}\lim_{x\to\infty}\left(3\sinh\left(\frac{x}{\sqrt{2}\epsilon}\right)+\sinh\left(\frac{3x}{\sqrt{2}\epsilon}\right)\sinh^3\left(\frac{x}{\sqrt{2}\epsilon}\right)\right) \\
&= \frac{\sqrt{2}\epsilon}{3}\lim_{x\to\infty}\left(\frac{3}{2}\left(e^{\frac{x}{\sqrt{2}\epsilon}}-e^{\frac{x}{\sqrt{2}\epsilon}}\right)+\frac{1}{2}e^{\frac{3x}{\sqrt{2}\epsilon}}-e^{\frac{-3x}{\sqrt{2}\epsilon}}\right)\left(\frac{2}{e^{\frac{x}{\sqrt{2}\epsilon}}+e^{\frac{-x}{\sqrt{2}\epsilon}}}\right)^3 \\
&= \frac{\sqrt{2}\epsilon}{3}\lim_{x\to\infty}\left(\frac{4e^{\frac{3x}{\sqrt{2}\epsilon}}+\text{Lower order terms}}{e^{\frac{3x}{\sqrt{2}\epsilon}}+\text{Lower order terms}}\right) \\
&= \frac{4\sqrt{2}\epsilon}{3}\ ,
\end{aligned}$$

which implies

(35)
$$\frac{3}{4\sqrt{2}\epsilon}\int_{-\infty}^{\infty}\left(1-q^2\left(\frac{x}{\sqrt{2}\epsilon}\right)\right)^2 dx = 1\ .$$

Multiplying Equation (30) by Equation (35) we get

(36)

$$\begin{aligned}
\int_C (H-H_0)^2 dx &= \frac{3}{4\sqrt{2}\epsilon}\int_{-\infty}^{\infty}\left(1-q^2\left(\frac{x}{\sqrt{2}\epsilon}\right)\right)^2 dx \int_C (H-H_0)^2 dx \\
&= \frac{3}{4\sqrt{2}\epsilon}\int_{-\infty}^{\infty}\left(1-q^2\left(\frac{x}{\sqrt{2}\epsilon}\right)\right)^2 dx \int_C \left(\frac{\sqrt{2}\epsilon}{1-q^2}\left(\Delta\phi+\frac{2q}{1-q^2}\nabla\phi\cdot\nabla\phi\right)-H_0\right)^2 dx \\
&\sim \frac{3}{4\sqrt{2}\epsilon}\int_S \left(1-q^2\left(\frac{x}{\sqrt{2}\epsilon}\right)\right)^2 \left(\frac{\sqrt{2}\epsilon}{1-q^2}\left(\Delta\phi+\frac{2q}{1-q^2}\nabla\phi\cdot\nabla\phi\right)-H_0\right)^2 dx \\
&= \frac{3}{8\sqrt{2}\epsilon}\int_S \left(\epsilon\Delta\phi+\frac{1}{\epsilon}\phi\left(1-\phi^2\right)+\sqrt{2}(1-\phi^2)H_0\right)^2 dx \\
&= \frac{3}{4\sqrt{2}}\int_S \frac{\epsilon}{2}\left(\Delta\phi+\frac{1}{\epsilon^2}\left(\phi+H_c\epsilon\right)\left(1-\phi^2\right)\right)^2 dx \ ,
\end{aligned}$$

where $H_c = \sqrt{2}H_0$. This shows that the two forms of the energy differ by a constant multiple, which suffices for giving the complete energy functional over the surface, S, as

$$F(\phi) = \frac{3k}{4\sqrt{2}}\int_S \frac{\epsilon}{2}\left(\Delta_s\phi+\frac{1}{\epsilon^2}\left(\phi+H_c\epsilon\right)\left(1-\phi^2\right)\right)^2 dx \ . \tag{37}$$

The model is subject to a mass concentration constraint given by

$$A(\phi) = \int_S \phi(x) ds = constant$$

6.2. First Variation of Energy Functional

To minimize the total energy we need to derive the variation of the total energy, $F(\phi)$, as defined in Equation (37). Using the definition of a functional derivative, for a general functional, $F(x)$:

$$\int \frac{\delta F}{\delta\phi} v(x)\ dx = \left[\frac{d}{d\tau}F(\phi+\tau v)\right]\Bigg|_{\tau=0}$$

and substituting in the functional from Equation (37) the variational derivative follows

$$F(\phi+\tau v) = \frac{3k}{4\sqrt{2}}\int_S \frac{\epsilon}{2}\left(\Delta_s(\phi+\tau v)+\frac{1}{\epsilon^2}\left((\phi+\tau v)+H_c\epsilon\right)\left(1-(\phi+\tau v)^2\right)\right)^2 dx \ , \tag{38}$$

(39)

$$\frac{d}{d\tau}F(\phi+\tau v) = \frac{d}{d\tau}\frac{3k}{4\sqrt{2}}\int_S \frac{\epsilon}{2}\left(\Delta_s(\phi+\tau v) + \frac{1}{\epsilon^2}\left((\phi+\tau v) + H_c\epsilon\right)\left(1-(\phi+\tau v)^2\right)\right)^2 dx \Bigg|_{\tau=0}$$

$$= \int_S k\left(\epsilon\Delta_s\phi - \frac{1}{\epsilon}\left(\phi+H_c\epsilon\right)\left(\phi^2-1\right)\right)\left(\Delta_s v + \frac{1}{\epsilon^2}v\left[1-\phi^2+\left(\phi+H_c\epsilon\right)\left(-2\phi\right)\right]\right) dx$$

$$= \int_S kW\left(\Delta_s v + \frac{1}{\epsilon^2}v\left[1-\phi^2+\left(\phi+H_c\epsilon\right)\left(-2\phi\right)\right]\right) dx$$

$$= \int_S -k\nabla_s W\cdot\nabla_s v dx - \int_S k\frac{1}{\epsilon^2}v[3\phi^2+2H_c\epsilon\phi-1]g\,dx$$

$$= \int_S k\Delta_s W v\,dx - \int_S k\frac{1}{\epsilon^2}v[3\phi^2+2H_c\epsilon\phi-1]g\,dx\ .$$

The total variation is then

$$\frac{\delta F}{\delta\phi} = k\left[\Delta_s W - \frac{1}{\epsilon^2}\left(3\phi^2+2H_c\epsilon\phi-1\right)W\right]\ ,$$

where

$$W = \epsilon\Delta_s\phi - \frac{1}{\epsilon}\left(\phi+H_c\epsilon\right)\left(\phi^2-1\right)\ .$$

Let W_L and W_N be the linear and nonlinear parts of W, respectively. Then

$$W_L = \epsilon\Delta_s\phi + \frac{1}{\epsilon}\phi + H_c\ , \qquad W_N = -\frac{1}{\epsilon}\phi^3 - H_c\phi^2$$

Then the linear part, F_L, of $\frac{\delta F}{\delta\phi}$ is given by

$$F_L = k\Delta_s W_L + \frac{k}{\epsilon^2}W_L\ , \tag{40}$$

and the nonlinear part, F_N, is given by

$$F_N = k\Delta_s W_N - \frac{k}{\epsilon^2}\left(3\phi^2+2H_c\epsilon\phi\right)W_N - \frac{k}{\epsilon^2}W_L\left(3\phi^2+2H_c\epsilon\phi\right)\ . \tag{41}$$

Totally,

$$\frac{\delta F}{\delta\phi} = F_L + F_N = k\Delta W_L + \frac{k}{\epsilon^2}W_L + k\Delta W_N - \frac{k}{\epsilon^2}\left(3\phi^2+2H_c\epsilon\phi\right)W_N - \frac{k}{\epsilon^2}W_L\left(3\phi^2+2H_c\epsilon\phi\right)\ .$$

The variation in its fully expanded form is

$$\begin{aligned}(42)\qquad \frac{\delta F}{\delta \phi} =& k\epsilon\Delta_s^2\phi - \frac{2k}{\epsilon}\Delta_s\phi + \left(\frac{2H_c^2k}{\epsilon} + \frac{k}{\epsilon^3}\right)\phi \\ &+ \frac{3k}{\epsilon^3}\phi^5 + \frac{5kH_c}{\epsilon^2}\phi^4 - \left(\frac{4k}{\epsilon^3} + \frac{2H_c^2k}{\epsilon}\right)\phi^3 \\ &- \frac{6H_ck}{\epsilon^2}\phi^2 - \frac{k}{\epsilon}\Delta_s\phi^3 - kH_c\Delta_s\phi^2 - \frac{3k}{\epsilon}\phi^2\Delta_s\phi - 2H_ck\phi\Delta_s\phi + \frac{H_ck}{\epsilon^2}\ .\end{aligned}$$

Using the identities derived in Equations (13) and (14) we can rewrite the variation as

$$\begin{aligned}(43)\qquad \frac{\delta F}{\delta \phi} =& k\epsilon\Delta_s^2\phi - \frac{2k}{\epsilon}\Delta_s\phi - \left(\frac{2C^2k}{\epsilon} + \frac{k}{\epsilon^3}\right)\phi \\ &+ \frac{3k}{\epsilon^3}\phi^5 + \frac{5kC}{\epsilon^2}\phi^4 - \left(\frac{4k}{\epsilon^3} + \frac{2C^2k}{\epsilon}\right)\phi^3 \\ &- \frac{6Ck}{\epsilon^2}\phi^2 + \frac{Ck}{\epsilon^2} - \left(4kC\phi + \frac{6k}{\epsilon}\phi^2\right)\Delta_s\phi - \left(\frac{6k}{\epsilon}\phi + 2kC\right)|\nabla_s\phi|^2\end{aligned}$$

And note the variation of the concentration constraint is

$$\frac{\partial A}{\partial \phi} = 1$$

6.3. Complete Model of Geodesic Curvature Modulated Lipid Raft Formation

Therefore, the gradient of the flow of the phase field function is given by

$$(44)\qquad \frac{\partial \phi}{\partial t} = -\frac{\delta F}{\delta \phi} + \lambda\frac{\partial A(\phi)}{\phi}\ ,$$

where λ is a Lagrange multiplier used to ensure the conservation of ϕ. We can derive an expression for λ by integrating Equation (44) and noting that $\int_S \frac{\partial \phi}{\partial t} = 0$. Hence

$$(45)\qquad 0 = -\int_S \frac{\delta F}{\delta \phi} + \int_S \lambda\ .$$

Then

$$\int_S \lambda = \int_S \frac{\delta F}{\delta \phi} \ , \tag{46}$$

so

$$\lambda |S| = \int_S \frac{\delta F}{\delta \phi} \ , \tag{47}$$

That is

$$\lambda = \frac{1}{|S|} \int_S \frac{\delta F}{\delta \phi} \ . \tag{48}$$

We can then rewrite the gradient flow equation as follows

$$\frac{\partial \phi}{\partial t} = -\frac{\delta F}{\delta \phi} + \frac{1}{|S|} \int_S \frac{\delta F}{\delta \phi} \tag{49}$$

We will develop a surface finite element method in Chapter 8 to solve the gradient flow equation.

CHAPTER 7

Review of Numerical Methods for Surface PDEs

Many of the models previously discussed contain a fourth order differential operator, also known as a bilaplacian or biharmonic operator. This term poses challenges to developing numerical methods to minimize the various free energy functionals presented in previous chapters. For general surface PDE's there are several numerical techniques including finite difference, finite element, spectral methods, finite volume, and embedded domain methods [20, 21, 29, 45, 35, 36, 12, 14, 23, 24, 28, 27, 34, 37, 38, 17, 56, 57]. We will give a brief overview of these numerical methods.

7.1. Mixed Finite Element Method

The fourth order Cahn-Hilliard equation can be reduced to a system of second order equations by introducing an intermediate variable. Mixed finite element methods can then be applied to solve this system [20, 21]. Let p be the chemical potential as in Equation (3). Let S be an open connected and bounded surface in $\mathbb{R}^3$ and let $\phi = \phi(x,t) \in H^1(S)$ Then we can reduce the Cahn-Hilliard equation into the following system:

$$\begin{cases} \frac{\partial \phi}{\partial t} = \Delta_s p \\ p = \frac{\partial F}{\partial \phi} = f'(\phi) - \sigma \Delta_s \phi \ , \end{cases} \tag{50}$$

with boundary conditions $\phi(x) = 0$ and $p(x) = 0$ for $x \in \partial S$. Let $U \subset S$ be the continuous piecewise linear function finite element space. Then the fully discrete approximation problem is:

Find $(\phi_{n+1}, P_n) \in U^2$ for $n = 0, 1, ..., N$ such that for any $V, W \in U$:

$$\begin{cases} (\delta_t \phi^n, V) + (\nabla P_n, \nabla V) = 0, \\ -(P_n, W) + \sigma(\nabla \phi_{n+\frac{1}{2}}, \nabla W) + (\tilde{\phi}(\phi_n, \phi_{n+1}), W) = 0 \end{cases} \tag{51}$$

where N is the number of timesteps, Δt is the step size in time, and

$$\phi_{n+\frac{1}{2}} = \frac{\phi_n + \phi_{n+1}}{2} \ ,$$

$$\delta_t \phi^n = \frac{\phi_{n+1} - \phi_n}{\Delta t} \ ,$$

$$\tilde{\phi}(x,y) = \begin{cases} \dfrac{f(x) - f(y)}{x - y} \ , & x \neq y \ , \\ \phi(x) \ , & x = y \ . \end{cases}$$

Convergent numerical results for the Cahn-Hilliard equation on a closed sphere at different time steps have been obtained by using this approach shown in Figure 7.1

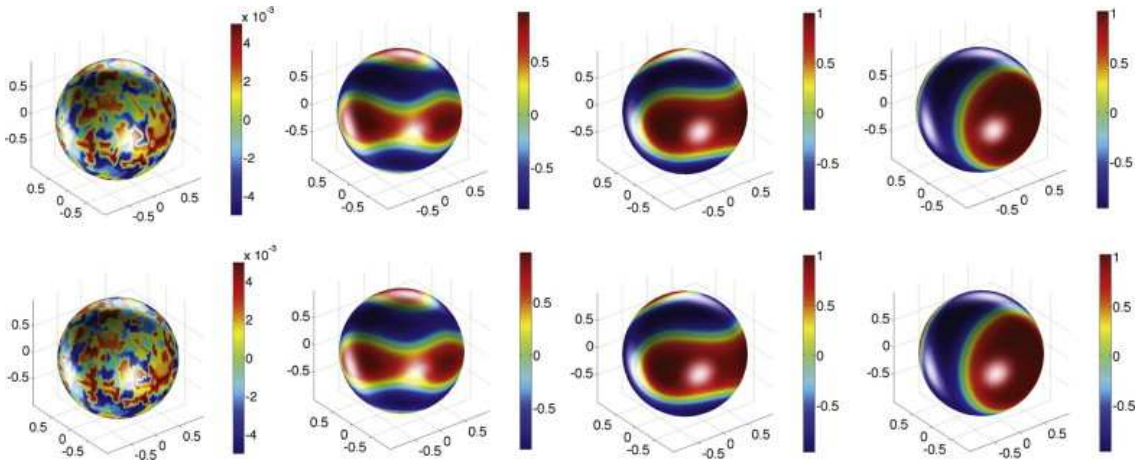

Figure 7.1: Solutions to the Cahn-Hilliard equation using a mixed finite element method at $t = 0, 1, 2, 5$. The top image is simulated on a mesh with 2018 nodes and the bottom image is simulated on a mesh with 8066 nodes [20].

It is noticed that the coupled system, Equation (51), can be integrated by neither an explicit or implicit method. When an explicit method is used a very small timestep has to be adopted due to the stability constraint. Interior iterations between the coupled equations are necessary if implicit methods are used. This motivates us to develop alternative efficient numerical techniques.

7.2. Spherical Finite Difference Methods

When the surfaces entail a global 2-D parameterization, finite difference methods can be applied to the fourth order equation directly without order reduction. Finite difference methods have been effective for such surfaces. Figure 7.2 shows a spherical-polar coordinate

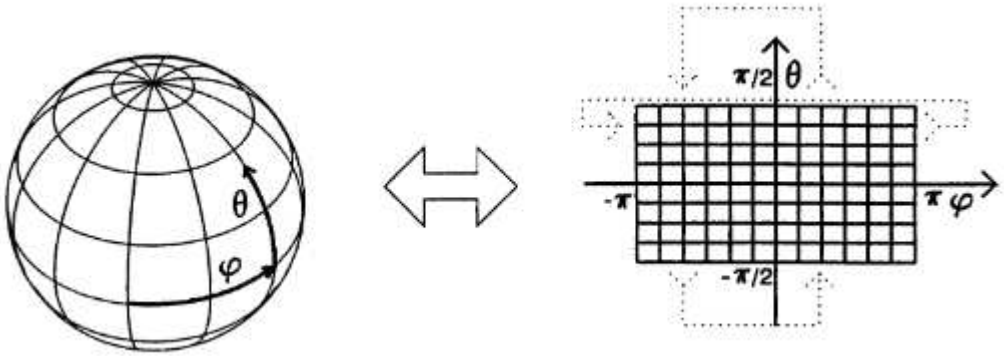

Figure 7.2: Grid arrangement and periodicities for spherical coordinates [29]

system. The dotted arrows indicate how the data repeats periodically. 1-D finite difference discretization can be applied to ρ and θ directions independently. Singularities at the poles can pose numerical difficulties for which we turn to [45] for an elegant treatment. We first derive the Cahn-Hilliard equations in spherical coordinates. The biharmonic term is

(52)
$$\Delta^2 u = u_\rho \left[\frac{\cos\rho}{\sin^3\rho} + 2\cot\rho\right] + \frac{4u_{\theta\theta}}{\sin^4\rho} - u_{\rho\rho}\cot^2\rho + 2u_{\rho\rho\rho}\cot\rho + u_{\rho\rho\rho\rho} + \frac{u_{\theta\theta\theta\theta}}{\sin^4\rho} + 2\frac{u_{\rho\rho\theta\theta}}{\sin^2\rho} - 2\frac{u_{\rho\theta\theta}\cos\rho}{\sin^3\rho} \ .$$

Lumping together all terms of the Cahn-Hilliard equation we get

$$\begin{aligned}(53)\quad \frac{\partial u}{\partial t} =& u_\rho \left[\frac{\cos\rho}{\sin^3\rho} + 2\cot\rho\right] + \frac{4u_{\theta\theta}}{\sin^4\rho} - u_{\rho\rho}\cot^2\rho + 2u_{\rho\rho\rho}\cot\rho + u_{\rho\rho\rho\rho} + \frac{u_{\theta\theta\theta\theta}}{\sin^4\rho} \\ &+ 2\frac{u_{\rho\rho\theta\theta}}{\sin^2\rho} - 2\frac{u_{\rho\theta\theta}\cos\rho}{\sin^3\rho} + (u^3)_\rho\cot\rho + \frac{(u^3)_{\theta\theta}}{\sin^2\rho} + (u^3)_{\rho\rho} - u_\rho\cot\rho + \frac{u_{\theta\theta}}{\sin^2\rho} + u_{\rho\rho} \ .\end{aligned}$$

To find the finite difference scheme near the poles we use a polar coordinate system as shown in Figure 7.3:

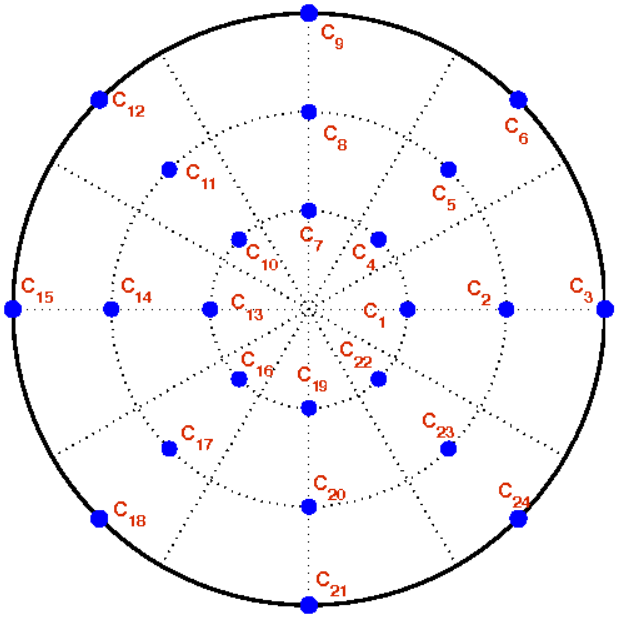

Figure 7.3: Finite difference scheme in polar coordinates near a pole.

The fourth order term in polar coordinates is

$$\Delta^2 u = u_{rrrr} + \frac{2}{r^2}u_{rr\theta\theta} + \frac{1}{r^4}u_{\theta\theta\theta\theta} + \frac{2}{r}u_{rrr} - \frac{2}{r^3}u_{r\theta\theta} - \frac{1}{r^2}u_{rr} + \frac{4}{r^4}u_{\theta\theta} + \frac{1}{r^3}u_r \ . \tag{54}$$

Along with the rest of the terms we have the Cahn-Hilliard equation in polar coordinates.

$$\begin{aligned}\frac{\partial u}{\partial t} =& u_{rrrr} + \frac{2}{r^2}u_{rr\theta\theta} + \frac{1}{r^4}u_{\theta\theta\theta\theta} + \frac{2}{r}u_{rrr} - \frac{2}{r^3}u_{r\theta\theta} - \frac{1}{r^2}u_{rr} + \frac{4}{r^4}u_{\theta\theta} + \frac{1}{r^3}u_r \\ &+ \frac{1}{r}(u^3)_r + (u^3)_{rr} + \frac{1}{r^2}(u^3)_{\theta\theta} - \frac{1}{r}u_r - u_{rr} - \frac{1}{r^2}u_{\theta\theta} \ .\end{aligned} \tag{55}$$

To find the finite difference scheme near the pole we define a new polar coordinate as

$$\tilde{r}(r,\theta) = \begin{cases} r \ , & 0 \le \theta < \pi \ , \\ -r \ , & \pi \le \theta < 2\pi \ , \end{cases}$$

over both positive and negative radius. Differentiation is done with respect to the new coordinate $\tilde{r}$.

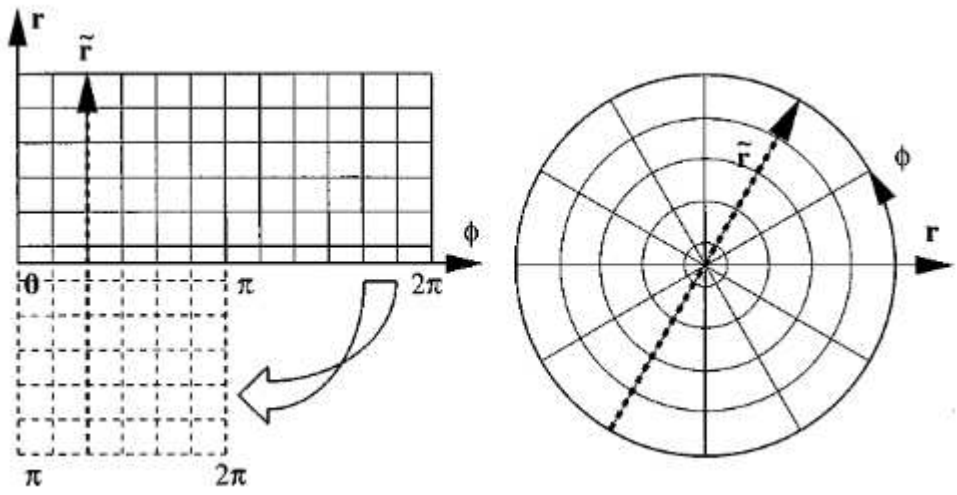

Figure 7.4: Computational and physical domains [45]

Vector and scalar quantities near the pole must be transformed using these rules:

(1) for $0 \leq \theta < \pi$ all quantities are the same in both coordinate systems

(2) for $\pi \leq \theta < 2\pi$ we multiply any polar components of a vector quantity, radial derivative, and any r by -1.

For example, to approximate

$$\frac{\partial(v_r v_\theta)}{\partial r}$$

near the poles we apply the aforementioned transformation for $\pi \leq \theta < 2\pi$ to get:

$$-\frac{\partial(-v_r v_\theta)}{\partial - r} = -\frac{\partial(v_r v_\theta)}{\partial r}$$

The signs change for $\pi \leq \theta < 2\pi$ but nothing changes for $0 \leq \theta < \pi$. The transformation is only used to calculate radial derivatives. A disadvantage to using an a finite difference scheme is that the domain has to be globally parameterizable. This really limits the types of domains, especially more physical domains, that can be used.

7.3. Embedded Domains

Deckelnick, Elliott, and Ranner develop an unfitted finite element method for approximating the solution of surface PDE's using bulk finite elements [17, 18, 50]. The idea behind embedded domain methods is a n-dimensional hypersurface is embedded in a polyhedral domain in $\mathbb{R}^{n+1}$ discritized by a union of $(n+1)$- simplices, as seen in Figure 7.5 Continuous piece-wise linear finite element functions are used for the finite element space. The authors combine the finite element method with discrete sharp interfaces and narrow bands to give a finite element method for parabolic equations on evolving surfaces.

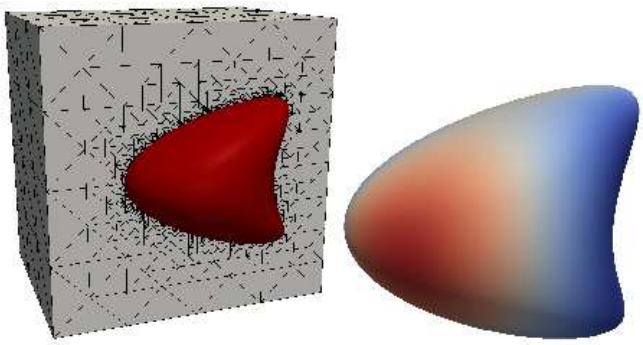

Figure 7.5: Example plots of computation domain and solution given in [17].

These methods works well for elliptic equations with advection/convection on evolving surfaces. The downfall is the memory and storage needed for the method and the method can have long run times. Although the method could be applied in subsequent projects it is not optimal for the problems presented in the lipid raft models.

CHAPTER 8

Surface Finite Element Method and Implementation

In this chapter we develop a C^0 interior penalty surface finite element method and an implicit time iteration scheme for solving the electrostatic and geodesic curvature models presented in Chapters 5 and 7. Our method is a generalization of a C^0 interior penalty discontinuous Galerkin method for the 2-D Cahn-Hilliard equation [6] to fourth order partial differential equations on arbitrary surfaces.

8.1. Electrostatics Model

8.1.1. C^0 Interior Penalty Surface Finite Element Method. Let $S \subset \mathbb{R}^3$ be a bounded polygonal surface and $\mathbb{V} = \{v \in H^2(S) | \frac{\partial v}{\partial n} = 0 \; on \, \partial S\}$, where $\frac{\partial v}{\partial n}$ is the outward normal derivative. Then the electrostatics model presented in Chapter 5 reads as:
Find $\phi \in \mathbb{V}$ such that

$$\begin{cases} \frac{\partial \phi}{\partial t} = \Delta_s f'(\phi) - \sigma \Delta_s^2 \phi + \Delta_s \psi \frac{d\rho}{d\phi} \ , \\ \psi = \int_S G(x.y)\rho(y)dy \ , \end{cases} \tag{56}$$

Consider the steady state problem,

$$\begin{cases} 0 = \Delta_s f'(\phi) - \sigma \Delta_s^2 \phi + \Delta_s \psi \frac{d\rho}{d\phi} \ , \\ \psi = \int_S G(x.y)\rho(y)dy \ , \end{cases} \tag{57}$$

The variational form is then,

$$A(\phi, v) = (f, v) \ , \quad v \in \mathbb{V}$$

for $f \in L_2(S)$ where

$$\begin{aligned} A(\phi, v) &= \int_S \Delta_s(\phi^3 - \phi)v - \int_S \sigma \Delta_s^2 \phi v + \int_S \frac{d\rho}{d\phi} \Delta_s \psi v \, dx \\ &= -\int_S \nabla_s(\phi^3 - \phi) \cdot \nabla_s v - \sigma \int_S \nabla_s^2 \phi : \nabla_s^2 v \, dx - \int_S \frac{d\rho}{d\phi} \nabla_s \psi \cdot \nabla_s v \, dx \ . \end{aligned} \tag{58}$$

With $\nabla_s^2 w : \nabla_s^2 v = \sum_{i,j=1}^{3} w_{x_i,x_j} v_{x_i,x_j}$ the inner product of the Hessian matrices of w and v.

Let T_h be a regular triangulation of the surface S and define V_h as the standard quadratic finite element space associated with T_h.

$$V_h = \{v \in C(\overline{S}) : v_t = v|_t \in P_2(T)\ \forall T \in T_h\}$$

We first consider the fourth order term (the second term in Equation (58)). We apply integration by parts to the biharmonic operator, Δ_s^2. For $w, v \in H^4(T)$ we will have

(59)

$$\begin{aligned}
\int_S \left(\Delta_s^2 w\right) v\, dx &= \int_{\partial T} \frac{\partial \Delta_s w}{\partial n} v\, ds - \int_T \nabla_s(\Delta_s w) \cdot \nabla_s v\, dx \\
&= \int_{\partial T} \frac{\partial \Delta w}{\partial n} v\, ds - \sum_{i=1}^{2} \int_T (\nabla_s \cdot \nabla_s w_{x_i}) v_{x_i}\, dx \\
&= \int_{\partial T} \frac{\partial \Delta w}{\partial n} v\, ds - \int_{\partial T} (\frac{\partial}{\partial n} \nabla_s w) \cdot \nabla_s v\, ds + \int_T \nabla_s^2 w : \nabla_s^2 v\, dx \\
&= \int_{\partial T} \frac{\partial \Delta w}{\partial n} v\, ds - \int_{\partial T} \frac{\partial^2 w}{\partial n \partial t} \frac{\partial v}{\partial t}\, ds - \int_{\partial T} \frac{\partial^2 w}{\partial n^2} \frac{\partial v}{\partial n}\, ds + \int_T \nabla_s^2 w : \nabla_s^2 v\, dx\ ,
\end{aligned}$$

where $\nabla_s^2 w : \nabla_s^2 v = \sum_{i,j=1}^{3} w_{x_i,x_j} v_{x_i,x_j}$ is the inner product of the Hessian matrices of w and v.

Substituting into Equation (58) the identity in Equation (59) the weak form now becomes

(60)
$$\begin{aligned}
A(\phi, v) = &- \int_T \nabla_s(\phi^3 - \phi) \cdot \nabla_s v - \sigma \int_{\partial T} \frac{\partial \Delta \phi}{\partial n} v\, ds + \sigma \int_{\partial T} \frac{\partial^2 \phi}{\partial n \partial t} \frac{\partial v}{\partial t}\, ds \\
&+ \sigma \int_{\partial T} \frac{\partial^2 \phi}{\partial n^2} \frac{\partial v}{\partial n}\, ds - \sigma \int_T \nabla_s^2 \phi : \nabla_s^2 v\, dx - \int_T \frac{d\rho}{d\phi} \nabla_s \psi \cdot \nabla_s v\, dx\ .
\end{aligned}$$

To define the discrete form of Equation (60), we define the the jumps and averages on edges as follows

$$\begin{aligned}
\left[\!\left[\frac{\partial v}{\partial n_e}\right]\!\right] =& \frac{\partial v_{T_+}}{\partial n_e}|_e - \frac{\partial v_{T_-}}{\partial n_e}|_e \ , \\
\left\langle \frac{\partial v}{\partial n_e} \right\rangle =& \frac{1}{2}\left[\frac{\partial v_{T_+}}{\partial n_e}|_e + \frac{\partial v_{T_-}}{\partial n_e}|_e\right] \ , \\
\left[\!\left[\frac{\partial^2 v}{\partial n_e^2}\right]\!\right] =& \frac{\partial^2 v_{T_+}}{\partial n_e^2}|_e - \frac{\partial^2 v_{T_-}}{\partial n_e^2}|_e \ , \\
\left\langle \frac{\partial^2 v}{\partial n_e^2} \right\rangle =& \frac{1}{2}\left[\frac{\partial^2 v_{T_+}}{\partial n_e^2}|_e + \frac{\partial^2 v_{T_-}}{\partial n_e^2}|_e\right] \ ,
\end{aligned}$$

where e is the edge shared by the two triangles $T_+, T_- \in T_h$. Define n_{T_+},n_{T_-} as the normal direction relative to T_+ and T_- and t_e to be defined as the tangential direction in the counterclockwise direction. This is pictured in Figure 8.1. Then,

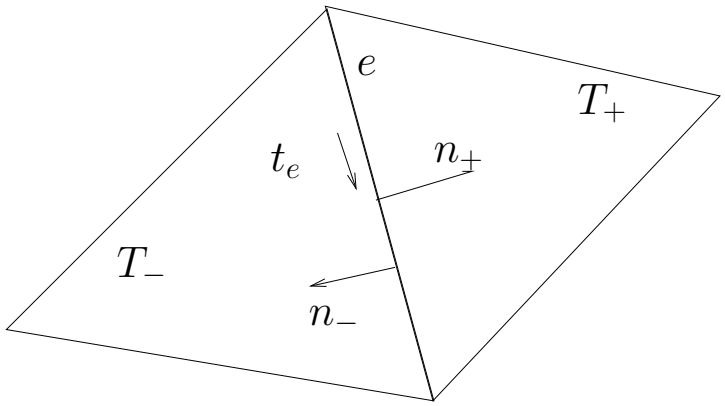

Figure 8.1: An edge, e, shared by triangles T_- and T_+ and the associated normal and tangent vectors

$$\begin{aligned}
\int_S \Delta_s^2 w v =& \sum_j \int_{T_j} \nabla_s^2 w : \nabla_s^2 v \, dx \\
&+ \sum_j \int_{e_j} \left\langle \frac{\partial^2 w}{\partial n_e^2} \right\rangle \left[\!\left[\frac{\partial v}{\partial n_e}\right]\!\right] ds + \sum_j \int_{e_j} \left\langle \frac{\partial^2 v}{\partial n_e^2} \right\rangle \left[\!\left[\frac{\partial w}{\partial n_e}\right]\!\right] ds \\
&+ \sum_j \frac{\epsilon}{|e|} \int_{e_j} \left[\!\left[\frac{\partial w}{\partial n_e}\right]\!\right] \left[\!\left[\frac{\partial v}{\partial n_e}\right]\!\right] ds \ .
\end{aligned}$$

for all $v, w \in V_h$, where $\epsilon \geq 1$ is a penalty parameter. Then the discrete problem is to find $\phi_h \in V_h$ such that

$$A_h(\phi_h, v) = (f, v)$$

for all $v \in V_h$, where

$$\begin{aligned} A_h(\phi_h, v_h) = &- \int_T \nabla(\phi_h^3 - \phi_h) \cdot \nabla v_h - \sigma \int_T \nabla_s^2 \phi_h : \nabla_s^2 v_h \, dx \\ &-\sigma \int_e \left\langle \frac{\partial^2 \phi_h}{\partial n_e^2} \right\rangle \left[\!\left[\frac{\partial v_h}{\partial n_e} \right]\!\right] \, ds - \sigma \int_e \left\langle \frac{\partial^2 v_h}{\partial n_e^2} \right\rangle \left[\!\left[\frac{\partial \phi_h}{\partial n_e} \right]\!\right] \, ds \\ &-\sigma \frac{\epsilon}{|e|} \int_e \left[\!\left[\frac{\partial \phi_h}{\partial n_e} \right]\!\right] \left[\!\left[\frac{\partial v_h}{\partial n_e} \right]\!\right] \, ds - \int_T \frac{d\rho}{d\phi} \nabla \psi_h \cdot \nabla v_h \, dx \end{aligned} \tag{61}$$

and

$$(f, v) = \int_T f v \, dx \ .$$

Since S is a closed surface there are no boundary conditions but is subject to a mass conservation constraint.

$$\int_S \phi \, ds = C$$

where C is the given total quantity of charged lipids on the surface S.

8.1.2. Time Iteration. For the time iteration we use an implicit scheme on the linear parts and explicit scheme on the nonlinear parts. The time dependent problem is

$$\frac{\partial \phi}{\partial t} = \Delta_s \left(f'(\phi) - \sigma \Delta_s \phi + \psi(\phi) \frac{d\rho}{d\phi} \right) \ .$$

For simplification let

$$R = \frac{d\rho}{d\phi} = \frac{q_A - q_B}{2} \ ,$$

then,

$$\frac{\partial \phi}{\partial t} = \Delta_s \left(f'(\phi) - \sigma \Delta_s \phi + \psi(\phi) R \right) \ .$$

To begin, we average the functions over the current and next time step ϕ_n and ϕ_{n+1} and use a linear approximation to the derivative.

$$\left(\frac{\phi^{n+1}-\phi^n}{\Delta t}\right) = \left(\Delta_s f'\left(\frac{\phi^{n+1}+\phi^n}{2}\right) - \sigma\Delta_s^2\left(\frac{\phi^{n+1}+\phi^n}{2}\right) + \frac{R}{2}\Delta_s\psi(\phi^{n+1}+\phi^n)\right) , \tag{62}$$

$$f'(\phi) = \phi^3 - \phi = (\phi^2-1)\phi \ .$$

To treat the fully implicit scheme, we define an interior iteration for computing ϕ_{n+1} with an index k called w^k where $w^k \to \phi^{n+1}$ as $k \to \infty$. Then replacing ϕ_{n+1} with w_k and w_{k+1} we have

$$\left(\frac{w^{k+1}-\phi^n}{\Delta t}\right) + \sigma\Delta_s^2\left(\frac{w^{k+1}}{2}\right) = \Delta_s\left[\left(\frac{w^k+\phi^n}{2}\right)^2 - 1\right]\left(\frac{1}{2}w^k+\phi^n\right) \tag{63}$$

$$- \sigma\Delta_s^2\left(\frac{\phi^n}{2}\right) + \frac{R}{2}\Delta_s\psi(w^k+\phi^n) \ .$$

Thus,

$$w^{k+1} + \sigma\Delta t\Delta_s^2\left(\frac{w^{k+1}}{2}\right) = \frac{\Delta t}{8}\Delta_s\left[(w^k+\phi^n)^2-4\right]\left(w^k+\phi^n\right) \tag{64}$$

$$- \sigma\Delta t\Delta_s^2\left(\frac{\phi^n}{2}\right) + \phi^n + \frac{R\Delta t}{2}\Delta_s\psi(w^k+\phi^n) \ ,$$

where

$$\psi(\phi^n) = \int G(x,y)\rho^n \ dy \qquad \psi(w^k) = \int G(x,y)\rho^k \ dy \ ,$$

and

$$\rho^n = \rho(\phi^n) \ , \qquad \rho^m = \rho(w^m) \ .$$

We continue the inner iteration on k until $||w_{k+1}-w_k|| \leq \beta$, where β is the desired tolerance. Then update $\phi_{n+1} = w_k$ and advance to the next timestep.

8.2. Curvature Model

8.2.1. C^0 Interior Penalty Surface Finite Element Method. Let $S \subset \mathbb{R}^3$ be a bounded polygonal surface and $\mathbb{V} = \{v \in H^2(S) | \frac{\partial v}{\partial n} = 0 \ on \, \partial S\}$, where $\frac{\partial v}{\partial n}$ is the outward

normal derivative. Then the curvature model presented in Chapter 7 reads as:

Find $\phi \in \mathbb{V}$ such that

$$\frac{\partial \phi}{\partial t} = -\frac{\delta F}{\delta \phi} + \frac{1}{|S|}\int_S \frac{\delta F}{\delta \phi} \ , \tag{65}$$

where

$$-\frac{\delta F}{\delta \phi} = -k\epsilon \Delta_s^2 \phi + \frac{2k}{\epsilon}\Delta_s \phi + \left(\frac{2C^2 k}{\epsilon} - \frac{k}{\epsilon^3}\right)\phi + g(\phi) \tag{66}$$

and g is defined by

$$\begin{aligned} g(\phi) = &-\frac{3k}{\epsilon^3}\phi^5 - \frac{5kC}{\epsilon^2}\phi^4 + \left(\frac{4k}{\epsilon^3} - \frac{2C^2 k}{\epsilon}\right)\phi^3 \\ &+ \frac{6Ck}{\epsilon^2}\phi^2 + \frac{k}{\epsilon}\Delta_s \phi^3 + kC\Delta_s \phi^2 + \frac{3k}{\epsilon}\phi^2 \Delta_s \phi + 2Ck\phi\Delta_s \phi - \frac{Ck}{\epsilon^2} \ . \end{aligned} \tag{67}$$

Consider the steady state problem

$$0 = -\frac{\delta F}{\delta \phi} + \frac{1}{|S|}\int_S \frac{\delta F}{\delta \phi} \ . \tag{68}$$

The variational form is then,

$$A(\phi, v) = (f, v) \ , \quad v \in \mathbb{V}$$

for $f \in L_2(S)$ and

(69)

$$\begin{aligned} A(\phi, v) &= \int_S -k\epsilon\Delta_s^2 \phi v + \int_S \frac{2k}{\epsilon}\Delta_s \phi v + \int_S \left(\frac{2C^2 k}{\epsilon} - \frac{k}{\epsilon^3}\right)\phi v + \int_S g(\phi)v + \int_S \frac{1}{|S|}\int_S \frac{\delta F}{\delta \phi} v \\ &= -k\epsilon \int_S \nabla_s^2 \phi : \nabla_s^2 v \, dx - \int_S \left(\sigma - \frac{2k}{\epsilon}\right)\nabla_s \phi \cdot \nabla_s v + \int_S \left(1 + \frac{2C^2 k}{\epsilon} - \frac{k}{\epsilon^3}\right)\phi v \\ &+ \int_S g(\phi)v + \int_S \frac{1}{|S|}\int_S \frac{\delta F}{\delta \phi} v \ , \end{aligned}$$

and $\nabla_s^2 w : \nabla_s^2 v = \sum_{i,j=1}^3 w_{x_i,x_j} v_{x_i,x_j}$ is the inner product of the Hessian matrices of w and v.

Let T_h be a regular triangulation of the surface S and define V_h as the standard quadratic finite element space associated with T_h;

$$V_h = \{v \in C(\overline{S}) : v_t = v|_t \in P_2(T)\ \forall T \in T_h\}\ .$$

Consider the fourth order term (the first term in Equation (69)). We apply integration by parts to the biharmonic operator Δ_s^2. For $w, v \in H^4(T)$ we have

$$\begin{aligned}
(70)\quad \int_S \left(\Delta^2 w\right) v\, dx &= \int_{\partial T} \frac{\partial \Delta_s w}{\partial n} v\, ds - \int_T \nabla_s(\Delta_s w)\cdot\nabla_s v\, dx \\
&= \int_{\partial T} \frac{\partial \Delta w}{\partial n} v\, ds - \sum_{i=1}^{2}\int_T (\nabla_s\cdot\nabla_s w_{x_i}) v_{x_i}\, dx \\
&= \int_{\partial T} \frac{\partial \Delta w}{\partial n} v\, ds - \int_{\partial T} (\frac{\partial}{\partial n}\nabla_s w)\cdot\nabla_s v\, ds + \int_T \nabla_s^2 w : \nabla_s^2 v\, dx \\
&= \int_{\partial T} \frac{\partial \Delta w}{\partial n} v\, ds - \int_{\partial T} \frac{\partial^2 w}{\partial n \partial t}\frac{\partial v}{\partial t}\, ds - \int_{\partial T} \frac{\partial^2 w}{\partial n^2}\frac{\partial v}{\partial n}\, ds + \int_T \nabla_s^2 w : \nabla_s^2 v\, dx
\end{aligned}$$

where $\nabla_s^2 w : \nabla_s^2 v = \sum_{i,j=1}^{3} w_{x_i,x_j} v_{x_i,x_j}$ is the inner product of the Hessian matrices of w and v.

Substituting into Equation (69) the identity in Equation (70) the weak form now becomes

$$\begin{aligned}
(71)\quad A(\phi, v) = &-\int_T \frac{2k}{\epsilon}\nabla_s\phi\cdot\nabla_s v + \int_T \left(\frac{2C^2 k}{\epsilon} - \frac{k}{\epsilon^3}\right)\phi v \\
&+ \int_T g(\phi) v + \int_T \frac{1}{|S|}\int_S \frac{\delta F}{\delta \phi} v - k\epsilon \int_T \nabla_s^2\phi : \nabla_s^2 v\, dx \\
&- \int_{\partial T} \frac{\partial \Delta_s \phi}{\partial n} v\, ds + \int_{\partial T} \frac{\partial^2 \phi}{\partial n \partial t}\frac{\partial v}{\partial t}\, ds \\
&+ \int_{\partial T} \frac{\partial^2 \phi}{\partial n^2}\frac{\partial v}{\partial n}\, ds
\end{aligned}$$

To define the discrete form of equation (71), we define the the jumps and averages as follows

$$\begin{aligned}
\left[\!\left[\frac{\partial v}{\partial n_e}\right]\!\right] =& \frac{\partial v_{T_+}}{\partial n_e}|_e - \frac{\partial v_{T_-}}{\partial n_e}|_e \ , \\
\left\langle \frac{\partial v}{\partial n_e} \right\rangle =& \frac{1}{2}\left[\frac{\partial v_{T_+}}{\partial n_e}|_e + \frac{\partial v_{T_-}}{\partial n_e}|_e\right] \ , \\
\left[\!\left[\frac{\partial^2 v}{\partial n_e^2}\right]\!\right] =& \frac{\partial^2 v_{T_+}}{\partial n_e^2}|_e - \frac{\partial^2 v_{T_-}}{\partial n_e^2}|_e \ , \\
\left\langle \frac{\partial^2 v}{\partial n_e^2} \right\rangle =& \frac{1}{2}\left[\frac{\partial^2 v_{T_+}}{\partial n_e^2}|_e + \frac{\partial^2 v_{T_-}}{\partial n_e^2}|_e\right] \ ,
\end{aligned}$$

where e is the edge shared by the two triangles $T_+, T_- \in T_h$. Define n_{T_+},n_{T_-} as the normal direction relative to T_+ and T_- and t_e to be defined as the tangential direction in the counterclockwise direction. This can be seen in Figure 8.1. Then,

$$\begin{aligned}
\int_S \Delta_s^2 w v =& \sum_j \int_{T_j} \nabla^2 w : \nabla^2 v \, dx \\
&+ \sum_j \int_{e_j} \left\langle \frac{\partial^2 w}{\partial n_e^2} \right\rangle \left[\!\left[\frac{\partial v}{\partial n_e}\right]\!\right] ds + \sum_j \int_{e_j} \left\langle \frac{\partial^2 v}{\partial n_e^2} \right\rangle \left[\!\left[\frac{\partial w}{\partial n_e}\right]\!\right] ds \\
&+ \sum_j \frac{\mu}{|e|} \int_{e_j} \left[\!\left[\frac{\partial w}{\partial n_e}\right]\!\right] \left[\!\left[\frac{\partial v}{\partial n_e}\right]\!\right] ds \ ,
\end{aligned}$$

for all $v, w \in V_h$, where $\mu \geq 1$ is a penalty paramenter. Then the discrete problem is to find $\phi_h \in V_h$ such that

$$A_h(\phi_h, v) = (f, v)$$

for all $v \in V_h$, where

$$\begin{aligned}
A_h(\phi_h, v_h) =& -\int_T \frac{2k}{\epsilon} \nabla_s \phi_h \cdot \nabla_s v_h + \int_T \left(\frac{2C^2 k}{\epsilon} - \frac{k}{\epsilon^3}\right) \phi_h v_h \\
&+ \int_T g(\phi_h) v_h + \int_T \frac{1}{|S|} \int_S \frac{\delta F}{\delta \phi} v_h - k\epsilon \int_T \nabla^2 \phi_h : \nabla^2 v_h \, dx \\
&- \int_e \left\langle \frac{\partial^2 \phi_h}{\partial n_e^2} \right\rangle \left[\!\left[\frac{\partial v_h}{\partial n_e}\right]\!\right] ds - \int_e \left\langle \frac{\partial^2 v_h}{\partial n_e^2} \right\rangle \left[\!\left[\frac{\partial \phi_h}{\partial n_e}\right]\!\right] ds \\
&- \frac{\mu}{|e|} \int_e \left[\!\left[\frac{\partial \phi_h}{\partial n_e}\right]\!\right] \left[\!\left[\frac{\partial v_h}{\partial n_e}\right]\!\right] ds
\end{aligned} \tag{72}$$

and

$$(f, v) = \int_T f v \, dx$$

We will now develop an iteration method to solve the time-dependent problem.

8.2.2. Time Iteration. The solution technique is similar to the solution technique for the electrostatic model in Section 8.1.2. We use an implicit scheme on the linear parts and explicit scheme on the nonlinear parts. For the curvature model the time dependent problem is

$$\phi_t = -\gamma \frac{\delta F}{\delta \phi} + \frac{1}{|S|} \int_S \frac{\delta F}{\delta \phi} \ . \tag{73}$$

For simplification define $g = \frac{\delta F}{\delta \phi}$ and $\lambda = \frac{1}{|S|} \int_S \frac{\delta F}{\delta \phi}$. Then the equation for gradient flow is given by

$$\phi_t = -\gamma g + \lambda. \tag{74}$$

To begin, we average the function in the first equation over the current and next step ϕ_n and ϕ_{n+1}, and use a linear approximation on the derivative to obtain,

$$\frac{\phi_{n+1} - \phi_n}{\Delta t} + \gamma g(\phi_{n+1}, \phi_n) - \lambda = 0, \tag{75}$$

where the averaged function is defined by

$$\begin{aligned} g(\phi_{n+1}, \phi_n) = & \frac{k}{2} \Delta \left(f_c(\phi_{n+1}) + f_c(\phi_n) \right) \\ & - \frac{k}{2\epsilon^2} \left(\phi_{n+1}^2 + \phi_{n+1}\phi_n + \phi_n^2 + C\epsilon(\phi_{n+1} + \phi_n) - 1 \right) \left(f_c(\phi_{n+1}) + f_c(\phi_n) \right) \ , \end{aligned} \tag{76}$$

and

$$f_c(\phi) = k \left(\epsilon \Delta \phi - \frac{1}{\epsilon} \left(\phi + C\epsilon \right) \left(\phi^2 - 1 \right) \right) \ . \tag{77}$$

To numerically treat this implicit scheme, we define an interior iteration for computing ϕ_{n+1} with an index m, named ψ_m, where $\psi_m \to \phi_{n+1}$ as $m \to \infty$. Then, replacing ϕ_{n+1} with ψ_m

and ψ_{m+1} in (75), we have:

$$\frac{\psi_{m+1}-\phi_n}{\Delta t}+\gamma g(\psi_{m+1},\psi_m,\phi_n)-\lambda=0, \tag{78}$$

where the new averaged functions are defined by

$$f_c'(\psi_{m+1},\psi_m,\phi_n)=\frac{\epsilon}{2}\Delta(\psi_{m+1}+\phi_n)-\frac{1}{4\epsilon}(\psi_m^2+\phi_n^2-2)(\psi_m+\phi_n+2C\epsilon) \tag{79}$$

$$\begin{aligned} g(\psi_{m+1},\psi_m,\phi_n)&=k\Delta\left(f_c'(\psi_{m+1},\psi_m,\phi_n)\right)\\ &\quad-\frac{k}{2\epsilon^2}\left(\psi_m^2+\psi_m\phi_n+\phi_n^2-1+C\epsilon(\psi_m+\phi_n)\right)\left(f_c(\psi_m)+f_c(\phi_n)\right)\,. \end{aligned} \tag{80}$$

We first iterate over the interior index m. Numerically, once $||\psi_{m+1}-\psi_m||\leq\beta$ where β is the desired tolerance, we say that ψ_m has converged and update $\phi_{n+1}=\psi_m$. Then, we advance to the next timestep.

To efficiently solve Equation (78) we divide the averaged functions up into linear and nonlinear parts, where the linear parts are functions of ψ_{m+1} only and the nonlinear parts are functions of ϕ_n and ψ_m only.

$$f_{c_{lin}}'(\psi_{m+1})=\frac{\epsilon}{2}\Delta\psi_{m+1}\ , \tag{81}$$

$$f_{c_{nlin}}'(\psi_m,\phi_n)=\frac{\epsilon}{2}\Delta\phi_n-\frac{1}{4\epsilon}(\psi_m^2+\phi_n^2-2)(\psi_m+\phi_n+2C\epsilon)\ , \tag{82}$$

$$g_{lin}=k\Delta f_{c_{lin}}'(\psi_{m+1})\ , \tag{83}$$

$$\begin{aligned} g_{nlin}&=k\Delta f_{c_{nlin}}'(\psi_m,\phi_n)\\ &\quad-\frac{k}{2\epsilon^2}\left(\psi_m^2+\psi_m\phi_n+\phi_n^2-1+C\epsilon(\psi_m+\phi_n)\right)\left(f_c(\psi_m)+f_c(\phi_n)\right)\,. \end{aligned} \tag{84}$$

The implicit scheme is now given by

$$\frac{\psi_{m+1}-\phi_n}{\Delta t}=\lambda-\gamma\left(g_{lin}+g_{nlin}\right). \tag{85}$$

To solve Equation (85), we first gather all the terms ψ_{m+1}, using the formulas for f_{lin} and g_{lin}:

$$\psi_{m+1} + \gamma \Delta t g_{lin} = (\lambda - \gamma g_{nlin})\,\Delta t + \phi_n, \tag{86}$$

$$\left(1 + \frac{\gamma \Delta t k \epsilon}{2} \Delta^2\right) \psi_{m+1} = (\lambda - \gamma g_{nlin})\,\Delta t + \phi_n.$$

Expanding the right hand side of Equation (86) we have

$$(\lambda - \gamma g_{nlin})\Delta t + \phi_n = \Delta t \lambda_1 - \frac{\Delta t \gamma k \epsilon}{2} \Delta^2 \phi_n + \Delta t \gamma \Delta \left(\frac{k}{4\epsilon} (\psi_m^2 + \phi_n^2 - 2)(\psi_m + \phi_n + 2C\epsilon) \right)$$
$$+ \Delta t \gamma \left(\frac{k}{2\epsilon^2} \left(\psi_m^2 + \psi_m \psi_n + \phi_n^2 - 1 + C\epsilon(\psi_m + \phi_n) \right) \left(f_c(\psi_m) + f_c(\phi_n) \right) \right) + \phi_n \ ,$$

where

$$f_c(\psi_m) = \epsilon \Delta \psi_m - \frac{1}{\epsilon} (\psi_m^2 - 1)(\psi_m + C\epsilon) \ ,$$

and

$$f_c(\phi_n) = \epsilon \Delta \phi_n - \frac{1}{\epsilon} (\phi_n^2 - 1)(\phi_n + C\epsilon) \ .$$

8.3. Surface Finite Elements

First we approximate the surface, S, by a polyhedral surface, S_h, which is the union of triangular faces, as seen in Figure 8.2.

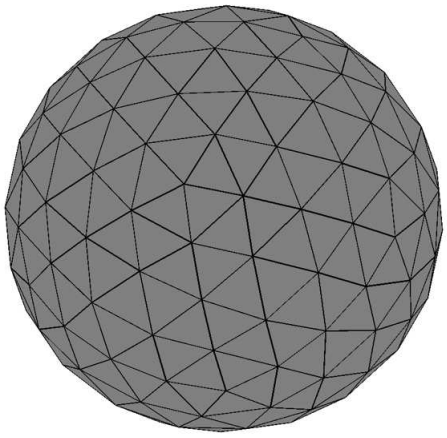

Figure 8.2: Sphere with triangle mesh

Let T_j be the j^{th} triangular face. Then,

$$S \approx S_h = \bigcup_{j=1}^{N} T_j \tag{87}$$

where N is the number of triangles. Every triangle is made up of three nodes and three midpoints. So each T_j, called a physical element, is associated with six points p_k, where $1 \geq k \leq 6$ as seen in Figure 8.3.

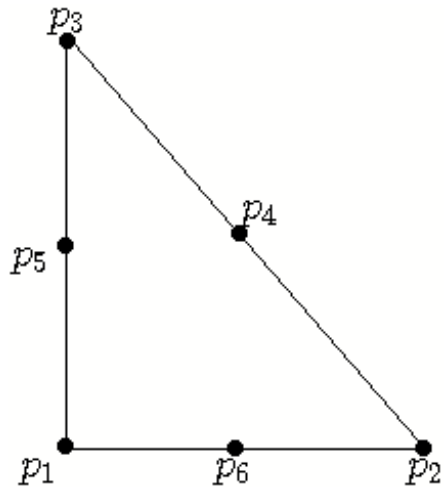

Figure 8.3: Triangle with six nodes. Three are the vertices of the triangle. The other three are the centers of three edges.

Consider one particular triangle, known as the reference element. The reference element refers to the triangle with vertices at

$$p_1 = (0,0,0),\ p_2 = (1,0,0),\ p_3 = (0,1,0),\ p_6 = \left(\frac{1}{2},0,0\right),\ p_4 = \left(\frac{1}{2},\frac{1}{2},0\right),\ p_5 = \left(0,\frac{1}{2},0\right).$$

This is pictured in Figure 8.4. To distinguish between reference element coordinates and physical element coordinates, we will denote the reference element with coordinates (ξ, η, ζ) and physical elements with coordinates (x, y, z). Also note the cooresponding node indicies will be labled in a counterclockwise order. Since the reference triangle lies locally in the

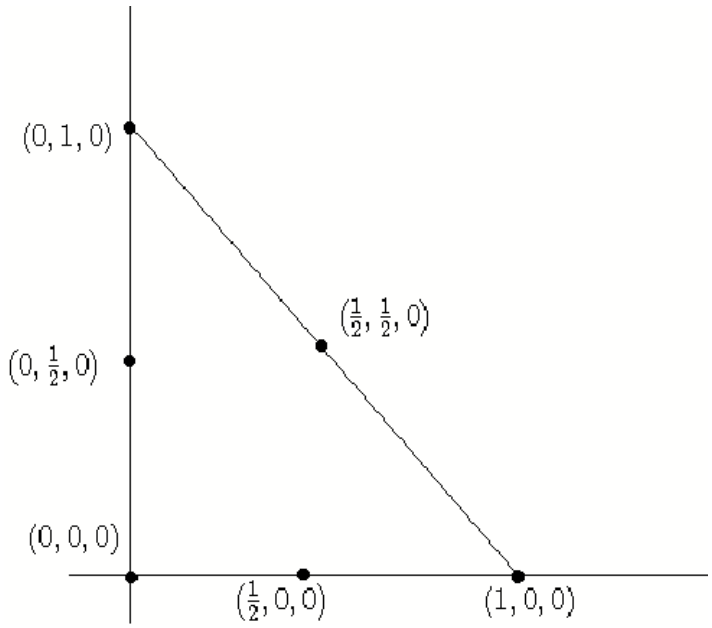

Figure 8.4: Reference triangle

$xy - plane$ we can treat it in two dimensions. Define

$$V_h = \{v \in C(\overline{S}) : v_t = v|_t \in P_2(T) \ \forall T \in T_h\}$$

and let $\{v_1, v_2, ..., v_n\}$ be the standard quadratic Lagrange basis functions of the form

$$v_i(x, y) = c_0 + c_1 x + c_2 y + c_3 x^2 + c_4 xy + c_5 y^2 \tag{88}$$

with general surface gradients

$$\nabla_s v_i(x, y) = \begin{bmatrix} c_1 + 2c_3 x + c_4 y \\ c_2 + 2c_5 y + c_4 x \\ 0 \end{bmatrix},$$

and the associated general surface Hessian matrix

$$H_f = \begin{bmatrix} 2c_3 & c_4 \\ c_4 & 2c_5 \end{bmatrix}.$$

Then for any $u \in V_h$

$$u(p) = \sum_{i}^{N} \bar{u}_i v_i(p) \ , \tag{89}$$

where $p \in S$. The basis functions defined on the reference element are

$$\mathbf{v_1} = 1 - 3\xi - 3\eta + 2\xi^2 + 4\eta\xi + 2\eta^2, \ \ \mathbf{v_2} = -\xi + 2\xi^2, \ \ \mathbf{v_3} = -\eta + 2\eta^2,$$

$$\mathbf{v_4} = 4\xi - 4\eta\xi - 4\xi^2, \ \ \mathbf{v_5} = 4\eta\xi, \ \ \mathbf{v_6} = 4\eta - 4\eta\xi - 4\eta^2,$$

We can map every physical triangle to the reference triangle, depicted in Figure 8.5, by the following affine transformation, denoted as $F(\xi, \eta, \zeta)$.

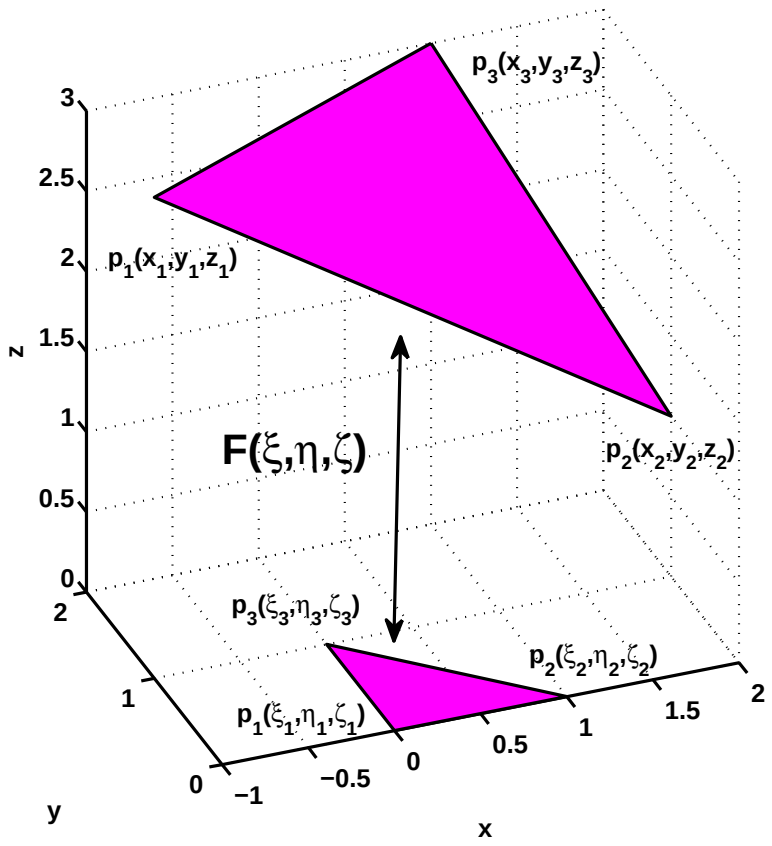

Figure 8.5: Affine transformation where $\zeta_1 = \zeta_2 = \zeta_3 = 0$

$$\underbrace{\begin{bmatrix} x \\ y \\ z \end{bmatrix} = \underbrace{\begin{bmatrix} x_2 - x_1 & x_3 - x_1 & n_1 \\ y_2 - y_1 & y_3 - y_1 & n_2 \\ z_2 - z_1 & z_3 - z_1 & n_3 \end{bmatrix}}_{\mathrm{M}} \begin{bmatrix} \xi \\ \eta \\ \zeta \end{bmatrix} + \begin{bmatrix} x_1 \\ y_1 \\ z_1 \end{bmatrix}}_{\mathrm{F}(\xi,\eta,\zeta)} \tag{90}$$

where n_k are the entries of the normal vector to the triangle T_j and (x_1, y_1, z_1) are the coordinates of the first node on the physical triangle. Now we are able evaluate the basis functions on every physical element, v_i, using the basis functions defined on the reference element in Equation (90). For example the gradient vector on a physical element would be calculated as follows

$$\nabla u = \begin{bmatrix} \frac{\partial u}{\partial x} \\ \frac{\partial u}{\partial y} \\ \frac{\partial u}{\partial z} \end{bmatrix} \tag{91}$$

with entries

$$\frac{\partial u}{\partial x} = \begin{bmatrix} \frac{\partial \xi}{\partial x} & \frac{\partial \eta}{\partial x} \end{bmatrix} \cdot \begin{bmatrix} \frac{\partial u}{\partial \xi} \\ \frac{\partial u}{\partial \eta} \end{bmatrix}, \tag{92}$$

$$\frac{\partial u}{\partial y} = \begin{bmatrix} \frac{\partial \xi}{\partial y} & \frac{\partial \eta}{\partial y} \end{bmatrix} \cdot \begin{bmatrix} \frac{\partial u}{\partial \xi} \\ \frac{\partial u}{\partial \eta} \end{bmatrix}, \tag{93}$$

$$\frac{\partial u}{\partial z} = \begin{bmatrix} \frac{\partial \xi}{\partial z} & \frac{\partial \eta}{\partial z} \end{bmatrix} \cdot \begin{bmatrix} \frac{\partial u}{\partial \xi} \\ \frac{\partial u}{\partial \eta} \end{bmatrix}, \tag{94}$$

and the Hessian matrix would be calculated as

$$H_f = \begin{bmatrix} \frac{\partial^2 u}{\partial x^2} & \frac{\partial^2 u}{\partial x \partial y} & \frac{\partial^2 u}{\partial x \partial z} \\ \frac{\partial^2 u}{\partial y \partial x} & \frac{\partial^2 u}{\partial y^2} & \frac{\partial^2 u}{\partial y \partial z} \\ \frac{\partial^2 u}{\partial z \partial x} & \frac{\partial^2 u}{\partial z \partial y} & \frac{\partial^2 u}{\partial z^2} \end{bmatrix} , \tag{95}$$

with entries

$$\frac{\partial^2 u}{\partial x^2} = \begin{bmatrix} \left(\frac{\partial \xi}{\partial x}\right)^2 & \frac{\partial \xi}{\partial x}\frac{\partial \eta}{\partial x} \\ \frac{\partial \eta}{\partial x}\frac{\partial \xi}{\partial x} & \left(\frac{\partial \eta}{\partial x}\right)^2 \end{bmatrix} \begin{bmatrix} \frac{\partial^2 u}{\partial \xi^2} & \frac{\partial^2 u}{\partial \xi \partial \eta} \\ \frac{\partial^2 u}{\partial \eta \partial \xi} & \frac{\partial^2 u}{\partial \eta^2} \end{bmatrix} = \begin{bmatrix} \left(\frac{\partial \xi}{\partial x}\right)^2 & \frac{\partial \xi}{\partial x}\frac{\partial \eta}{\partial x} \\ \frac{\partial \eta}{\partial x}\frac{\partial \xi}{\partial x} & \left(\frac{\partial \eta}{\partial x}\right)^2 \end{bmatrix} \begin{bmatrix} 2c_3 & c_4 \\ c_4 & 2c_5 \end{bmatrix} . \tag{96}$$

To calculate the normal derivatives on the triangle edges as seen in equation (72) and (61) we will develop a normal transformation defined as

$$\begin{bmatrix} n \\ \tau \\ \nu \end{bmatrix} = \underbrace{\begin{bmatrix} n_x & n_y & n_z \\ \tau_x & \tau_y & \tau_z \\ \nu_x & \nu_y & \nu_z \end{bmatrix}}_{\mathrm{M}} \begin{bmatrix} x \\ y \\ z \end{bmatrix} \tag{97}$$

Where n_x,n_y,n_z are the components to the vector normal to the triangle edge, $\mathbf{n}$. t_x,t_y,t_z are the components to the vector tangent to the triangle edge, τ. ν_x,ν_y,ν_z are the components to the vector normal to the triangle face, ν. These are pictured in Figure 8.6.

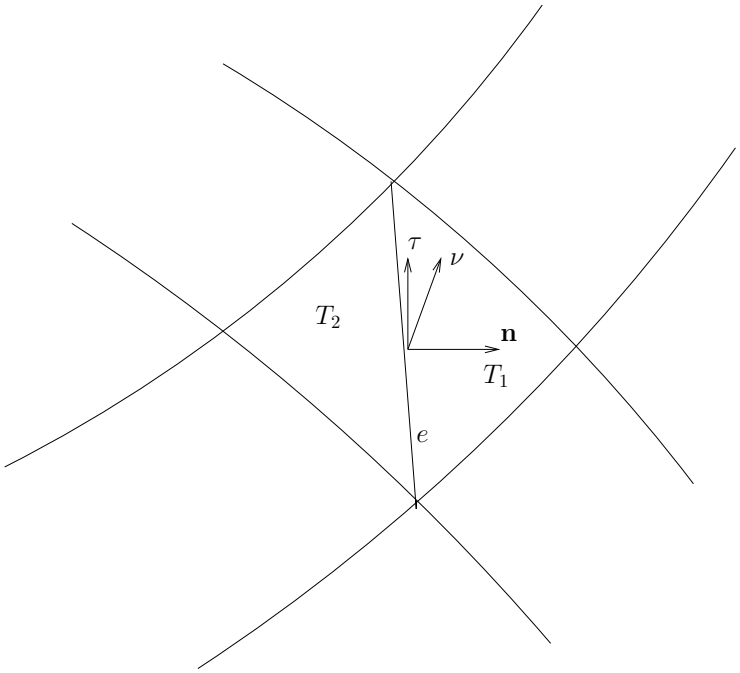

Figure 8.6: Local coordinate system on a triangulated surface

This transformation allows us to calculate the normal derivatives on the triangle edge. For example the first and second derivatives would be calculated as

$$\frac{\partial^2 u}{\partial n^2} = \begin{bmatrix} \left(\frac{\partial x}{\partial n}\right)^2 & \frac{\partial x}{\partial n}\frac{\partial y}{\partial n} & \frac{\partial x}{\partial n}\frac{\partial z}{\partial n} \\ \frac{\partial y}{\partial n}\frac{\partial x}{\partial n} & \left(\frac{\partial y}{\partial n}\right)^2 & \frac{\partial y}{\partial n}\frac{\partial z}{\partial n} \\ \frac{\partial x}{\partial n}\frac{\partial z}{\partial n} & \frac{\partial y}{\partial n}\frac{\partial z}{\partial n} & \left(\frac{\partial z}{\partial n}\right)^2 \end{bmatrix} \begin{bmatrix} \frac{\partial^2 u}{\partial x^2} & \frac{\partial^2 u}{\partial x \partial y} & \frac{\partial^2 u}{\partial x \partial z} \\ \frac{\partial^2 u}{\partial y \partial x} & \frac{\partial^2 u}{\partial y^2} & \frac{\partial^2 u}{\partial y \partial z} \\ \frac{\partial^2 u}{\partial z \partial x} & \frac{\partial^2 u}{\partial z \partial y} & \frac{\partial^2 u}{\partial z^2} \end{bmatrix}, \tag{98}$$

$$\frac{\partial u}{\partial n} = \begin{bmatrix} \frac{\partial u}{\partial x} \\ \frac{\partial u}{\partial y} \\ \frac{\partial u}{\partial z} \end{bmatrix} \cdot \begin{bmatrix} n_x \\ n_y \\ n_z \end{bmatrix}. \tag{99}$$

Using both transformations presented above and the $\mathbb{P}_2$ finite element space we are able to solve the discrete problem defined by Equations (72) and (61).

CHAPTER 9

Numerical Simulations and Discussion

9.1. Numerical Solution of the Cahn-Hilliard Equation on Surfaces

In this section we numerically implement the Cahn-Hilliard equations presented in Chapter 2. The coding of the model was done in C, using a biconjugate gradiant method and a 6-point Gaussian Quadrature. We apply the C^0 interior penalty surface finite element method and the implicit time iteration scheme discussed in Chapter 8. We first vary the penalty parameter, μ, to find the most precise solution. Then we modify the interface width, σ, to find the desired separation. We also compare and contrast the total energy using different σ. These graphs are used for comparision in later simulations.

After 10,000 iterations the results for different penalty parameters, μ, with σ fixed at $\sigma = 0.1$ are found in Figure 9.1. These were ran on a mesh with 460 nodes until the time evolution reached equillibrium state. These results show that the penalty parameter does not effect the solutions greatly. After 10,000 iterations the results for different σ with μ fixed at $\mu = 10.0$ are found in Figure 9.2. These were ran on a mesh with 460 nodes until the time evolution reached equillibrium state. After 10,000 iterations the energy plots for these different σ values are found in Figure 9.3. Note that in this graph the red curve for $\sigma = 0.001$ is very similiar to $\sigma = 0.0001$ and is not visible on this graph.

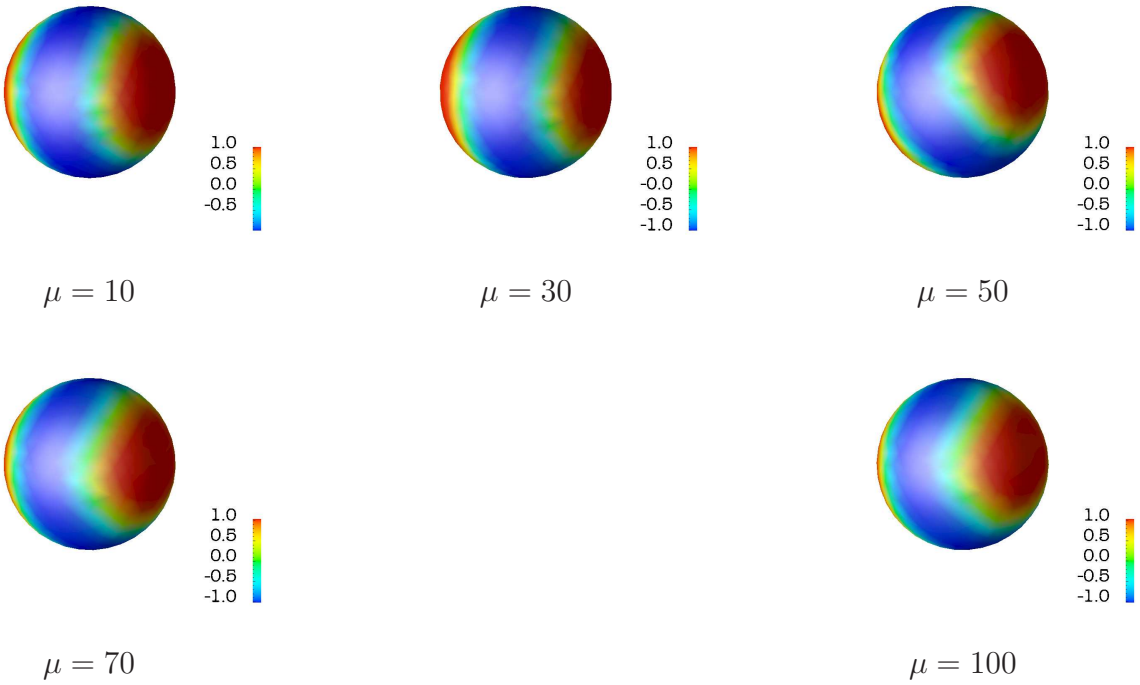

Figure 9.1: Cahn-Hilliard solutions for different values of the penalty parameter, μ

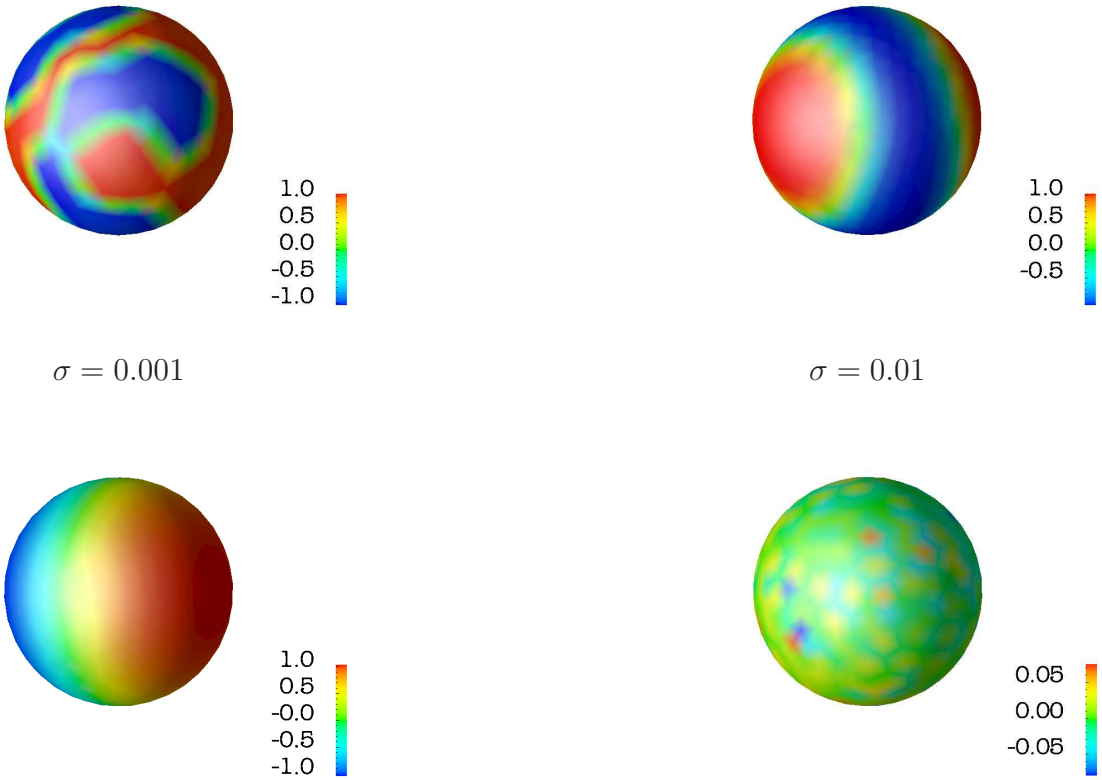

$\sigma = 0.001$ $\sigma = 0.01$

$\sigma = 0.1$ $\sigma = 1.0$

Figure 9.2: Cahn-Hilliard solutions for different interface widths, σ

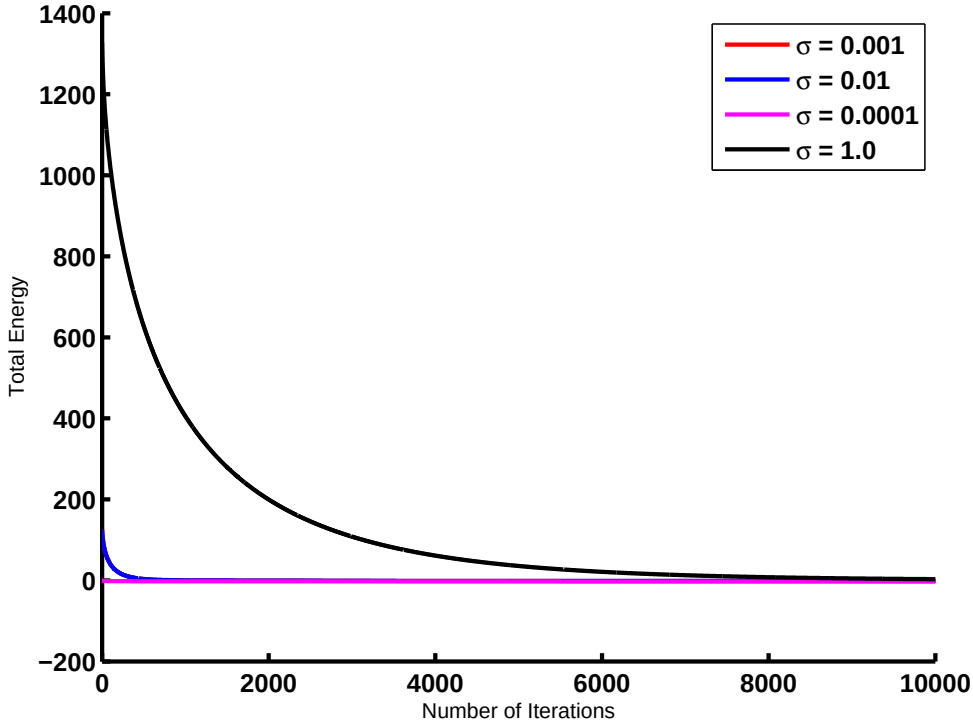

Figure 9.3: Total energy for different σ values

In Figure 9.4 we present the obtained results ran on a fine mesh with 3963 nodes for 10,000 iterations.

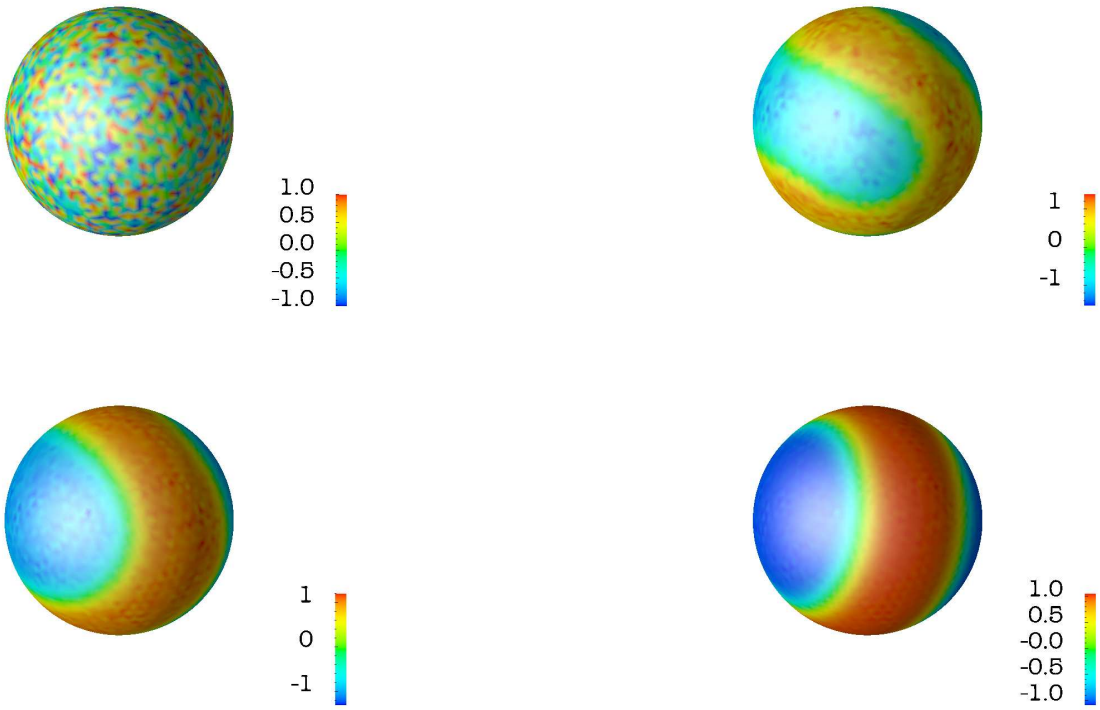

Figure 9.4: Plot of solutions of the Cahn-Hilliard equation with penalty parameter $\mu = 10$, interface width $\sigma = 0.01$, timestep $\Delta t = 0.001$. Top left is the initial condition. Top right is at 2000 iterations. Bottom left is at 4000 iterations. Bottom right is at 8000 iterations

We can see separation into two domains one with $\phi = 1$ and one with $\phi = -1$ in the numerical results. These are the expected results and gives confindence to implement the modified models presented in Chapter 5 and 6.

9.2. Electrostatic Simulations

In this section we numerically implement the electrostatic lipid raft model presented in Chapter 5. The coding of the model was done in C using a biconjugate gradient method and a 6-point Gaussian Quadrature. We apply the C^0 interior penalty surface finite element method and the time iteration scheme discussed in Chapter 8. We present solutions using different interface widths, σ. We also compare and contrast the total energy.

After 10,000 iterations the results for different interface widths, σ, with the penalty parameter, μ, fixed at $\mu = 10.0$ are found in Figure 9.5. These were ran on a mesh with 460 nodes with a random initial condition until an equillibrium state is reached.

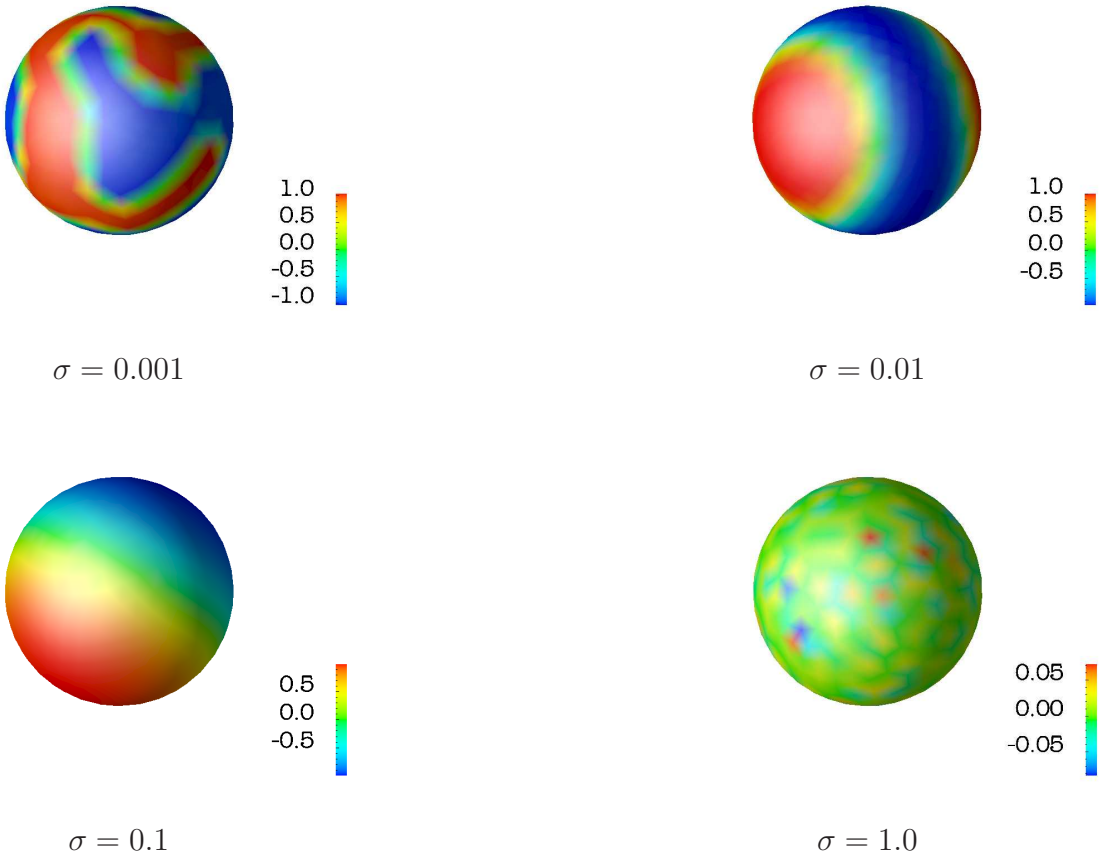

$\sigma = 0.001$ $\sigma = 0.01$

$\sigma = 0.1$ $\sigma = 1.0$

Figure 9.5: Electrostatic model solutions for different σ values

After 10,000 iterations the energy plots for these different σ values are found in Figure 9.6

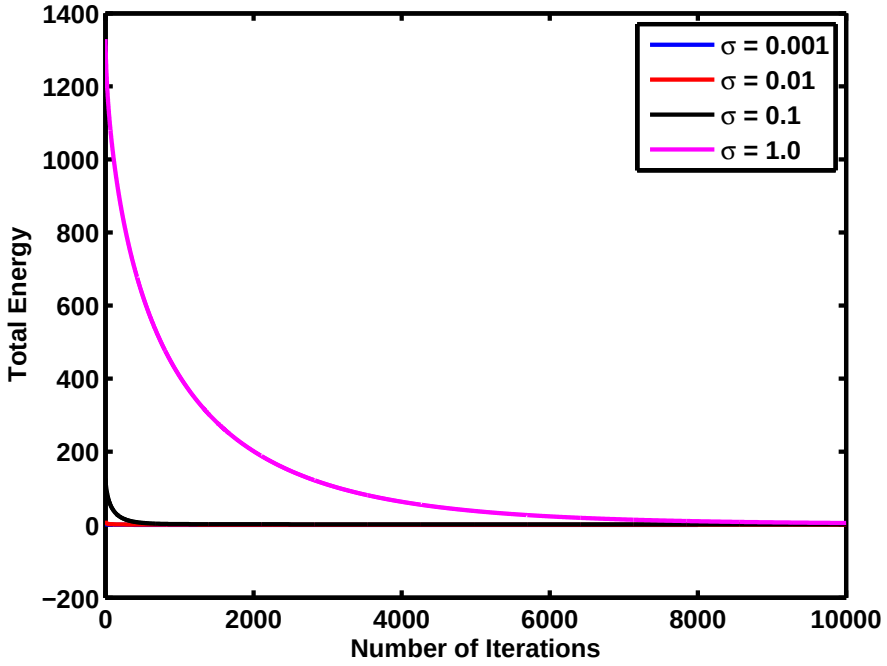

Figure 9.6: Electrostic model total energy for different interface widths, σ

As one would notice the solutions above are very similar to the Cahn-Hilliard equations. This leads us to scale the electrostatic energy by some constant, ϵ, to make this energy relevent in the solution. Three different patterns were obtained as seen in Figures 9.7, 9.8, and 9.9. We were unable to obtain circular raft-like mircodomains at this time. However, the model is very sensitive to the value of ϵ and further investigation into this model is necessary. The total energy for these three simulations and for different values of ϵ can be found in Figure 9.10. Note that for $\epsilon = 0$ the standard Cahn-Hilliard energy is reproduced.

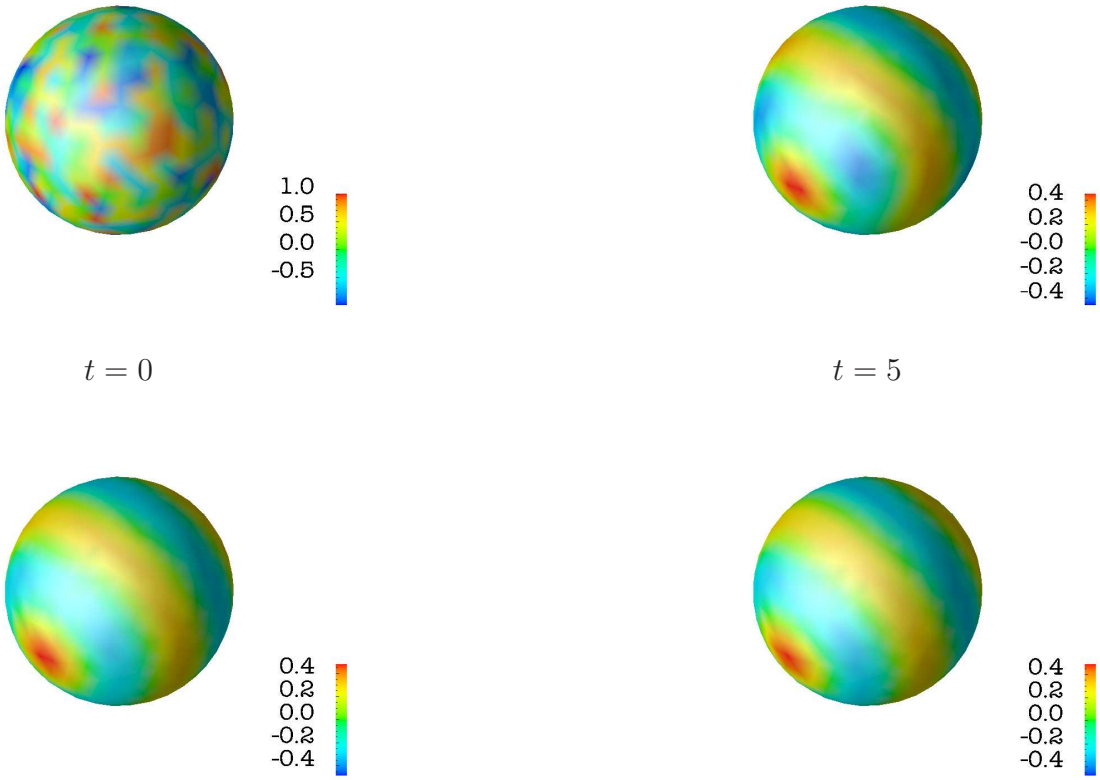

Figure 9.7: Electrostatic model solutions for scaling constant $\epsilon = 5.0$.

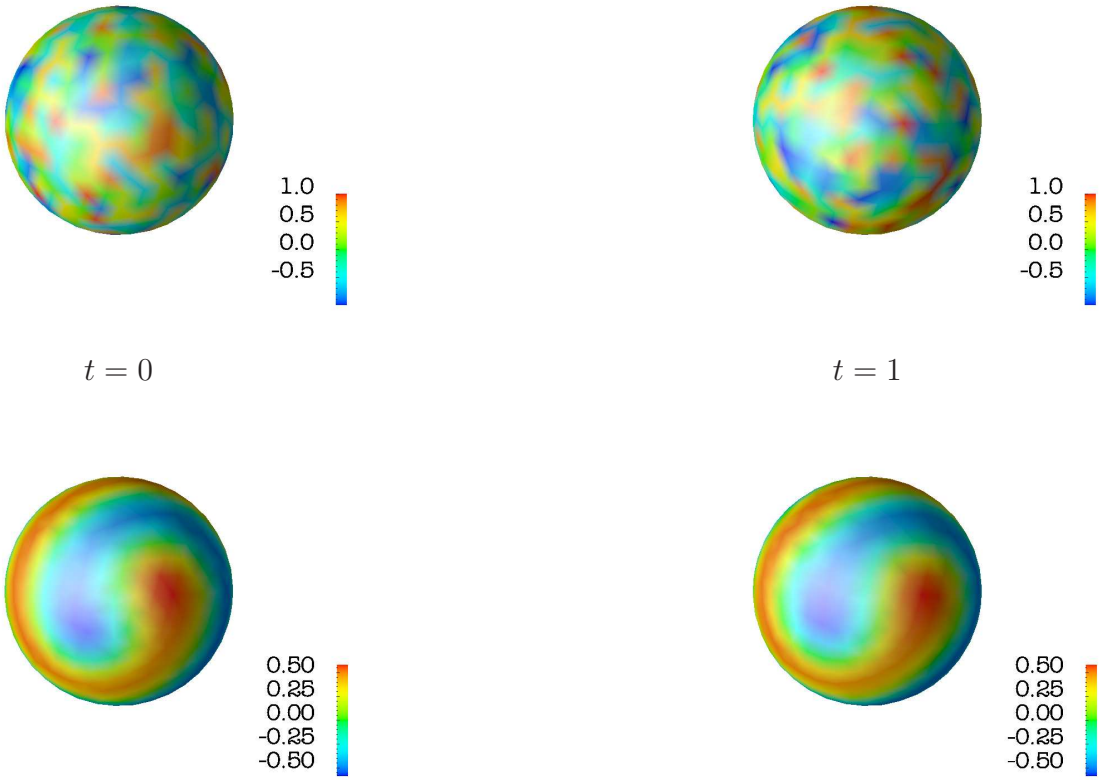

Figure 9.8: Electrostatic model solutions for scaling constant $\epsilon = 4.5$.

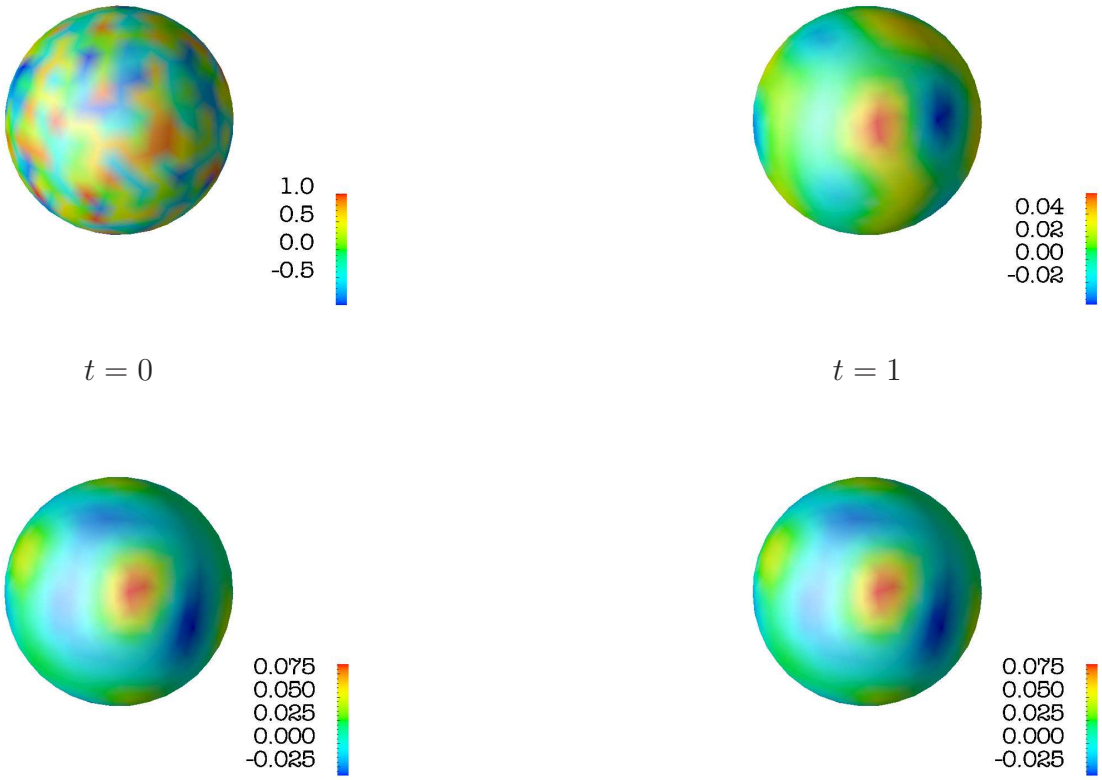

$t = 0$ $t = 1$

$t = 10$ $t = 20$

Figure 9.9: Electrostatic model solutions for scaling constant $\epsilon = 5.5$.

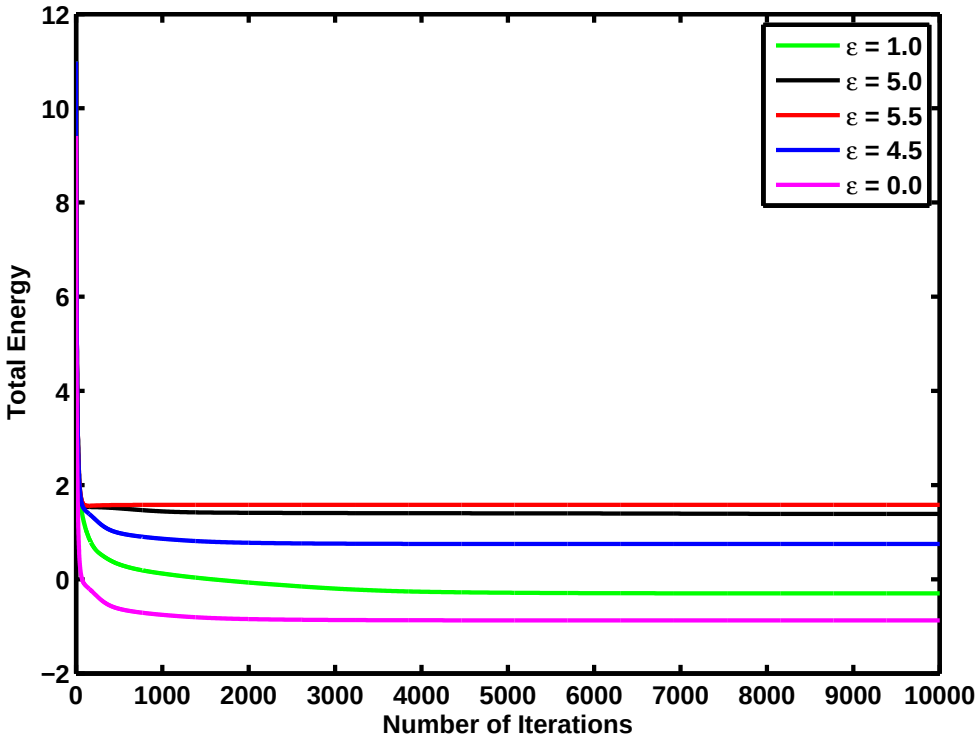

Figure 9.10: Electrostic Energy for different scaling constants,ϵ.

9.3. Numerical Simulations of the Allen-Cahn equation

In this section we numerically solve the Allen-Cahn equation presented in Chapter 2. The coding of the model was done in C, using a biconjugate gradient method and a 6-point Gaussian Quadrature. We apply the C^0 interior penalty surface finite element method and the time iteration scheme discussed in Chapter 8. We present solutions using different values for the parameters σ, as well as different initial conditions as the model may be sesitive to the inital state. We also compare and contrast the total energy.

After 10,000 iterations the results for different σ with μ fixed at $\mu = 10.0$ are found in Figure 9.11, 9.12, 9.13, and 9.14. These were ran on a mesh with 460 nodes until equillibrium.

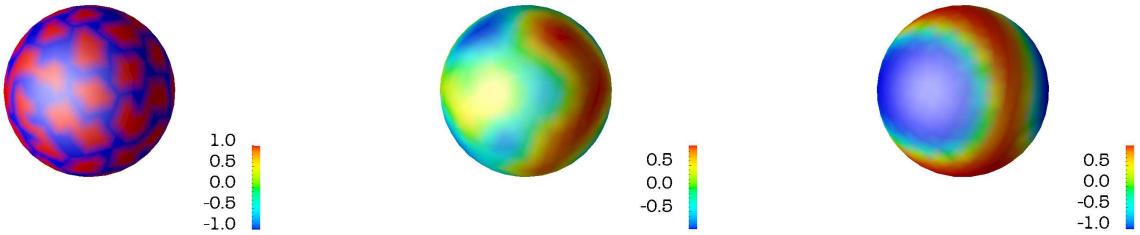

Figure 9.11: Allen-Cahn equation with penalty parameter $\mu = 10$, interface width $\sigma = 0.01$, and timestep $\Delta t = 0.001$.

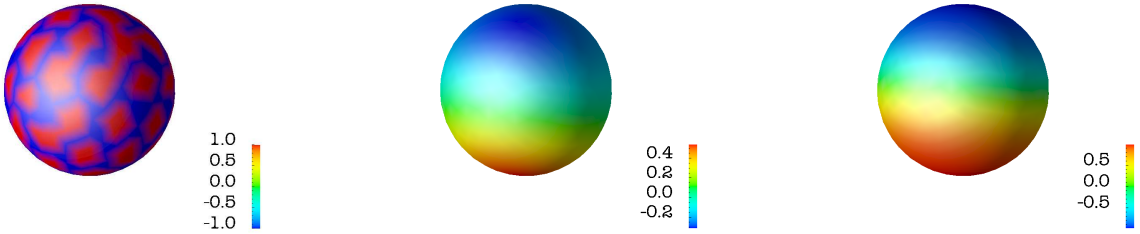

Figure 9.12: Allen-Cahn equation with penalty parameter $\mu = 10$, interface width $\sigma = 0.1$, and timestep $\Delta t = 0.001$.

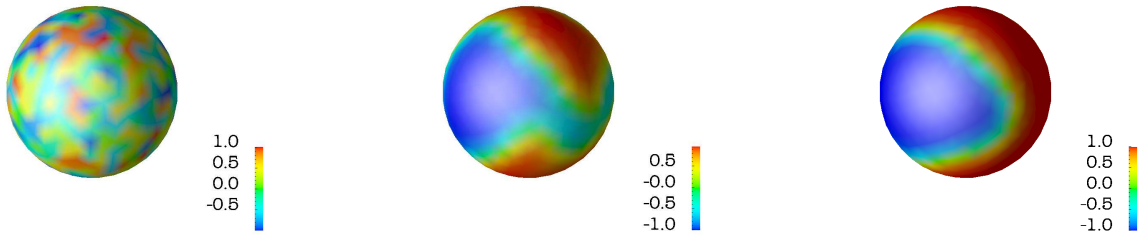

Figure 9.13: Allen-Cahn equation with penalty parameter $\mu = 10$, interface width $\sigma = 0.01$, and timestep $\Delta t = 0.001$.

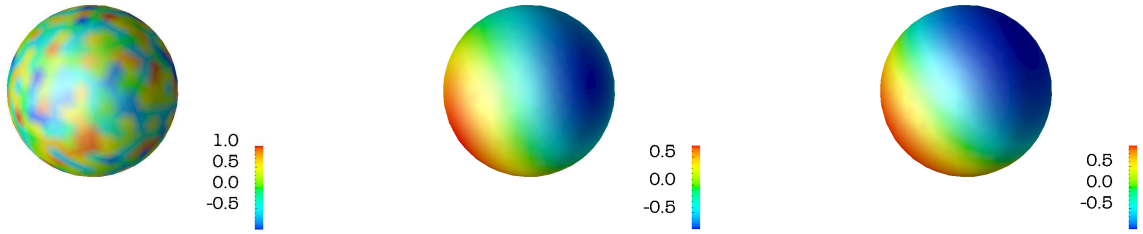

Figure 9.14: Allen-Cahn equation with penalty parameter $\mu = 10$, interface width $\sigma = 0.1$, and timestep $\Delta t = 0.001$.

As can be seen the inital condition does not make a significant impact on the solution in these simulations. Also, note the Allen-Cahn equation solutions look very similar to the Cahn-Hilliard solutions as to be expected. The different values of σ also behave as we would predict. We can compare the total energy of the Allen-Cahn equation using these different σ values. After 10,000 iterations the energy plots for these different σ values are found in Figure 9.15

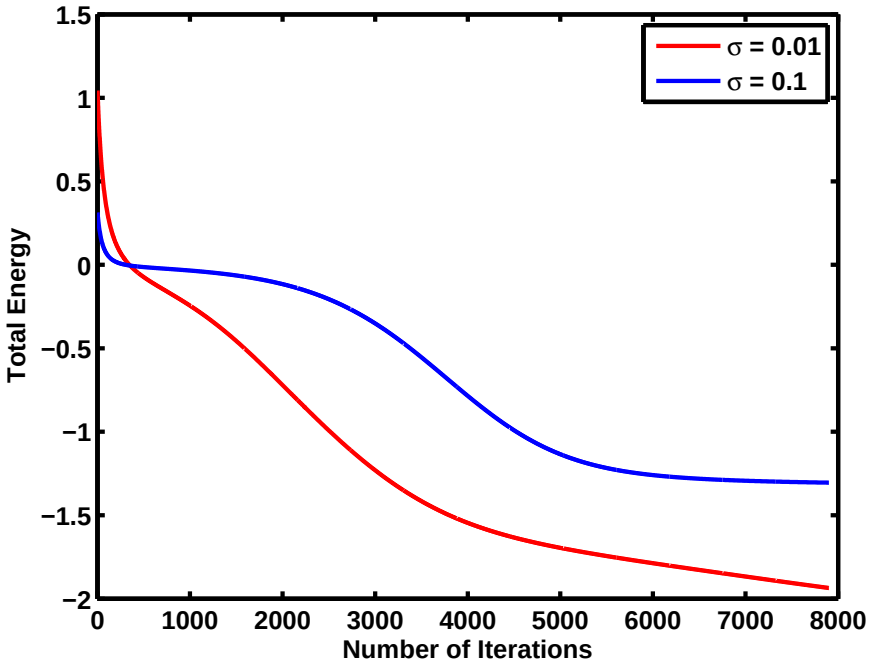

Figure 9.15: Ginzburg-Landau Energy for interface widths $\sigma = 0.01$ and $\sigma = 0.1$

9.4. Curvature Simulations

In this section we numerically implement the curvature lipid raft model presented in Chapter 6. The coding of the model was done in C, using a 6-point Gaussian Quadrature a biconjugate gradient method. We apply the C^0 interior penalty surface finite element method and the time iteration scheme discussed in Chapter 8. We present 4 different simulations using different values for the parameters. We also compare and contrast the total energy and are able to approximate the radius of lipid rafts.

9.4.1. Simulation # 1. In this simulation we set $\epsilon = 0.1$, $C_0 = \frac{1}{0.3}$, $k = 0.01$, $\Delta t = 0.001$. We set the inital condition as a scaled random initial condtion. This scaling allows for more control over how many rafts could be produced given the initial condition. The results are compared side by side with the Allen-Cahn equation in Figure 9.4.1. This simulation was ran on the unit sphere using 3963 nodes. Using a k-means clustering method and calculating the area of each raft we are able to get an approximation of the raft radius. The

radius assiociated with the average raft is approximately 0.23. Which means the curvature is approximately $\frac{1}{0.23}$. We are able to obtain an approximation to the initial spontaneous curvature. The total energy for Simulation #1 and the Allen-Cahn equation have been plotted in Figure 9.16.

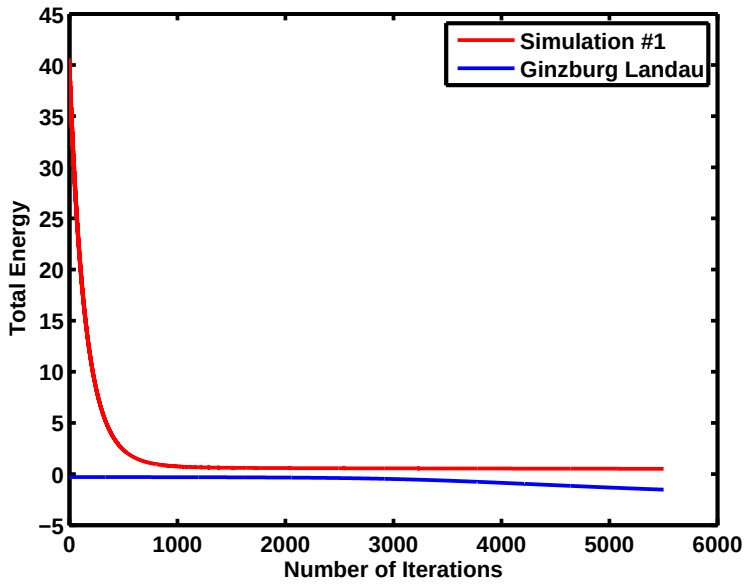

Figure 9.16: Total energy in Simulation #1 vs. Ginzburg-Landau Energy

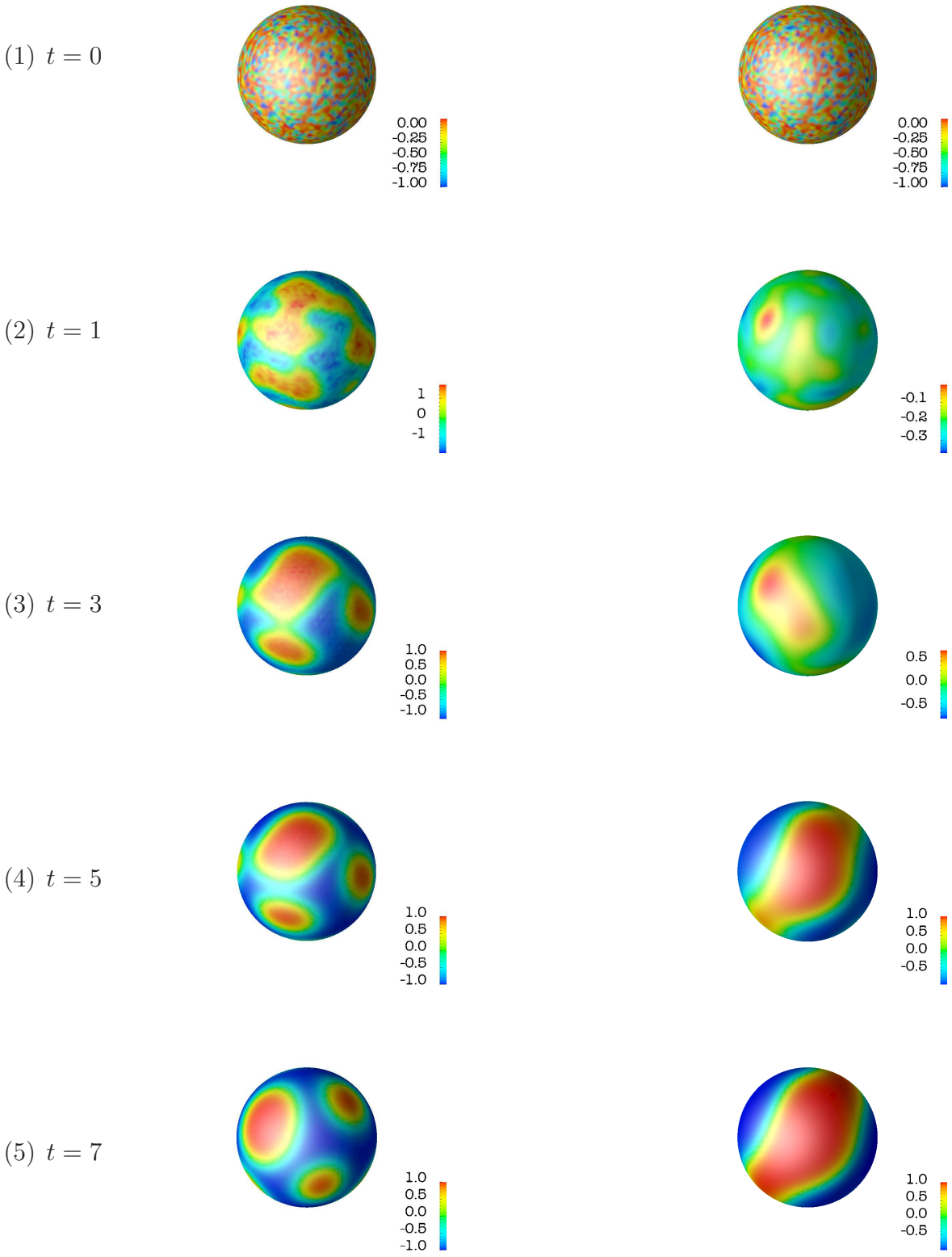

Figure 9.17: Simulation #1 (left) and Allen-Cahn equation (right) at different time steps.

9.4.2. Simulation # 2. In this simulation we set $\epsilon = 0.1$, $C_0 = \frac{1}{0.40}$, $k = 0.01$, $\Delta t = 0.001$. This spontaneous curvature is the reported spontaneous curvature for Lysophosphatidylcholine [30]. We set the inital condition as a random initial condtion. The results are compared side by side with the Allen-Cahn equation in Figure 9.4.2. This simulation was ran on the unit sphere using 984 nodes. Using a k-means clustering method and calculating the area of each raft we are able to get an approximation of the raft radius. The radius assiociated with the largest raft is approximately 0.37. Which means the curvature is approximately $\frac{1}{0.37}$. We are able to obtain an approximation to the initial spontaneous curvature. The total energy for Simulation #2 and the Allen-Cahn equation have been plotted in Figure 9.18.

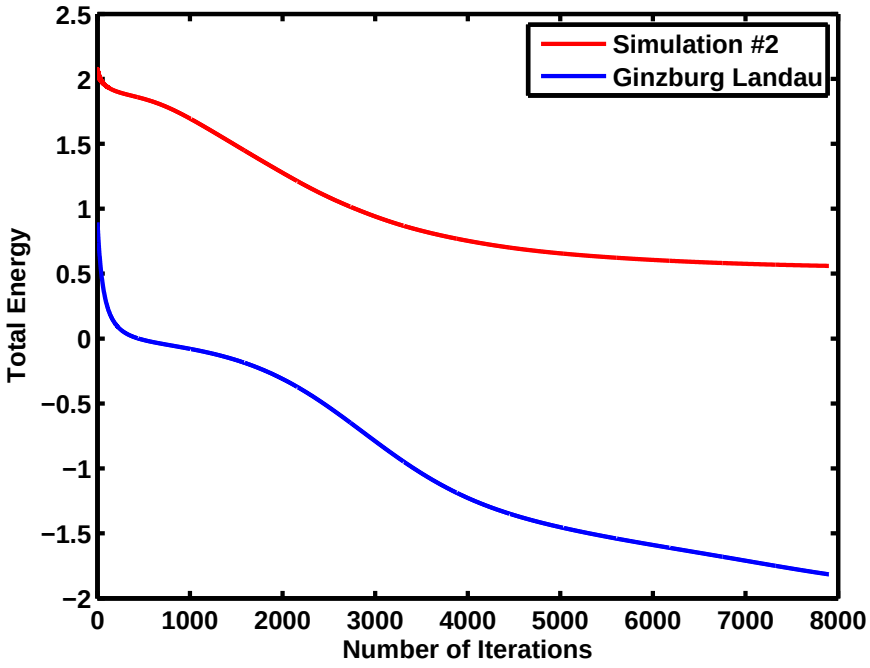

Figure 9.18: Total Energy in Simulation #2 vs. Ginzburg-Landau Energ.y

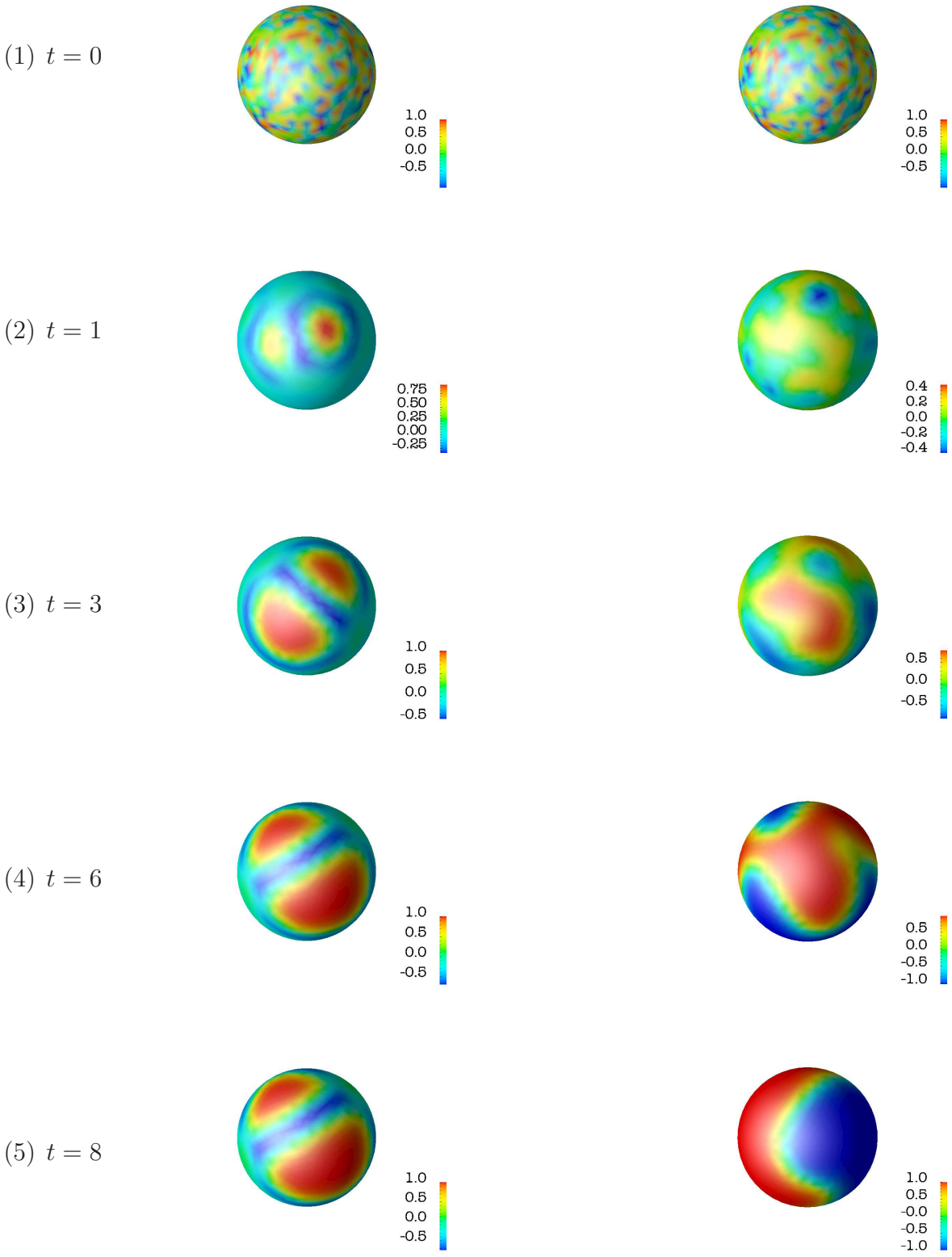

Figure 9.19: Simulation #2 (left) and Allen-Cahn equation (right) at different time steps.

9.4.3. Simulation # 3. In this simulation we use a more robust geometry made of three spheres. We set $\epsilon = 0.1$, $C_0 = \frac{1}{0.4}$, $k = 0.01$, and $\Delta t = 0.001$. The inital condition is random. The results are compared side by side with the Allen-Cahn equation in Figure 9.4.3. Using a k-means clustering method and calculating the area of each raft we are able to get an approximation of the raft radius. The radii of the approximately six rafts produced by this simulation are plotted in Figure 9.20. One can see the largest raft radius obtained by the simulation is about 0.37 which means the curvature of that raft is about $\frac{1}{0.37}$. We are able to approximate the initial spontaneous curvature. The total energy for Simulation #3 and the Allen-Cahn equation have been plotted in Figure 9.21.

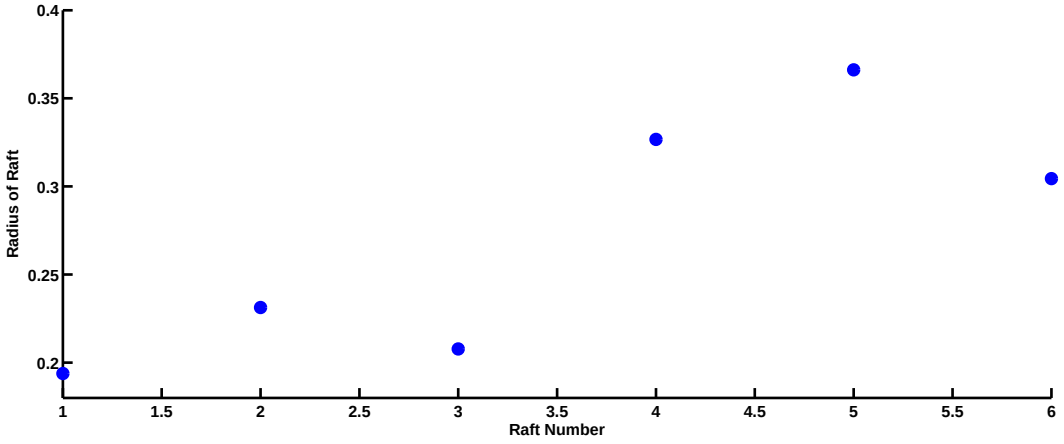

Figure 9.20: The radii of the prominent 6 rafts produced by Simulation #3

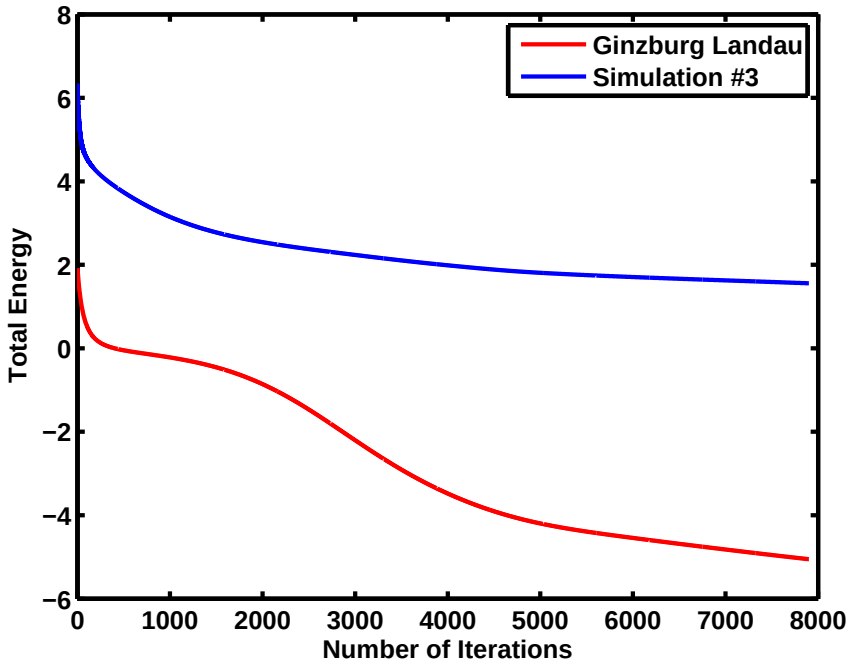

Figure 9.21: Total Energy in Simulation #3 vs. Ginzburg-Landau Energy

(1) $t = 0$

(2) $t = 1$

(3) $t = 3$

(4) $t = 6$

(5) $t = 8$

Figure 9.22: Simulation #3 (left) and Allen-Cahn equation (right) at different time steps.

9.4.4. Simulation # 4. We test the robustness of the numerical implementation by running a simulation using a geometry composed of six spheres. This mesh contains 3903 nodes and we set $\epsilon = 0.1$, $C_0 = \frac{1}{0.4}$, $k = 0.01$, and $\Delta t = 0.001$. The inital condition is random. The results are compared side by side with the Allen-Cahn equation in Figure 9.4.4. Using a k-means clustering method and calculating the area of each raft we are able to get an approximation of the raft radius. The radii of the approximately nine rafts produced by this simulation are plotted in Figure 9.23. One can see the largest raft radius obtained by the simulation is about 0.35 which means the curvature of that raft is about $\frac{1}{0.35}$. We are able to approximate the initial spontaneous curvature. The total energy for Simulation #4 and the Allen-Cahn equation have been plotted in Figure 9.24.

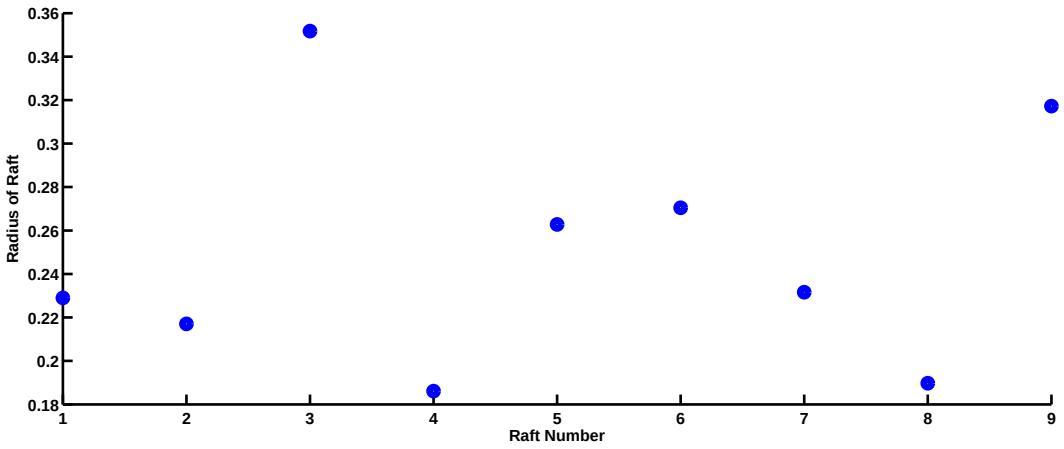

Figure 9.23: The radii of the prominent 9 rafts produced by Simulation #4

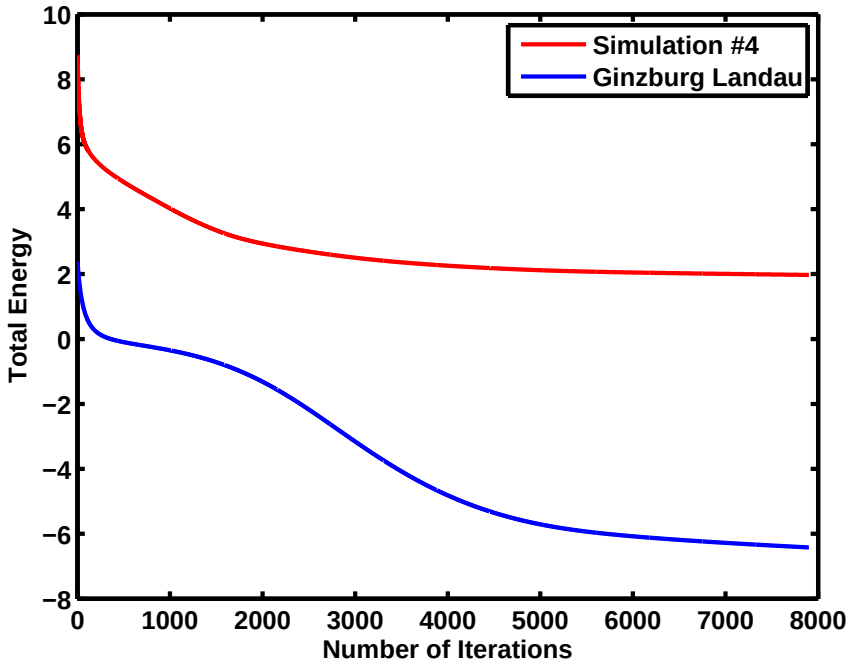

Figure 9.24: Total Energy in Simulation #4 vs. Ginzburg-Landau Energy

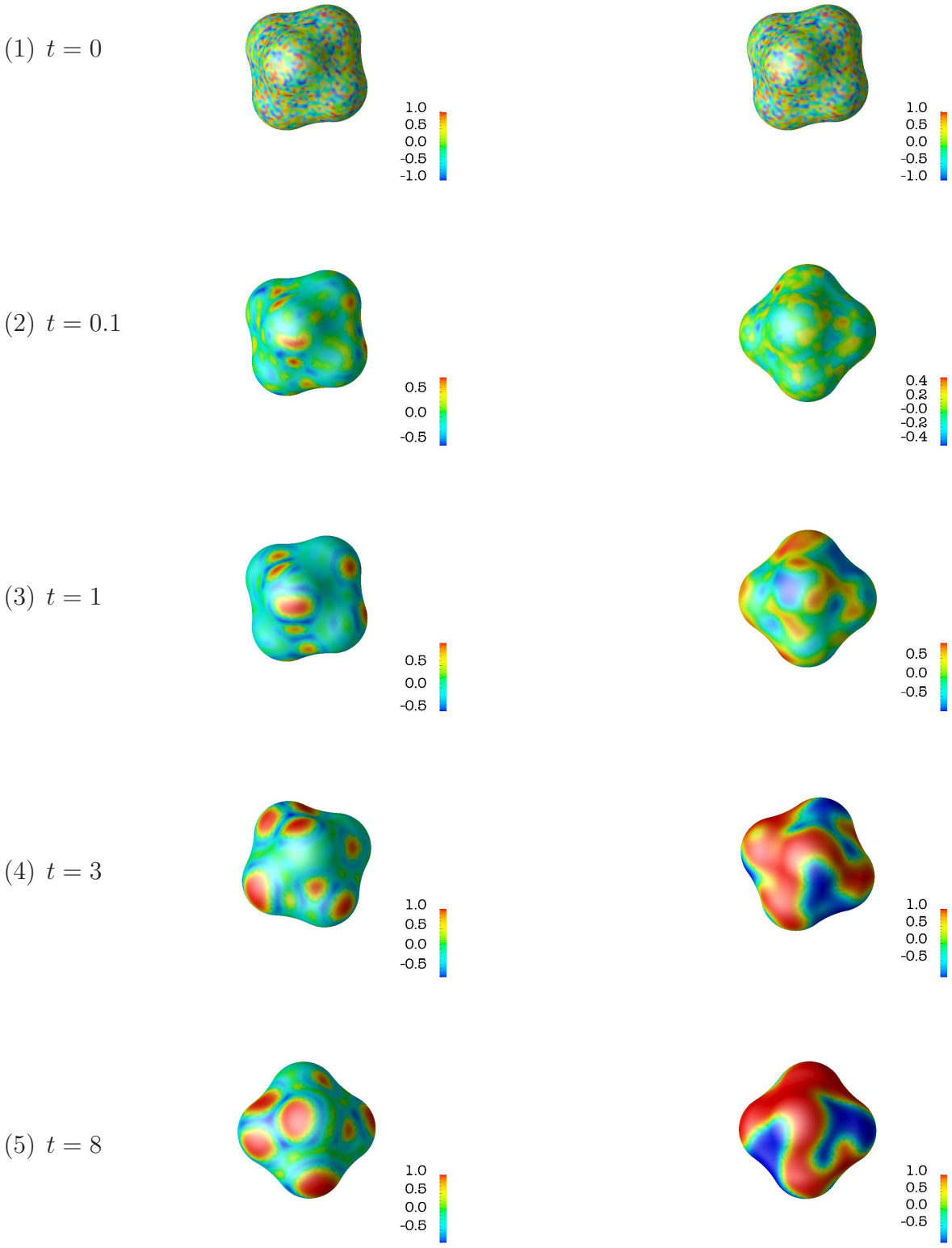

Figure 9.25: Simulation #4 (left) and Allen-Cahn equation (right) at different time steps.

CHAPTER 10

Conclusions

10.1. Conclusions and Discussion

In this work we investigated phase separation on membrane surfaces. We proposed two models starting with the Ginzburg-Landau free energy and adding electrostatic energy and geodesic curvature energy. Patterned states are produced by a competition of the different energies. In Chapter 8 we developed a C^0 interior penalty surface finite element method along with a time iteration scheme to numerically implement these models. The overall aim of this work was to develop the understanding of how lipid rafts could form and obtain the ability to measure the size of the rafts.

The electrostatic model did produce interesting patterns obtained by scaling the electrostatic energy. We produced the lamellar pattern which is produced and discussed quite frequently in the liturature. However it was not able to produce the circular raft-like patterns we are interested in. This model is very sensitive to the value of the parameters and would be worth investingating further.

The geodesic curvature model was able to produce the circular raft-like microdomains we are interested in. We presented four simulations in all of which we were able to produce an approximation to the spontaneous curvature. Using biological data, like the spontatneous curvature of lysophosphatidylcholine, we were able to fit the raft domain sizes by adjusting the spontaneous curvature. The numerical method was shown to be quite robust by running the simulation on different geometries. Ultimately we were able to produce a raft-like pattern and measure the raft size.

10.2. Future Direction

There are numerous future works that can be developed off of the presented models. I believe the investigation into the electrostatic model would prove to be fruitful and helpful

to the field of study. Further work in the analysis of the two models would be benificial, especially analysis that focused on the differences in the surface problem and domain problem. Obtaining bounds on the parameters and their relationship to mesh size and geometry would be extremely valuable. Computationally incorporating different combinations of bending rigidities, spontaneous curvatures, and initial conditions would further convince biologist of the relevance of the model.

Lipid rafts are found on both layers of the bilayer, so one future direction would be to incorporate the second leaflet of the bilayer. The investigation of whether the leaflet interactions could drive different pattern formation would be interesting.

There is much evidence that lipid rafts aid in vesicle budding and the deformation of the membrane. Currently many models are being produced to model vesicle budding and membrane deformation. This opens up a whole research area of connecting the two biological phenomenon. Numerous other biological energies could be incorporated into the models. For instance, adding the thermal fluctuations as discussed in the literature review.

This research is still in its early years but has a bright future for its continued study.

BIBLIOGRAPHY

1. *The state of lipid rafts: From model membranes to cells*, Annual Review of Biophysics and Biomolecular Structure **32** (2003), 257–283.

2. *Model systems, lipid rafts, and cell membranes*, Annual Review of Biophysics and Biomolecular Structure **33** (2004), 269–295.

3. Jonathan J. Amazon and Gerald W. Feigenson, *Lattice simulations of pase morphology on lipid bilayers: Renormalization, membrane shape, and electrostatic dipole interations*, Phys Rev E Stat Nonlin Soft Matter Phys **89** (2014), 1–11.

4. Jonathan J. Amazon, Shih Lin Goh, and Gerald W. Feigenson, *Competition between line tension and curvature stabilizes modulated phase patterns on the surface of giant unilamellas vesicles: A simulation study*, Phys Rev E Stat Nonlin Soft Matter Phys **87** (2013), 1–10.

5. Luis Bagatolli and P. B. Sunil Kumar, *Phase behavior of multicomponent membranes: Experimental and computational techniques*, Soft Matter **5** (2009), 3234–3248.

6. Susanne C Brenner, Shiyuan Gu, Thirupathi Gudi, and Li Yeng Sung, *A quadratic c0 interior penalty method for linear fourth order boundary value problems with boundary conditions of the cahn hilliard type*, SIAM Journal on Numerical Analysis **50** (2012), 2088–2110.

7. Robert Brewster and Samuel A. Safran, *Line active hybrid lipids determine domain size in phase seperation of saturated and unsaturated lipids*, Biophysical Journal **98** (2010), L21–L23.

8. Robert Brewster, Samuel A. Safran, and P.A. Pincus, *Hybrid lipids as a biological surface-active component*, Biophysical Journal **97** (2009), 1087–1094.

9. Luo C, Wang K, Liu de Q, Li Y, and Zhao QS., *The functional roles of lipid rafts in t cell activation, immune diseases and hiv infection and prevention.*, Cell Mol. Immunol. **5** (2008), 1–7.

10. Brian Camley and Frank Brown, *Dynamic scaling in phase separation kinetics for quasi-two-dimensional membranes*, J. Chem. Physics **135** (2011), 1–10.

11. C.B.Muratov, *Theory of domain patterns in systems with long-range interactions of coulomb type*, Phys Rev E Stat Nonlin Soft Matter Phys **66** (2002), 1–25.

12. L.-Q. Chen and J.Shen, *Applications of semi-implicit courier-spectral method to phase field equations*, Comp. Phys. Commun, **108** (1996), 147–158.

13. F.Xabier Contrerasa, Lissete Sanchez-Magranerb, Alicia Alonsoc, and Felix M. Gonic, *Transbilayer (flip-flop) lipid motion and lipid scrambling in membranes*, FEBS Letters **584** (2010), 1779–1786.

14. L. Cueto-Felgueroso and J. Peiraire, *A time-adaptive finite volume method for the Cahn-Hilliard and Kuramoto-Sivashinsky equations*, J. Comp. Phys **227** (2008), 9985–10017.

15. Benjamin Cummings, *Cell biology*, Pearson Education, 2006.

16. Manika Das and Dipak K Das, *Lipid raft in cardiac health and disease*, Current Cardiology Review **5** (2009), 105–111.

17. Klaus Deckelnick, Charles M. Elliott, and Thomas Ranner, *Unfitted finite element methods using bulk meshes for surface partial differential equations*, SIAM J. Numer. Anal **52** (2013), 2137–2162.

18. Klaus Deckelnick, Charles M. Elliott, Thomas Ranner, and C.-J. Heine, *An h-narrow band finite element method for implicit surfaces*, IMA J. Numer. Anal. **30** (2010), 351–376.

19. Q. Du, C. Liu, R. Ryham, and X. Wang, *Modeling the spontaneous curvature effects in static cell membrane deformations by a phase field formulation*, Comm. of Pure and Applied Math. **4** (2005), 537–548.

20. Qiang Du, Lili Ju, and Li Tian, *A finite element approximation of the Cahn-Hilliard equation on surfaces*, Computer Methods in Applied Mechanics and Engineering **200** (2011), 2458–2470.

21. Qiang Du and R.A. Nicolaides, *Numerical analysis of a continuum model of phase transition*, SIAM J. Numer. Anal **28** (1991), 1301–1322.

22. Gerhard Dziuk, *Finite elements for the Beltrami operator on arbitrary surfaces*, Lecture Notes in Mathematics **1357** (1988), 142–155.

23. C. Elliott and D.A. French, *A nonconforming finite element method for the two-dimensional Cahn-Hilliard equation*, SIAM J. Numer. Anal. **26** (1989), 884–903.

24. D.J. Eyre, *Unconditionally gradient stable time marching the Cahn-Hilliard equation*, Mater. Res. Soc. Sympos. Pos (1998).

25. Fabelo, Martin, Santpere, Marin, Torren, Ferrer, and Diaz, *Severe alterations in lipid composition of frontal cortex lipid rafts from Parkinsons disease and incidental Parkinsons disease*, Molecular Medicine **17** (2011), 1107–1118.

26. Fabelo, Martin, Santpere, Puig, Marin, Ferrer, and Diaz, *Lipid alterations in lipid rafts from Alzheimers disease human brain cortex*, Journal of Alzheimer's Disease **19** (2010), 489–502.

27. X. Feng and A.Prohl, *Error analysis of a mixed finite element method for the Cahn-Hilliard equation*, Numer. Math **99** (2004), 47–84.

28. X. Feng and A. Prohl, *An analysis of a fully discrete finite element method for the phase field model and approximation of its sharp interface limits*, SIAM J. Numer. Anal **73** (2003), 541–567.

29. Bengt Fornberg, *A pseudospectral approach for polar and spherical geometries*, SIAM J. Sci. Comput. **16** (1995), 1071–1081.

30. Nola Fuller, Carlos R. Benatti, and R.Peter Rand, *Curvature and bending constants for phosphatidylserine-containing membranes*, Biophysical Journal **85** (2003), 1667–1674.

31. Ana J. Garcia-Saez, Salvatore Chiantia, and Petra Schwille, *Effect of line tension on the lateral organization of lipid membranes*, Journal of Biological Chemistry **282** (2007), 33537–33544.

32. Shih Lin Goh, JonathanJ. Amazon, and Gerald W. Feigenson, *Toward a better raft model: Modulated phases in the four-component bilayer, DSPC/DOPC/POPC/CHOL*, Biophysical Journal **104** (2013), 853–862.

33. A. T. Hammond, F. A. Heberle, T. Baumgart, D. Holowka, B. Baird, and G. W. Feigenson, *Crosslinking a lipid raft component triggers liquid ordered-liquid disordered phase separation in model plasma membranes*, Proceedings of the National Academy of Sciences **102** (2005), 6320–6325.

34. Y. He, Y. Liu, and T. Tang, *On large time stepping methods of the Cahn-Hilliard equation*, Appl. Numer. Math **57** (2007), 616–628.

35. J.Barrett and J.Blowey, *An error bound for the finite element approximation of the Cahn-Hilliard equation with logarithm free energy*, Numer. Math **72** (1995), 1–20.

36. J.Barrett, J.Blowey, and H.Garcke, *On fully practical finite element approximations of degenerate Cahn-Hilliard systems*, Math. Mod. and Numer. Analy. **35** (2000), 713–748.

37. J.-H. Jeong, N. Goldenfield, and J. Dantzig, *Phase field model for three-dimensional dendritic growth with fluid flow*, Phys Rev E Stat Nonlin Soft Matter Phys **64** (2001), 1–14.

38. A. Kassam and L. Trefethen, *Fourth-order time-stepping for stiff odes*, SIAM J. Sci. Comput. **26** (2005), 1214–1233.

39. Vladimir Yu Kiselev, Davide Marenduzzo, and Andrew B Goryachev, *Lateral dynamics of proteins with polybasic domain on anionic membranes: a dynamic Monte-Carlo study*, Biophysical Journal **100** (2011), 1261.

40. Shigeyuki Komura and David Andelman, *Physical aspects of heterogeneities in multi-component lipid membranes*, Advances in Colloid and Interface Science **208** (2014), 34–46.

41. M. Maeda, *Membranes and transport*, Elsevier, China, 2005.

42. J. Mart and F.S.Csajka, *Flip-flop dynamics in a model lipid bilayer membrane*, Europhysics Letters **61** (2003), 409–414.

43. Fredrick R. Maxfield and Ira Tabas, *Role of cholesterol and lipis organization in disease*, Nature **438** (2005), 612–621.

44. Sebastian Meinhart, Richard L.C. Vink, and Friederike Schmid, *Monolayer curvature stabilizes nanoscale rat domains in mixed lipid bilayers*, Proceedings of the National Academy of Sciences **110** (2013), 3234–3248.

45. Kamran Mohseni and Tim Colonius, *Numerical treatment of polar coordinate singularities*, J. Comp. Phys. **157** (2000), 787–795.

46. Toshiyuki Murai, *The role of lipid rafts in cancer cell adhesion and migration*, International Journal of Cell Biology **2012** (2012), 1–6.

47. Ramon Relgada, Jordi Gomez, Javier Buceta, Katja Lindenberg, and Francesc Sagues, *Pattern formation in nonequillibrium lipid membranes: From membrane undulations to lipid rafts*, Biophysical Reviews and Letters **15** (2010), 1–34.

48. Ken Ritchie and Jeff Spector, *Single molecule studies of molecular diffusion in cellular membranes: Determining membrane structure*, Biopolymers **87** (2007), 95–101.

49. Tamar Schlick, *Molecular modeling and simulation: An interdisciplinary guide*, Springer, New York, NY, 2010.

50. P. Schwartz, D. Adalsteinsson, P. Colella, A. P. Arkin, and M.Onsum, *Numerical computation of diffusion on a surface*, Proceedings of the National Academy of Sciences **102** (2005), 11151–11156.

51. Michael Seul and David Andelman, *Domain shapes and patterns: The phenomenology of modulated phases*, Science **267** (1995), 476–483.

52. Kai Simons and Elina Ikonen, *Functional rafts in cell membranes*, Nature **387** (1997), 569–572.

53. Campbell SM, Crowe SM, and Mak J., *Lipid rafts and HIV-1: from viral entry to assembly of progeny virions*, J. Clin Virol. **3** (2001), 217–27.

54. Michael Spivak, *Calculus on manifolds*, Addison-Wesley, United States of America, 1965.

55. Dina Vind-Kezunovic, Claus Helix Nielsen, Urszula Wojewodska, and Robert Gniadecki, *Line tension at lipid phase boundaries regulates formation of membrane vesicles in living cells*, BBA - Biomembranes **1778** (2008), 2480–2486.

56. G. Wells, E. Kuhl, and K. Garikipati, *A discontinuous Galerkin method for the Cahn-Hilliard equation*, J. Comp. Phys. **218** (2006), 860–877.

57. C.-W.Shu Y. Xia, Y.Xu, *Local discontinuous Galerkin methods for the Canh-Hilliard type equations*, J. Comp. Phys. **227** (2007), 472–491.

58. Y.C. Zhou, *Electrodiffusion of lipids on membrane surfaces*, J. Chem. Phys. **136** (2012), 205103.